

**STUDIES ON SYNTHESIS CHARACTERISATION  
OF  $\text{AgI}_{1-x}\text{Cl}_x$  SOLID SOLUTIONS FOR  $\text{I}_2$  AND  $\text{Cl}_2$   
SENSING PROPERTIES**

*By*

**P.C. CLINSHA**

**CHEM02201104013**

**Indira Gandhi Centre for Atomic Research, Kalpakkam**

*A thesis submitted to the  
Board of Studies in Chemical Sciences  
In partial fulfilment of requirements  
for the Degree of  
**DOCTOR OF PHILOSOPHY**  
of  
**HOMI BHABHA NATIONAL INSTITUTE***



**August 2017**

# Homi Bhabha National Institute<sup>1</sup>

## Recommendations of the Viva Voce Committee

As members of the Viva Voce Committee, we certify that we have read the dissertation prepared by **P.C. Clinsha** entitled “**Studies on Synthesis Characterisation of AgI<sub>1-x</sub>Cl<sub>x</sub> Solid Solutions for I<sub>2</sub> and Cl<sub>2</sub> Sensing Properties**” and recommend that it may be accepted as fulfilling the thesis requirement for the award of Degree of Doctor of Philosophy.

---

Chairman – M. Joseph

**Date:**

---

Guide / Convener – V. Jayaraman

**Date:**

---

Examiner-Prof. S.M. Shivaprasad

**Date:**

---

Member 1- K. Ananthasivan

**Date:**

---

Member 2- N.V. Chandra Shekar

**Date:**

---

Technical Advisor – K. Prabakar

**Date:**

---

Final approval and acceptance of this thesis is contingent upon the candidate's submission of the final copies of the thesis to HBNI.

I/We hereby certify that I/we have read this thesis prepared under my/our direction and recommend that it may be accepted as fulfilling the thesis requirement.

**Date:**

**Place:**

**Guide**

---

<sup>1</sup> This page is to be included only for final submission after successful completion of viva voce.

## **STATEMENT BY AUTHOR**

This dissertation has been submitted in partial fulfilment of requirements for an advanced degree at Homi Bhabha National Institute (HBNI) and is deposited in the Library to be made available to borrowers under rules of the HBNI.

Brief quotations from this dissertation are allowable without special permission, provided that accurate acknowledgement of source is made. Requests for permission for extended quotation from or reproduction of this manuscript in whole or in part may be granted by the Competent Authority of HBNI when in his or her judgment the proposed use of the material is in the interests of scholarship. In all other instances, however, permission must be obtained from the author.

**P C Clinsha**

## **DECLARATION**

I, hereby declare that the investigation presented in the thesis has been carried out by me.  
The work is original and has not been submitted earlier as a whole or in part for a degree /  
diploma at this or any other Institution / University.

**P C Clinsha**

## List of Publications arising from the thesis

### Journal

1. Iodine sensing by AgI and  $\text{AgI}_{1-x}\text{Cl}_x$ , **P.C. Clinsha**, K.I. Gnanasekar, V. Jayaraman and T. Gnanasekaran, *Electroanalysis*, 2014, 26, 2398-2402
2.  $\text{AgI}_{1-x}\text{Cl}_x$  ( $x = 0.025$ ) electrolytes for trace level sensing of chlorine, **P.C. Clinsha**, K.I. Gnanasekar, V. Jayaraman and T. Gnanasekaran, *IEEE: Physics and Technology of Sensors (ISPTS)*, 2015, doi: 10.1109/ISPTS.2015.7220090
3. Halogen sensing using  $\text{AgI}_{1-x}\text{Cl}_x$  ( $x= 0-0.25$ ), **P.C. Clinsha**, K.I. Gnanasekar and V. Jayaraman, *Communicated to Journal of Alloys and Compounds*, 2018
4. Studies on the solubility of AgCl in AgI, **P.C. Clinsha**, S. Vijayalakshmi, Uma Maheswari and V. Jayaraman, under preparation

### Conferences

1. Iodine sensing by AgI and  $\text{AgI}_{1-x}\text{Cl}_x$ , **P.C. Clinsha**, T. Tamil Selvam, K.I. Gnanasekar, V. Jayaraman and T. Gnanasekaran, *ISEAC DM2014*, Amritsar
2. Chlorine sensing using  $\text{AgI}_{1-x}\text{Cl}_x$  ( $x = 0-0.025$ ), **P.C. Clinsha**, K.I. Gnanasekar, V. Jayaraman and T. Gnanasekaran, *CHEMNUT 2015*, Kalpakkam
3. Chlorine sensing using  $\text{AgI}_{1-x}\text{Cl}_x$  ( $x = 0-0.025$ ), **P.C. Clinsha**, K.I. Gnanasekar, V. Jayaraman and T. Gnanasekaran, *ISPTS 2015*, Pune
4.  $\text{AgI}_{1-x}\text{Cl}_x$  systems- $\text{I}_2$  and  $\text{Cl}_2$  sensing materials, **P.C. Clinsha**, K.I. Gnanasekar, V. Jayaraman and T. Gnanasekaran, *SETSC*, 2016, Tirupathi

P C Clinsha

## **DEDICATIONS**

*To my husband, daughter & our parents*

## **ACKNOWLEDGEMENTS**

I wish to express my sincere gratitude to Dr. V. Jayaraman, Head, Materials Chemistry Division, Indira Gandhi Centre for Atomic Research (IGCAR), Kalpakkam. He inspired me greatly to work in this project. His willingness to motivate me contributed tremendously to the project. I am thankful to his priceless discussions towards completion of this work.

I would also like to thank Dr. K. I Gnanasekar, Head, Novel Chemical Sensor Section and Dr. E. Prabhu, Novel Chemical Sensor Section and other colleagues who provided me constant support.

I wish to extend my heartfelt thanks to Dr. Carsten Schwandt, National Chair Professor, University of Nizwa, Sultanate of Oman, for helping me to refine my thesis to a greater extent.

I wish to acknowledge all the colleagues whose skilled expertise rendered the useful characterisation and fabrications for successfully completing this thesis.

**P C Clinsha**

| <b>CONTENTS</b>        |   | <b>Page<br/>No</b> |
|------------------------|---|--------------------|
| <b>SYNOPSIS</b>        |   | xiii               |
| <b>LIST OF FIGURES</b> |   | xv                 |
| <b>LIST OF TABLES</b>  |   | xx                 |
| <b>CHAPTER 1</b>       | <b>INTRODUCTION</b>   | 1                  |
|                        | 1.1 Sources of iodine and chlorine  | 1                  |
|                        | 1.1.1 Natural Sources of iodine and chlorine  | 1                  |
|                        | 1.1.2 Processes involving the production of iodine and chlorine in industrial scale | 1                  |
|                        | 1.2 Iodine and chlorine in nuclear industry   | 4                  |
|                        | 1.2.1 Thermal reactor   | 4                  |
|                        | 1.2.2 Fast reactor  | 5                  |
|                        | 1.3 Iodine in nuclear industry  | 6                  |
|                        | 1.3.1 Role of chlorine in pyroprocessing of spent nuclear fuels                     | 7                  |
|                        | 1.4 Applications of iodine and chlorine   | 9                  |
|                        | 1.5 Effect of exposure of radioactive iodine  | 10                 |
|                        | 1.6 Effect of exposure to chlorine  | 10                 |
|                        | 1.7 Different methodologies to sense halogen and halide ions                        | 11                 |
|                        | 1.7.1 Conductometric mode of sensing iodine vapour                                  | 11                 |
|                        | 1.7.2 Optical sensing of iodide in solution   | 11                 |
|                        | 1.7.3 Potentiometric mode for sensing iodine vapours                                | 12                 |

| <b>CONTENTS</b>  |  | <b>Page<br/>No</b> |
|------------------|--|--------------------|
| 1.7.4            | Conductometric sensors for chlorine using organometallic compound                              | 13                 |
| 1.7.5            | Potentiometric sensing of chlorine   | 14                 |
| 1.7.6            | Optical sensing of chlorine  | 14                 |
| 1.8              | Salient features and limitations of conductometric, optical and potentiometric mode of sensing | 15                 |
| 1.9              | Determination of radioactive iodine  | 15                 |
| 1.10             | The concept of Gibbs energy  | 16                 |
| 1.10.1           | Relation between Gibbs energy and emf in an electrochemical cell                               | 18                 |
| 1.11             | Electrochemical sensors based on solid electrolyte   | 20                 |
| 1.12             | Other application of potentiometric cells using solid electrolyte                              | 24                 |
| 1.13             | Structure of AgI   | 26                 |
| 1.14             | Substitution of cationic or anionic species in AgI   | 28                 |
| 1.15             | Scope of the thesis  | 30                 |
| 1.16             | References   | 31                 |
| <b>CHAPTER 2</b> | <b>EXPERIMENTAL METHODS, PRICIPLES AND APPLICATION</b>   | <b>41</b>          |
| 2.1              | Introduction   | 41                 |
| 2.2              | Experimental   | 41                 |
| 2.3              | Preparation of $\text{AgI}_{1-x}\text{Cl}_x$   | 41                 |
| 2.4              | X-ray diffraction  | 42                 |

| <b>CONTENTS</b>  |   | <b>Page<br/>No</b> |
|------------------|---|--------------------|
| 2.5              | Scanning electron microscopy  | 44                 |
| 2.6              | Differential Scanning Calorimetry   | 44                 |
| 2.7              | Atomic absorption spectroscopy  | 45                 |
| 2.8              | X-ray photoelectron spectroscopy  | 46                 |
| 2.9              | Ionic transport measurements  | 48                 |
| 2.10             | Dielectric impedance spectroscopy   | 49                 |
|                  | 2.10.1 Exchange current density<br>measurements using three electrode<br>configuration    | 52                 |
| 2.11             | Sensor set-up   | 57                 |
|                  | 2.11.1 Miniaturised chlorine sensor   | 59                 |
| 2.12             | Conclusion  | 60                 |
| 2.13             | References  | 61                 |
| <b>CHAPTER 3</b> | <b>PHYSICOCHEMICAL CHARACTERISATION<br/>OF AgI<sub>1-x</sub>Cl<sub>x</sub> (x=0-0.25)</b> | <b>63</b>          |
| 3.1              | Introduction  | 63                 |
| 3.2              | Experimental  | 63                 |
| 3.3              | X-ray diffraction studies   | 63                 |
|                  | 3.3.1 Unit cell volume calculation  | 65                 |
| 3.4              | Morphological characterisation  | 67                 |
| 3.5              | DSC measurements  | 70                 |
| 3.6              | Solubility limit estimation using AAS and XPS<br>technique                                | 74                 |
|                  | 3.6.1 Solubility studies using atomic<br>absorption spectrometer (AAS)                    | 74                 |

| <b>CONTENTS</b>  |   | <b>Page<br/>No</b> |
|------------------|---|--------------------|
|                  | 3.6.2 Elucidation of AgCl solubility in AgI by using X-ray photoelectron spectroscopy | 76                 |
|                  | 3.7 Studies related to ionic conduction and bulk electrical conductivity              | 81                 |
|                  | 3.7.1 Transport number measurement studies  | 81                 |
|                  | 3.7.2 Electrical conductivity studies   | 83                 |
|                  | 3.8 Conclusion  | 92                 |
|                  | 3.9 References  | 93                 |
| <b>CHAPTER 4</b> | <b>HALOGEN SENSING CHARACTERISTICS OF AgI<sub>1-x</sub>Cl<sub>x</sub> (x=0-0.05)</b>  | 95                 |
|                  | 4.1 Introduction  | 95                 |
|                  | 4.2 Experimental  | 95                 |
|                  | 4.3 Principle of halogen sensing by AgI <sub>1-x</sub> Cl <sub>x</sub>                | 95                 |
|                  | 4.3.1 Theoretical emf calculation   | 95                 |
|                  | 4.4 Iodine sensing characteristics  | 98                 |
|                  | 4.5 Comparison of experimental value to the theoretical emf                           | 103                |
|                  | 4.6 Chlorine sensing characteristics  | 104                |
|                  | 4.7 Conclusion  | 108                |
|                  | 4.8 References  | 109                |
| <b>CHAPTER 5</b> | <b>METHODOLOGY FOR ELUCIDATING THE MECHANISM OF AgI TOWARDS SENSING OF CHLORINE</b>   | 111                |
|                  | 5.1 Introduction  | 111                |
|                  | 5.2 Experimental  | 111                |
|                  | 5.3 Non retracing behaviour of AgI towards chlorine                                   | 111                |

| <b>CONTENTS</b>  |   | <b>Page<br/>No</b> |
|------------------|---|--------------------|
|                  | 5.3.1 X-ray photoelectron spectroscopic studies                                       | 112                |
|                  | 5.3.2 Study on the working electrode interface<br>of AgI using impedance spectroscopy | 116                |
|                  | 5.4 Conclusion  | 121                |
|                  | 5.5 References  | 121                |
| <b>CHAPTER 6</b> | <b>FABRICATION AND TESTING OF<br/>MINIATURISED CHLORINE SENSOR</b>                    | 123                |
|                  | 6.1 Introduction  | 123                |
|                  | 6.2 Experimental  | 123                |
|                  | 6.3 Principle of operation  | 123                |
|                  | 6.4 Fabrication and assembly of sensor  | 124                |
|                  | 6.4.1 Materials for making sensor   | 124                |
|                  | 6.4.2 Sketch of sensor  | 124                |
|                  | 6.5 Sensing characteristics of miniaturised sensor                                    | 129                |
|                  | 6.6 Conclusion  | 133                |
|                  | 6.7 References  | 133                |
| <b>CHAPTER 7</b> | <b>SUMMARY AND CONCLUSIONS</b>  | 135                |
| <b>CHAPTER 8</b> | <b>FUTURE PLANS</b>   | 137                |

## SYNOPSIS

Iodine is one of the major fission products in nuclear fission reactor with a range of isotopes produced during the fission reaction.  $^{129}\text{I}$  is the radioisotope of concern because of its high half-life. During any accidental leak from the reactor, the isotope  $^{129}\text{I}$ , if ingested in human body, will take longer time to decay. Copious amounts of chlorine gas are used in pyroprocessing of nuclear fuels for purging the electrochemical cell containing the LiCl-KCl bath. Thus, iodine and chlorine need to be monitored, during normal operation of the reactor and pyroprocessing units.

The objective of this thesis is to investigate suitable materials for iodine and chlorine sensing. Solid state sensors based on AgI shows good ionic conduction above 423 K due to its open crystal structure. Such compounds with high ionicity are ideal to be used as electrolyte in a potentiometric sensor. The affinity of Ag in AgI to maintain equilibrium with iodine and chlorine and being one of the best ionic conductors are the driving force for selecting AgI as the base matrix for sensing material. The need for substituting I<sup>-</sup> with Cl<sup>-</sup> was to reduce the  $\beta$  to  $\alpha$  transition temperature. Thus, it would be possible to operate the sensor material containing appropriate AgCl content, at much lower temperature compared to pure AgI. Also, it is expected that the presence of Cl<sup>-</sup> in AgI will increase the selectivity of the electrochemical sensor towards chlorine gas.

The solubility limit of AgCl in AgI prepared through a novel solution route was established by using various physicochemical techniques. The gradation in other physical properties like morphology, ionic transference number and bulk conductivity observed for the composition  $\text{AgI}_{1-x}\text{Cl}_x$  was compared with solubility limit studies.

Characterisation of the compositions AgI, AgI<sub>0.975</sub>Cl<sub>0.025</sub> and AgI<sub>0.95</sub>Cl<sub>0.05</sub> for sensing were carried out towards 6-60 vppm of iodine and 20-100 vppb of chlorine gas at 428 K. The unusual behaviour of AgI towards chlorine gas was studied by an in - house fabricated three electrode configuration using dielectric spectroscopic technique. The results were then compared with the XPS studies to confirm the findings from the impedance and capacitance measurements at the electrode-electrolyte interface. A miniaturised chlorine sensor was fabricated and was tested for 17-15000 vppb of chlorine in air at 428 K. The advantage of miniaturisation and the improvement in detecting lower concentration are further discussed in different chapters.

| <b>Figure No.</b> | <b>LIST OF FIGURES</b>  | <b>Page No.</b> |
|-------------------|---|-----------------|
| 1.1               | Schematic of pressurised heavy water reactor  | 5               |
| 1.2               | Sketch of FBTR at Kalpakkam   | 6               |
| 1.3               | Schematic of pyroprocessing electrochemical cell  | 8               |
| 1.4               | Pie chart representing industrial uses of (a) iodine and (b) chlorine   | 9               |
| 1.5               | Schematic of the potentiometric sensor used for measuring the iodine concentration  | 13              |
| 1.6               | Schematic of (a) high conduction (channel for electron transfer) of antimony-doped SnO <sub>2</sub> in air and (b) reduced conduction in the presence of chlorine gas | 14              |
| 1.7               | Sketch of a potentiometric sensor   | 20              |
| 1.8               | Tetrahedra with (a) corner shared (b) edge shared and (c) face shared atoms   | 27              |
| 1.9               | Crystal structure of (a) $\gamma$ -AgI (b) $\beta$ -AgI and (c) $\alpha$ -AgI   | 29              |
| 1.10              | Crystal structure of $\alpha$ -AgI representing the 42 interstitial voids   | 29              |
| 2.1               | Schematic representation of Bragg's law   | 43              |
| 2.2               | Sketch of XPS facility  | 48              |
| 2.3               | Impedance plot of Parallel combination of resistor and capacitor  | 51              |
| 2.4               | Sketch of the fabrication cell for ionic transport measurements   | 53              |
| 2.5               | Cell arrangements (a), (b) and (c) for studying three electrode configuration   | 49              |
| 2.6               | Sketch of the three electrode configuration   | 56              |
| 2.7               | (a) Sketch of the sensor set up used for studying bulk pellets and (b) Configuration of the potentiometric cell   | 58              |
| 2.8               | Schematic of the dynamic flow experiment for iodine sensing studies   | 59              |

| <b>Figure No.</b> | <b>LIST OF FIGURES</b>   | <b>Page No.</b> |
|-------------------|--|-----------------|
| 2.9               | Photograph of miniaturised chlorine sensor   | 60              |
| 3.1               | XRD pattern of (a) AgI as-prepared (b) $\beta$ -AgI (c) $\gamma$ -AgI  | 64              |
| 3.2               | XRD pattern of $\text{AgI}_{1-x}\text{Cl}_x$ with x as (a) 0, (b) 0.05, (c) 0.1 and (d) 0.25                               | 65              |
| 3.3               | SEM images of (a) AgI and (b) $\text{AgI}_{0.975}\text{Cl}_{0.025}$  | 68              |
| 3.4               | SEM images of (a) $\text{AgI}_{0.95}\text{Cl}_{0.05}$ and (b) $\text{AgI}_{0.94}\text{Cl}_{0.06}$                          | 68              |
| 3.5               | EDX of $\text{AgI}_{0.975}\text{Cl}_{0.025}$ for the image shown in Fig. 3.3 (b) in a specified spot                       | 69              |
| 3.6               | EDX of $\text{AgI}_{0.96}\text{Cl}_{0.04}$ for the image shown in Fig. 3.4 (b) in a specified spot appearing as clusters   | 69              |
| 3.7               | DSC pattern of AgI   | 71              |
| 3.8               | DSC pattern of $\text{AgI}_{0.975}\text{Cl}_{0.025}$   | 71              |
| 3.9               | DSC pattern of $\text{AgI}_{0.95}\text{Cl}_{0.05}$   | 72              |
| 3.10              | DSC pattern of $\text{AgI}_{0.94}\text{Cl}_{0.06}$   | 72              |
| 3.11              | DSC pattern of $\text{AgI}_{0.9}\text{Cl}_{0.1}$   | 73              |
| 3.12              | Phase diagram of AgI-AgCl composition with temperature   | 73              |
| 3.13              | Plot of $\beta$ -AgI to $\alpha$ -AgI phase transition vs. concentration of $\text{Cl}^-$ in AgI from DSC measurements     | 74              |
| 3.14              | XPS patterns of Cl 2p of $\text{AgI}_{0.95}\text{Cl}_{0.05}$ as-prepared sample  | 76              |
| 3.15              | XPS patterns of Cl 2p of $\text{AgI}_{0.95}\text{Cl}_{0.05}$ sample after heating at 473 K and washing with ammonia        | 77              |
| 3.16              | XPS patterns of Ag 3d of $\text{AgI}_{0.95}\text{Cl}_{0.05}$ ammonia washed (a) as-prepared sample and (b) heated to 473 K | 79              |
| 3.17              | XPS patterns of I 3d of $\text{AgI}_{0.95}\text{Cl}_{0.05}$ ammonia washed (a) as-prepared sample and (b) heated to 473 K  | 80              |

| Figure No. | LIST OF FIGURES   | Page No. |
|------------|---|----------|
| 3.18       | Typical plot of current vs. time for AgI at (a) 298 and (b) 423 K with a DC potential of 0.5 V  | 82       |
| 3.19       | Typical Nyquist plots for AgI at temperatures of (a) 298 K (b) 373 K (c) 408 K (d) 413 K (e) 417 K and (f) 473 K  | 84-87    |
| 3.20       | Bauerle equivalent circuit  | 88       |
| 3.21       | Equivalent circuit used for fitting $\text{AgI}_{1-x}\text{Cl}_x$   | 89       |
| 3.22       | Arrhenius plots of $\text{AgI}_{1-x}\text{Cl}_x$ with x as (-▲-) 0, (-●-) 0.025, (-■-) 0.05 and (-○-) 0.06  | 91       |
| 4.1        | Sketch of the electrochemical cell used for sensing halogen   | 95       |
| 4.2        | Transient response of AgI and ~40 vppm of iodine gas at 428 K   | 97       |
| 4.3        | Typical variation in the baseline of AgI based electrochemical cell during the passage of the argon carrier gas   | 98       |
| 4.4        | Typical transient observed by AgI ~6 vppm of iodine at 428 K  | 99       |
| 4.5        | Typical transient observed by $\text{AgI}_{0.975}\text{Cl}_{0.025}$ ~6 vppm of iodine at 428 K  | 100      |
| 4.6        | Typical transient observed by $\text{AgI}_{0.95}\text{Cl}_{0.05}$ ~6 vppm of iodine at 428 K  | 100      |
| 4.7        | Calibration plot of iodine sensing in the range of 6-60 vppm for (a) AgI, (b) $\text{AgI}_{0.975}\text{Cl}_{0.025}$ and (c) $\text{AgI}_{0.95}\text{Cl}_{0.05}$ | 102      |
| 4.8        | Plot of experimental vs theoretical value of $\text{AgI}_{1-x}\text{Cl}_x$ (x=0, 0.025 and 0.05) towards ~6-60 vppm of iodine at 428 K                          | 103      |
| 4.9        | Typical transients observed for $\text{AgI}_{0.975}\text{Cl}_{0.025}$ towards (a) 20 vppb and (b) 100 vppb $\text{Cl}_2$ gas                                    | 105      |
| 4.10       | Typical transient exhibited by $\text{AgI}_{0.95}\text{Cl}_{0.05}$ towards (a) 20 vppb and (b) 100 vppb $\text{Cl}_2$   | 106      |
| 4.11       | Calibration plots of (a) $\text{AgI}_{0.975}\text{Cl}_{0.025}$ and (b) $\text{AgI}_{0.95}\text{Cl}_{0.05}$ towards 20-100 vppb chlorine at 428 K                | 108      |

| <b>Figure No.</b> | <b>LIST OF FIGURES</b>   | <b>Page No.</b> |
|-------------------|--|-----------------|
| 5.1               | Transient response for AgI towards 40 vppb Cl <sub>2</sub>   | 112             |
| 5.2               | XPS pattern of Ag 3d peak after exposure to 500 vppb of Cl <sub>2</sub> gas at 428 K   | 114             |
| 5.3               | XPS pattern of I 3d peak for AgI after exposure to 500 vppb of Cl <sub>2</sub> gas at 428 K                                      | 114             |
| 5.4               | XPS pattern of Cl 2p peak in AgI after exposure to 500 vppb of Cl <sub>2</sub> gas at 428 K                                      | 115             |
| 5.5               | Nyquist plot of AgI at 428 K   | 116             |
| 5.6               | Nyquist plot of AgI exposed to iodine at 428 K   | 117             |
| 5.7               | Nyquist plot of AgI after exposure to chlorine at 428 K  | 117             |
| 5.8               | Equivalent circuit based on Ershler-Randles impedance  | 118             |
| 5.9               | Equivalent circuit used for fitting AgI three electrode system at 428 K  | 119             |
| 6.1               | Layout of the sensor testing assembly  | 125             |
| 6.2               | Sketch of the sensor showing configuration of (a) front side having the electrolyte and (b) rear side having the platinum heater | 126             |
| 6.3               | Photograph of the sensor assembly  | 127             |
| 6.4               | Photograph of the electrochemical cell which was configured as sensor  | 128             |
| 6.5               | Calibration plot for screen printed platinum heater  | 129             |
| 6.6               | Baseline of the electrochemical cell containing AgI <sub>0.95</sub> Cl <sub>0.05</sub> at 428 K                                  | 130             |
| 6.7               | Typical transient for 17 vppb of chlorine gas  | 131             |
| 6.8               | Repeatability of sensor (AgI <sub>0.95</sub> Cl <sub>0.05</sub> ) towards 17 vppb of chlorine gas                                | 131             |

| <b>Figure No.</b> | <b>LIST OF FIGURES</b>   | <b>Page No.</b> |
|-------------------|--|-----------------|
| 6.9               | Calibration plot of $\text{AgI}_{0.95}\text{Cl}_{0.05}$ towards ~17 to 15000 vppb chlorine at 428 K in air | 132             |

| <b>Table No.</b> | <b>LIST OF TABLES</b>  | <b>Page No.</b> |
|------------------|--|-----------------|
| 1.1              | Half-life of iodine isotopes and cumulative yields with respect to $^{235}_{92}\text{U}$   | 6               |
| 1.2              | Half-life of iodine isotopes and cumulative yields with respect to $^{239}_{94}\text{Pu}$  | 6               |
| 2.1              | Composition and geometry of the samples studied under each characterisation  | 42              |
| 3.1              | Lattice parameters of $\text{AgI}_{1-x}\text{Cl}_x$ ( $x=0$ to $0.1$ )   | 65              |
| 3.2              | Cell volume of $\text{AgI}_{1-x}\text{Cl}_x$ where ( $x=0$ to $0.1$ )  | 66              |
| 3.3              | Value of lattice loosening for $\text{AgI}_{1-x}\text{Cl}_x$   | 67              |
| 3.4              | Concentration of $\text{Ag}^+$ ions in AgI using Atomic Absorption Spectrometer  | 75              |
| 3.5              | Concentration of $\text{Ag}^+$ ions leached from the $\text{AgI}_{1-x}\text{Cl}_x$ matrix  | 75              |
| 3.6              | Summary of binding energies of Cl 2p, I 3d and Ag 3d   | 831             |
| 3.7              | Measured ionic transference number in percentage for $\text{AgI}_{1-x}\text{Cl}_x$ at different temperatures                                 | 83              |
| 3.8              | $\beta$ -AgI to $\alpha$ -AgI phase transition temperature for $\text{AgI}_{1-x}\text{Cl}_x$ ( $x = 0-0.06$ ) from conductivity measurements | 92              |
| 4.1              | Fit parameters for the calibration plot for $\text{AgI}_{1-x}\text{Cl}_x$ towards iodine sensing   | 102             |
| 4.2              | Fit parameters for the calibration plot for $\text{AgI}_{1-x}\text{Cl}_x$ towards chlorine sensing   | 108             |
| 5.1              | Values of the circuit components used for equivalent circuit fitting   | 120             |

# CHAPTER 1

## INTRODUCTION

### 1.1 SOURCES OF IODINE AND CHLORINE

#### 1.1.1 Natural source of iodine and chlorine

The sources of iodine and chlorine in nature are multitude, starting from mineral rocks to marine organisms, as halides. A vast resource of halogen is obtained from brine (an aqueous solution of NaCl). Iodine and chlorine exists as iodide and chlorides in sea water. The least abundant of the halogen includes insoluble iodides like AgI and soluble iodates [1]. Common rock-forming minerals were reported to contain 1.2 mg/kg of iodine [2]. As reported by Fuge and Johnson [2], the iodine content in the rocks reaches the soil by the process of weathering. Thermodynamically iodide and iodates are the only stable forms of iodine existing in nature [3].

In the case of chlorine, apart from sea water, chlorinated alkaloids are concentrated in various plants and amphibians that are medicinal in nature [4]. The sediments from volcanic eruptions are carried to the earth's crust, mainly containing the fluorides and chlorides, which are eventually brought into earth's atmosphere. About  $2.6 \times 10^{16}$  metric tons of chlorine is present in ocean [5].

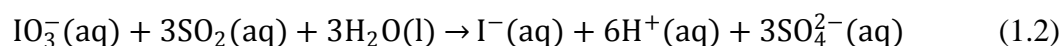
#### 1.1.2 Processes involving the production of iodine and chlorine in industrial scale

##### 1.1.2.1 Production of iodine [6]

Iodine can be extracted from brine and also from the nitrate ores. Brine, close to oil and natural gas fields contains 100-150 ppm iodine as iodide, depending on the source. After acidification with  $H_2SO_4$ , the brine is chlorinated to liberate iodine.



Nitrate ores situated in Chile contains 95 %  $\text{NaNO}_3$  and 5 % sodium iodate. After the removal of nitrate by crystallisation, the decanted solutions are treated with  $\text{SO}_2$ . The reaction is as follows:

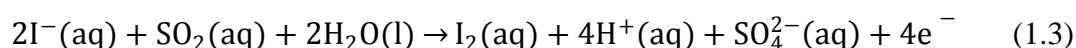


The final solution is then mixed with  $\text{IO}_3^-$  to give free iodine.

The crude iodine obtained from brine undergoes refining process. There are two processes for refining iodine produced from brine:

(a) Blowing out method [6]:

A counter current mixing of air and iodine is done, after which the air containing iodine is passed through a tower having hydroiodic and sulphuric acid. This solution is further treated with sulphur dioxide solution reducing iodide to iodine as given in the equation below:



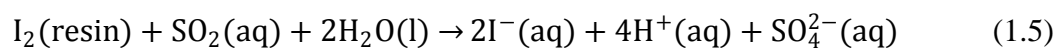
The solution is then reacted with chlorine and the iodine produced is allowed to settle, re-melted and then flaked. As given in equation (1.1), the iodine vapours are produced after reaction with chlorine.

(b) Ion exchange method [6]

The iodine obtained from the brine is treated with  $\text{I}^-$  solution to form  $\text{I}_3^-$  as given in equation below:



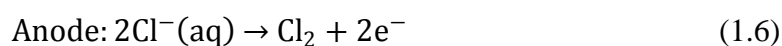
An anionic exchange resin is used, which will adsorb  $\text{I}_3^-$ . This resin is then loaded in another column where aqueous solution of  $\text{SO}_2$  drops, finally giving iodide solution, as given in equation (1.5).



As in the blowing out process, the solution is heated again with chlorine to liberate iodine which is further purified.

#### 1.1.2.2 Production of chlorine

Major part of industrial chlorine is prepared by electrolysis process. Underground rock salt contains high purity brine. The brine is pumped to the surface using water. Electrolysis of brine gives chlorine gas at the anode. The anode and the cathode reactions are as follows:



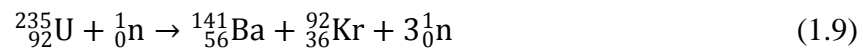
Mixing of by-products, NaOH and Cl<sub>2</sub>, formed in the above reaction eventually reacts to form NaOCl. To minimise the mixing of the products formed, various methods are employed in industry. The processes used for production of chlorine, to minimise the mixing of by-products, based on the electrolysis are:

- (a) **Cation exchange membrane cell:** the membrane allows only the cation to cross between brine and caustic compartment thereby controlling the side reaction leading to the formation of NaOCl.
- (b) **Mercury amalgam cell:** sodium ions are transferred as mercury-sodium amalgam thereby reducing the available free sodium for the side reaction.
- (c) **Percolating diaphragm cell:** the diaphragm percolates only brine from anode to cathode. It separates chlorine and hydrogen gas spaces by using asbestos. The migration of OH<sup>-</sup> ions from the cathode to the anode is prevented by the velocity of liquid flow against them. The physical partition prevents the intermixing of Cl<sub>2</sub> and NaOH formed during the electrolysis.

## 1.2 IODINE AND CHLORINE IN NUCLEAR INDUSTRY

### 1.2.1 Thermal reactor [7]

Since 1950s, the development of the power generation based on the reactors has started in India. The thermal reactors use natural uranium ( $^{238}\text{U}$  (99.2 %) and  $^{235}\text{U}$  (0.72 %)) or enriched uranium (3-4 %  $^{235}\text{U}$ ) [8]. The typical fission reaction for  $^{235}\text{U}$  in a thermal reactor is given in equation (1.9):



Cooling of the reactors in the primary containment is done either by gases like  $\text{CO}_2$  (gas cooled reactor) or by light or heavy water (Light water reactor, Pressurised Heavy Water Reactor (PHWR) and Boiling Water Reactor (BWR)). The usage of moderator for slowing down the neutrons is important in thermal reactors as the maximum yield of neutrons occurs for natural uranium in the thermal region (25 meV). Graphite rods are used in thermal reactors as moderator, whereas other thermal reactors employ the cooling water itself as the moderator. The purpose of the moderator is to reduce the kinetic energy of the neutrons to the thermal region. Neutron absorbers like cadmium or boron is used as control rods in thermal reactors, which controls the fission reaction by absorbing the excess neutrons. The schematic of a pressurised heavy water reactor is shown in Fig. 1.1.

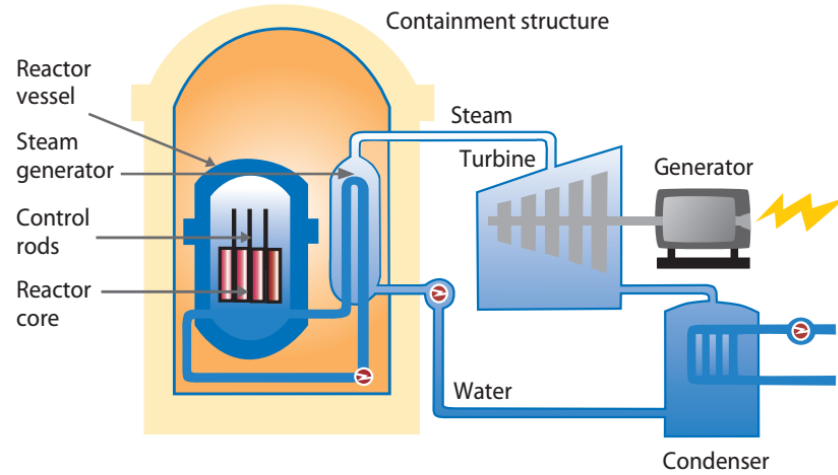
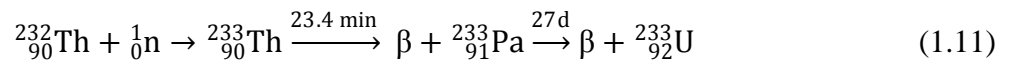
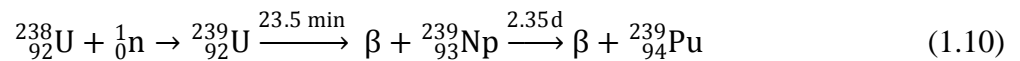


**Fig. 1.1 Schematic of pressurized heavy water reactor [7]**

### 1.2.2 Fast reactors [7]

The need for more fissile materials to sustain future reactors has led to the idea of breeding the fissile matter within the reactor. Fast reactors make its advent to introduce the breeding of the fissile nuclei of  $^{239}\text{Pu}$  and  $^{233}\text{U}$  from the existing natural uranium ( $^{238}\text{U}$ ) and  $^{232}\text{Th}$ . The two major breeder reactions taking place in fast reactors are:



Generally, the fuel is made of mixed oxides or carbides. As the thermal output is higher than that of thermal reactors, materials with good thermal conductivity must be used as a coolant for removal of heat. Thus, liquid sodium with wide physical, chemical and nuclear properties is employed in fast reactors as primary coolant. There are no moderators in fast reactors. The control rods are mainly made of boron carbide. The sketch of the fast breeder test reactor is shown in Fig. 1.2. Apart from the primary cooling system, there will be secondary coolant, again employing liquid sodium, which exchanges the heat between sodium and steam in the steam generators. Eventually, the thermal energy from the steam generators is converted into electrical power.

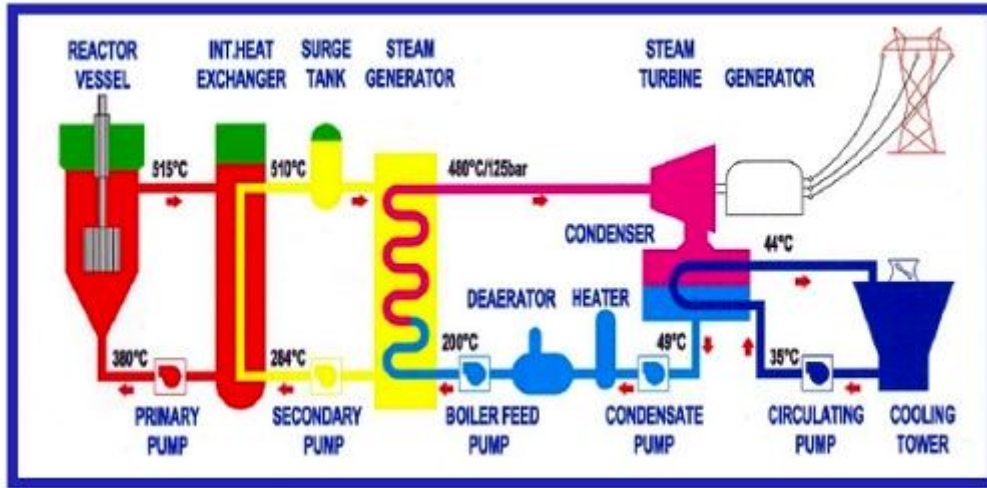


Fig. 1.2 Sketch of FBTR at Kalpakkam [9]

### 1.3 IODINE IN NUCLEAR INDUSTRY

Iodine is one of the major fission products in nuclear industry with a range of isotopes produced during the fission reaction in a reactor. The major isotopes of iodine which are produced are given in Table 1.1 and 1.2.

Table 1.1 Half-life of iodine isotopes and cumulative yields with respect to  $^{235}\text{U}$  [10]

| Sl.No | Nuclide          | Half-life           | Yield in thermal reactor (% per fission) | Yield in fast reactor (% per fission) |
|-------|------------------|---------------------|--|---------------------------------------|
| 1.    | $^{129}\text{I}$ | $1.57 \cdot 10^7$ y | $1.407 \pm 0.086$                        | $1.31 \pm 0.13$                       |
| 2.    | $^{131}\text{I}$ | 8 d                 | $3.724 \pm 0.078$                        | $4.09 \pm 0.12$                       |
| 3.    | $^{133}\text{I}$ | 20.8 h              | $6.97 \pm 0.13$                          | $6.99 \pm 0.33$                       |
| 4.    | $^{135}\text{I}$ | 6.57 h              | $6.33 \pm 0.23$                          | $6.24 \pm 0.22$                       |

Table 1.2 Half-life of iodine isotopes and cumulative yields with respect to  $^{239}\text{Pu}$  [10]

| Sl.No | Nuclide          | Half-life           | Yield in thermal reactor (% per fission) | Yield in fast reactor (% per fission) |
|-------|------------------|---------------------|--|---------------------------------------|
| 1.    | $^{129}\text{I}$ | $1.57 \cdot 10^7$ y | $0.706 \pm 0.032$                        | $1.03 \pm 0.26$                       |
| 2.    | $^{131}\text{I}$ | 8 d                 | $2.878 \pm 0.032$                        | $3.365 \pm 0.054$                     |
| 3.    | $^{133}\text{I}$ | 20.8 h              | $6.59 \pm 0.11$                          | $6.61 \pm 0.13$                       |
| 4.    | $^{135}\text{I}$ | 6.57 h              | $6.39 \pm 0.22$                          | $6.01 \pm 0.18$                       |

Among the iodine isotopes,  $^{129}\text{I}$  is the radioisotope of concern because of its high half-life.

During any accidental leak from the reactor, the isotope  $^{129}\text{I}$ , if ingested, will take longer

time to decay. Iodine is produced both in thermal and fast reactor as a fission product. During a breach in the fuel pin, in the case of reactor, there will be release of fission products into the adjacent cooling system. In thermal reactors, the formation of HI during the reaction with the coolant water surrounding the core will further dissociate in the presence of oxygen (occurring due to air ingress) to form free iodine as given in the equation (1.12).



In the case of fast reactors, iodine leaking out during a breach in the fuel pin reacts with sodium to give sodium iodide. Sodium iodide, during a major accident can be released into the air. In such situations, equilibrium is established between NaI and oxygen in air releasing iodine gas [11] as given in equation (1.13).



### **1.3.1 Role of chlorine in pyroprocessing of spent nuclear fuels**

In view of the large amount of spent fuel being progressively added to the cumulative inventory in the world, the significance of spent fuel management will continue to grow [12]. For closing the fuel cycle, either aqueous or non-aqueous routes of reprocessing can be adopted. In aqueous reprocessing, after the process of chopping and acidic dissolution of used fuel pins, an organic extractant like, tributylphosphate (TBP) is used to recover the useful fissile materials.

Pyroprocessing is an alternate way for reprocessing the spent nuclear fuel for reuse as fresh fuel for the next reactor. It falls in the category of “Partitioning and Transmutation” (P&T) concept for the recovery of useful fuel from the spent fuel rather than disposing the spent fuel in repositories [13]. The method uses simple inorganic compounds in the process as electrolyte bath. This process gives an advantage for handling high burn-up (shorter cooling time) fuels to be reprocessed. Fuel burn-up is the total amount of thermal

energy generated per unit quantity of heavy element charged to the core [14]. Also the ease in handling the advanced fuels like metallic, nitride, carbide and CERMET (materials made of ceramic and sintered metal) fuels for cycling becomes easier with pyroprocessing as it is difficult to dissolve such fuels in aqueous reprocessing route. A schematic of pyroprocessing is shown in Fig. 1.3.

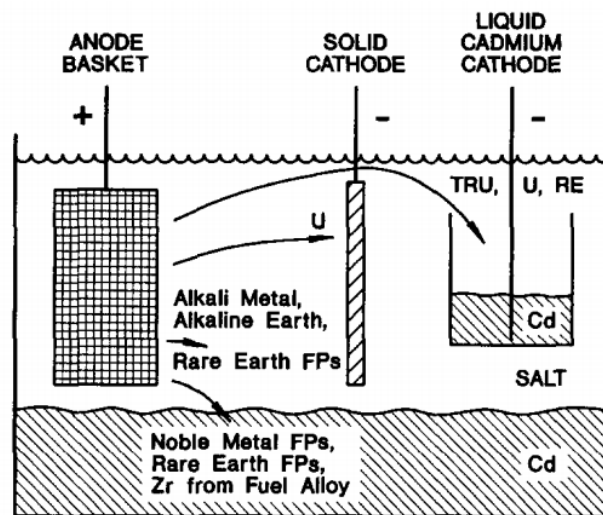
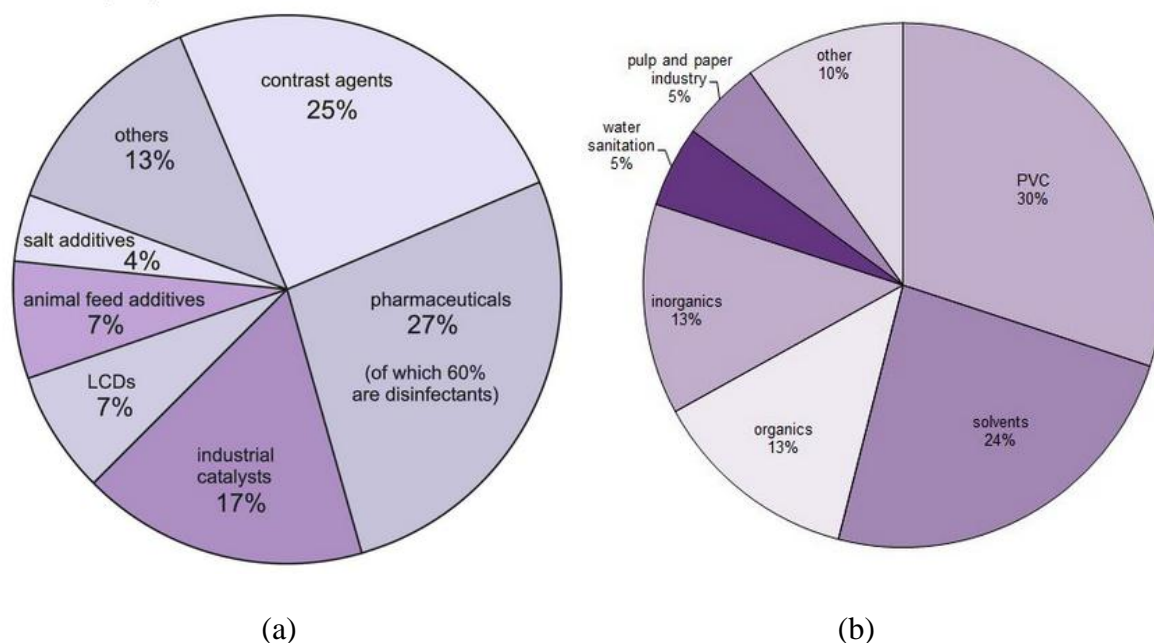


Fig. 1.3 Schematic of pyroprocessing electrochemical cell [15]

Pyroprocessing involves electrorefining of the spent fuel from the reactors using an electrochemical cell. The anode of the cell is a basket filled with the spent fuel. There are two cathodes in the reprocessing of non-aqueous spent fuel. A solid cathode will accumulate pure uranium when the desired potential is applied across the cell. A mixture of transuranic elements, uranium and rare earth fission products migrates to the cadmium cathode. Depending on the stability of other chlorides, other salts will distribute either in Cd or salt (LiCl-KCl) melt [15]. Chlorine is a major constituent in pyroprocessing sector, where copious amounts of chlorine gas are used for purging the electrochemical cell containing the LiCl-KCl bath.

## 1.4 APPLICATIONS OF IODINE AND CHLORINE

Iodine and chlorine play key roles in various industries due to their oxidising nature. Chlorine and iodine have similar chemical characteristics. Being the most abundant among the halogens, chlorine is used as a bleaching agent in paper industry and as a germicide in water purification systems as it is a major constituent in dettol [16]. Chlorine is used widely in the production of PVC and epoxy resin based materials. Iodine is a major constituent in the biological system as it plays a significant role in the functioning of thyroid gland. Iodine is one of the major elements employed in medical field, where it is used in X-ray imaging as a contrast agent. Alcohol solutions of iodine were once used



**Fig. 1.4** Pie chart representing the industrial uses of (a) iodine and (b) chlorine [5 & 6]

as an antiseptic [16]. Various sectors utilising iodine and chlorine are shown in the Pie chart given in Fig. 1.4. The medical industry and the plastic industry share the major hold for the usage of iodine and chlorine.

## **1.5 EFFECT OF EXPOSURE OF RADIOACTIVE IODINE [17-19]**

Iodine consumed from food is concentrated in thyroid gland, which controls the hormonal balance in the body of human beings. During radioactive fallouts, the radioiodine in atmosphere can get ingested into the body. Like the normal iodine, radioiodine also concentrates in the thyroid gland and causes damage to the thyroid. The primary risk is the cause of radiogenic thyroid cancer in the ingested human, later in the lifetime. Other than the thyroid cancer, possibility of non-cancerous growth and thyroiditis are involved as risks. The risk of thyroid cancer is dependent on age. Children and teenagers are more affected than adults. The risk can be mitigated by taking iodine supplements, raising the total iodine content in the body, reducing the uptake of radioiodine by thyroid gland. Inactive iodine also plays the same significance as radioiodine, except the presence of radioactivity. The daily intake of iodine by a normal adult is around 150 µg, beyond which the accumulation of excess iodine will lead to hyperthyroidic disorder [20]. Iodine induced hyperthyroidism may be transient or permanent and the risk factor include non-toxic and diffuse nodular goitre, latent Grave disease and long standing iodine deficiency [21]. Iodine induced hyperthyroidism in euthyroid patients with nodular goitre in iodine sufficient areas has also been reported when iodine supplementation is excessive [22]. The permissible level of intake for iodine is 8-30 µg/ person/day [23].

## **1.6 EFFECT OF EXPOSURE TO CHLORINE [24-26]**

A short term exposure to chlorine causes burning of eyes, nose and throat. But, these symptoms subside when the exposure is stopped. The severity of consequence increases with more serious exposure to the gas. Large amount of chlorine when breathed-in causes the swelling of lining of throat and lungs, making breathing difficult. Trachibronchitis, pulmonary edema and pneumonia have been reported with severe exposure of chlorine. At high concentrations, approximately 400 vppm of chlorine gas can be fatal over the

time duration of 30 min whereas a concentration of 1000 vppm causes fatality within a few minutes. The threshold limit value for chlorine is 0.5 vppm [27].

## **1.7 DIFFERENT METHODOLOGIES FOR SENSING HALOGENS AND HALIDE IONS**

### **1.7.1 Conductometric mode of sensing iodine vapour**

Generally, the sensing material in a conductometric sensor will be a layer of semiconductor or a polymer or a gel, whose change in the resistance or capacitance, is related to the concentration of the analyte gases injected [28]. A rather simple design consists of two electrodes with the sensitive layer on top of these electrodes. These sensing materials require large surface area and a specified geometry as the conductance is derived from the dimension of the cell. The conductivity is generally measured as:

$$\frac{1}{R} = \sigma * \frac{A}{l} \quad (1.14)$$

where R is the resistance of the material,  $\sigma$  is the conductivity; A is the surface area of the sensing material and  $l$  is the thickness of the sensing layer. Polymer based long chain acetylenes were reported to sense iodine vapours [29]. The conducting polymers contain alternate double and single bonds. The degree of delocalisation, steric factors and charge interactions lead to the formation of forbidden band gaps. The enhancement of conductivity due to the introduction of the suitable doping elements to the polymers to tune the band gaps and in-turn tune them for the proper interaction with the analyte gas gives them an added advantage for the sensing application. The limit of detection was reported to be around 10 vppm of iodine.

### **1.7.2 Optical sensing of iodide in solution**

Certain gases are having optical properties intrinsically within them. The optical properties of such analytes can be evaluated in many cases to obtain concentration dependent chemical signals without a mediator. The mediator refers to the sensor material, which changes its optical characteristics in the presence of the analyte [28]. The

phenomenon of fluorescence takes place when a molecule returns from the lowest excited state to one of the vibrational states in the ground state. The emitted radiation will have lower frequency compared to that of the excited radiation. The process happens in an interval of  $10^{-6}$ - $10^{-8}$  s [28]. 9-ethyl-3-carbazylidene carbazole hydrazone was tested based on the fluorescence emission of the material in the presence of different concentration of iodine in solution [30]. The reduction in the fluorescence intensity was observed with increasing concentration of the iodide in micro molar level.

### 1.7.3 Potentiometric mode for sensing iodine vapours

Most of the reported literature shows the usefulness of potentiometric mode of sensing of halogens. An electrochemical cell based on CsI added AgI for sensing iodine in trace levels was reported by Sola et al. [31]. The reported article discusses the use of Ag|AgI(CsI)|graphite cell, whose characteristics towards iodine vapour was studied from 39-519 Pa (385-5122 vppm). The document elaborates on the diffusion of iodine through the pellet and provides a mathematical treatment of the concentration of iodine at a given time  $t$  and the condition of equilibrium of iodine with the pellet. The ratio of the emf at time  $t$ ,  $E_t$  after admitting the respective partial pressure of iodine to the baseline emf  $E$  was plotted against time for evaluating the sensor. A sketch of the sensor reported is represented in the Fig. 1.5.

The change in the emf was based on the Nernst equation for the cell represented as in equation (1.15) [31]:

$$E = \frac{RT}{2F} \ln p_{I_2} \quad (1.15)$$

where  $R$  is the universal gas constant,  $T$  is the absolute temperature,  $F$  is the Faraday's constant and  $p_{I_2}$  is the partial pressure of iodine admitted. The increase in the partial pressure of the gas was envisaged as an increase in the emf of the electrochemical cell.

An ion selective electrode was tested based on room temperature  $\beta$ -AgI for sensing iodide

in solution [32]. Functionalised ZnO and miconazole coated ZnO was reported to sense iodide in solution from 1  $\mu$ M to 0.1 M at room temperature based on potentiometric mode of sensing [33].

#### 1.7.4 Conductometric sensors for chlorine using organometallic compounds

Derivatives of phthalocyanines were reported to sense chlorine gas in conductometric mode. Zn(II)2,3,9,10,16,17,23,24-octakis(octyloxy)-29H,31H-phthalocyanine (ZnPcOC<sub>8</sub>) nanowires and nanoflowers of Cu(II)2,3,9,10,16,17,23,24-octakis(octyloxy)-29H, 31H-phthalocyanine (CuPcOC<sub>8</sub>) were reported to sense chlorine down to ~ 5 vppb of chlorine gas at room temperature based on conductometric mode of sensing [34]. The oxygen in the ambience was reported to bind with phthalocyanine forming MPc<sup>+</sup> and O<sub>2</sub><sup>-</sup> responsible for p-type conduction as shown in equation (1.16): [34]



Antimony-doped SnO<sub>2</sub> sensors were reported to sense chlorine gas down to 3 vppm at room temperature [35]. Heavily doped SnO<sub>2</sub> was found to be a highly conducting material, whereas in the presence of the oxidising gas, chlorine, the depletion layer is created due to the charge transfer at the grain boundary interface giving rise to the sensing action. Fig. 1.6 depicts the mode of sensing for antimony doped SnO<sub>2</sub>.

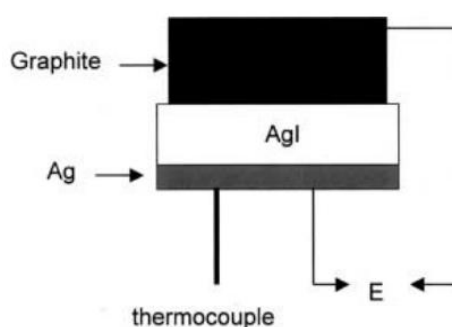
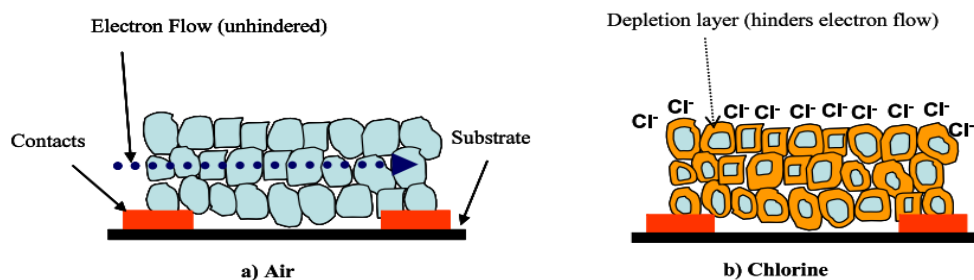


Fig. 1.5 Schematic of the potentiometric sensor used for measuring the iodine concentration [31]



**Fig. 1.6 Schematic of (a) high conduction (channel for electron transfer) of antimony-doped SnO<sub>2</sub> in air and (b) reduced conduction in the presence of chlorine gas [34]**

A compilation of the materials for chlorine sensing was given in the literature of Chaparadza and Ranannavare [35]. The materials vary from ZnO to nickel ferrates with detection limit varying from 0.01-1000 vppm of chlorine gas at different temperatures [36-49].

### 1.7.5 Potentiometric sensing of chlorine

The use of auxiliary electrodes was discussed in paper of Hotzel and Weppner [50] and Weppner [51]. Both the literature describes the study on the partial pressure determination of chlorine in trace levels using AgCl as the auxiliary electrode. Menne and Weppner [52] reported the use of thermally evaporated AgCl over the Ag-β"-Al<sub>2</sub>O<sub>3</sub> (electrolyte) to sense chlorine. The chlorine concentration tested using the electrolyte was around 1 vppm to 100 % in air.

### 1.7.6 Optical sensing of chlorine

Carbon dots covered with rhodium boride were reported to sense free chlorine in water, based on the change in the intensity of fluorescence of the carbon dots due to exposure to free chlorine. The ratio of the fluorescence intensities at 445 and 580 nm were found to reduce in the presence of free chlorine in the solution in micro molar quantities [53].

## **1.8 SALIENT FEATURES AND LIMITATIONS OF CONDUCTOMETRIC, OPTICAL AND POTENTIOMETRIC MODE OF SENSING**

The sensitivity of polymer based conductometric sensors as well as the use of various semiconducting oxides is very high. The fabrications of such films are also easier than other methods of sensing. Even though the reported literature proves the usefulness of various polymer materials for sensing halogen at trace levels, the output signal of the material is geometry dependent and also the use of such organic molecules in the oxidising nature of iodine and chlorine gases will cause damage to the chemical structure of these moieties reducing the life of the sensor material.

The major advantages of fluorescence based sensors include their simple designs without reference electrode and a sensor configuration without the necessity of two probes for sensing. The optical signal produced by the sensor material does not interfere with electrical signals and the miniaturisation is also easier. The output can be transferred from a remote area by suitably integrating with fibre optics configuration for remote sensing. The major setbacks involve the interference from ambient light and the bleaching of the fluorescent dyes by the UV-radiation [28].

The geometry independent design for potentiometric sensors makes it simpler for applying different configurations of the material to be used for the purpose. Also the potentiometric sensors can be used in wide dynamic range due to the logarithmic behaviour of the concentration against the emf. The major disadvantages include the use of high input impedance for the measurement, as any stray current passing through the cell will cause the baseline emf to drift.

## **1.9 DETERMINATION OF RADIOACTIVE IODINE**

NaI, hyper pure germanium and organic liquid scintillation detectors are used to measure the gamma and X-radiation emitted from  $^{125}\text{I}$  and  $^{131}\text{I}$  [54]. Gamma ray of energy 28 keV (0.0665 photons/transition) and  $K\alpha_1$  and  $K\alpha_2$  X-rays of energy 27.5 keV (0.739

photons/transition) and 27.2 keV (0.397 photons/transition) are generally used for quantification of these radioisotopes. Isotopes of I<sup>125</sup> and I<sup>131</sup> are identified based on the K $\beta$ <sub>1</sub> and K $\beta$ <sub>2</sub> transition at 31.0 keV (0.140 photons/transitions) and 31.7 keV (0.043 photons/transition) [55, 56].

In the following sections, fundamental theory governing the function of potentiometric mode of sensing is described. Further, details and applications of solid electrolytes used in potentiometric sensors are discussed.

### 1.10 THE CONCEPT OF GIBBS ENERGY

In thermodynamics, Gibbs energy of a system is defined as,

$$G = H - TS \quad (1.17)$$

where G is the Gibbs energy, H is the enthalpy, T is the absolute temperature and S is the entropy of the system. As H and S are state functions G is also a state function.

For an infinitesimally small change in the system from state 1 to 2:

$$dG = dH - TdS \text{ (at constant temperature)} \quad (1.18)$$

$$\Rightarrow \int_1^2 dG = \Delta G = \Delta H - T\Delta S \text{ (at constant temperature)} \quad (1.19)$$

From the definition of the enthalpy change of a system:

$$dH = dU + PdV = \delta q - \delta w + PdV + VdP \quad (1.20)$$

where U is the internal energy of the system and PV represents the pressure-volume work done, 'w' and q is the heat energy associated with the change.

$$\text{Hence, } dG = \delta q - \delta w + PdV + VdP - TdS \text{ (at constant temperature)} \quad (1.21)$$

As  $\delta w$  and  $\delta q$  are the infinitesimal change in pressure-volume work (PdV) and heat energy associated with the system. Considering an infinitesimal change in the temperature, the above equation can be rewritten as:

$$dG = \delta q + VdP - TdS - SdT \quad (1.22)$$

$$\text{From the definition of entropy: } \delta q = TdS \quad (1.23)$$

$$\text{Hence, } dG = VdP - SdT \quad (1.24)$$

Equation (1.24) shows the dependence of Gibbs energy on pressure and temperature. For an isothermal change, equation 1.24 can be rewritten as:

$$\int_{G^0}^G dG = \int_{P^0}^P V dP \quad (1.25)$$

where  $G$  and  $G^0$  are the Gibbs energies at pressure  $P$  and at the standard state of the system with pressure  $P^0 = 1$  bar. Equation (1.25) can be rewritten for one mole of an ideal gas ( $R$  being the universal gas constant) as:

$$G - G^0 = \int_{P^0}^P \frac{RT}{P} dP \quad (1.26)$$

$$\Rightarrow G - G^0 = RT \ln \frac{P}{P^0} \quad (1.27)$$

Considering the standard state with pressure  $P^0$  as 1 bar and  $n$  moles of the gas, the above equation modifies as:

$$G - G^0 = nRT \ln P \quad (1.28)$$

Considering a chemical reaction:



The Gibbs energy change for the chemical reaction can be written as:

$$\Delta G = \sum G_{\text{products}} - \sum G_{\text{reactants}} \quad (1.30)$$

$$\Delta G = cG_C + dG_D - (aG_A + bG_B) \quad (1.31)$$

Thus, for the given chemical reaction:

$$\Delta G = cG_C^0 + dG_D^0 - (aG_A^0 + bG_B^0) + cRT \ln p_C + dRT \ln p_D - (aRT \ln p_A + bRT \ln p_B) \quad (1.32)$$

where  $G_A^0$ ,  $G_B^0$ ,  $G_C^0$  and  $G_D^0$  are the standard Gibbs energy for the reactants and the products and  $p_A$ ,  $p_B$ ,  $p_C$  and  $p_D$  are the arbitrary pressures of the reactants and products. Equation (1.32) can be rewritten as

$$\Delta G = \Delta G^0 + RT \ln \left( \frac{p_C^c \cdot p_D^d}{p_A^a \cdot p_B^b} \right) \quad (1.33)$$

where  $\Delta G^{\circ} = cG_C^{\circ} + dG_D^{\circ} - (aG_A^{\circ} + bG_B^{\circ})$ . The product of the pressures in the above equation represents a form of equilibrium constant (K). However, the product will be equal to the equilibrium constant when all the arbitrary pressures ( $p_A$ ,  $p_B$ ,  $p_C$  and  $p_D$ ) are in equilibrium. At equilibrium,

$$\Delta G = 0 \quad (1.34)$$

$$\text{Equation (1.33) becomes: } \Delta G^{\circ} + RT\ln(K) = 0 \quad (1.35)$$

$$\Rightarrow \Delta G^{\circ} = -RT\ln K \quad (1.36)$$

### 1.10.1 Relation between Gibbs energy and emf in an electrochemical cell

During an electrochemical reaction, there will be associated voltage or cell potential which can be related to the Gibbs energy change for the cell. To understand the relation between the two parameters, let us reconsider the definition of Gibbs energy:

$$dG = dU + PdV + VdP - SdT - TdS \quad (1.37)$$

$$dG = \bar{d}q_{\text{res}} - \bar{d}w_{\text{max}} + PdV - TdS \quad (1.38)$$

Equation (1.38) is valid for a reversible process occurring at constant temperature and pressure. Also, the system can do maximum work ( $\bar{d}w_{\text{max}}$ ) during a reversible process. As heat change associated with the process,  $\bar{d}q_{\text{res}} = TdS$ , equation (1.38) can be simplified as:

$$dG = -\bar{d}w_{\text{max}} + PdV \quad (1.39)$$

$$\text{or } \Delta G = -\bar{d}w_{\text{max}} + P\Delta V \quad (1.40)$$

During a chemical reaction in the electrochemical cell, the system not only does the pressure volume work ( $PdV$ ) but, also transfers the electric charge through an external circuit. The electrochemical cell can be operated reversibly by connecting the leads of the cell to a high impedance circuit which draws infinitesimally small current when connected to the electrochemical cell. Thus, the reversible work done by the electrochemical cell

will be the total of the work done by means of electric charge transfer ( $w_{\text{ele}}$ ) and the pressure-volume work ( $w_{\text{PV}}$ ).

$$\text{Therefore, } w_{\text{max}} = w_{\text{ele}} + w_{\text{PV}} \quad (1.41)$$

$$\Rightarrow \Delta G = -(w_{\text{ele}} + w_{\text{PV}}) + P\Delta V \quad (1.42)$$

$$\therefore \Delta G = -w_{\text{ele}} \quad (1.43)$$

If the Gibbs energy change in the cell is negative, the system does electrical work on the surrounding and if the Gibbs energy change is positive, the work will be done on the system by surrounding.

The potential difference ( $\Delta E$ ) across the two leads of the electrochemical cell is equivalent to the work done in transferring a unit charge between them. Therefore, for transferring 'nF' charge across the leads, the Gibbs energy can be represented as:

$$\Delta G = -nF \cdot \Delta E \quad (1.44)$$

where F is the Faraday constant and n is the number of moles of charge transferred.

The experimentally observed cell potential depends on the nature of the reactant and products and also on the temperature of operation. To compare the voltages different electrochemical cells on a common basis, standard voltage ( $\Delta E^0$ ) is used. This standard voltage can be correlated with the standard Gibbs energy ( $\Delta G^0$ ) as:

$$\Delta G^0 = -nF \cdot \Delta E^0 \quad (1.45)$$

Considering the chemical reaction in equation (1.29) and assuming arbitrary concentration A, B, C and D for the reactants and the products, equation (1.33) can be rewritten as:

$$\Delta G = \Delta G^0 + RT \ln \left( \frac{C^c \cdot D^d}{A^a \cdot B^b} \right) \quad (1.46)$$

Substituting the relation between Gibbs energy and the cell potential in the above equation gives:

$$-nF \cdot \Delta E = -nF \cdot \Delta E^0 + RT \ln \left( \frac{C^c \cdot D^d}{A^a \cdot B^b} \right) \quad (1.47)$$

$$\Delta E = \Delta E^0 - \frac{RT}{nF} \ln \left( \frac{C^c \cdot D^d}{A^a \cdot B^b} \right) \quad (1.48)$$

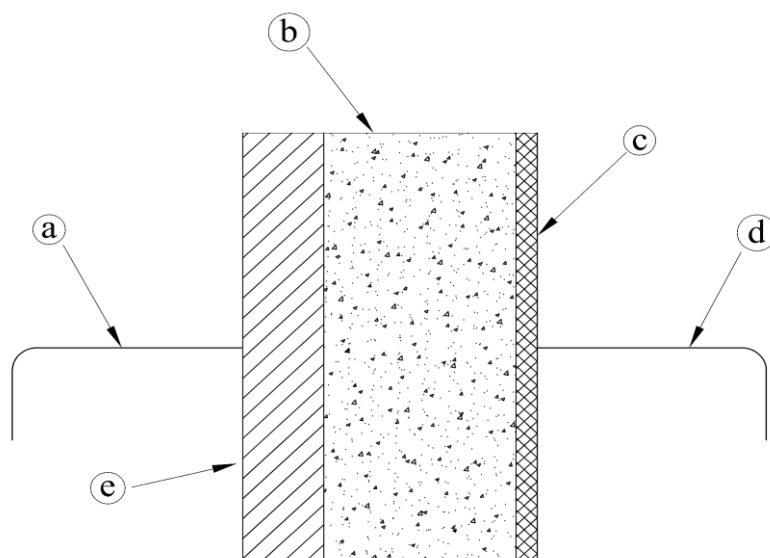
Equation (1.48) is known as the Nernst equation which relates the cell potential to the concentration of the reactants and products and also to the temperature of the electrochemical cell. Under equilibrium conditions, when there is no net transfer of charges, the cell potential goes to zero. Therefore, equation (1.48) can be rewritten as:

$$\Delta E^0 = -\frac{RT}{nF} \ln \left( \frac{C^c \cdot D^d}{A^a \cdot B^b} \right) \quad (1.49)$$

The condition of equilibrium is maintained when all the leads will attain the same potential and the charge transfer ceases across the leads.

### 1.11 ELECTROCHEMICAL SENSORS BASED ON SOLID ELECTROLYTE [51]

A marked difference between the potentiometric sensors against other modes of sensing is its significance in miniaturisation (as solid electrolytes are used) and also its geometrical



- |                                  |                                |
|----------------------------------|--------------------------------|
| (a) Lead for reference electrode | (d) Lead for working electrode |
| (b) Solid electrolyte            | (e) Reference electrode        |
| (c) Working electrode            |                                |

**Fig. 1.7 Sketch of a potentiometric sensor**

independent configuration. In addition to the above mentioned advantages, the wide dynamic range incorporation due to the logarithmic relation to the concentration makes it more useful in various applications. A sketch of the potentiometric sensor is shown in Fig. 1.7. Generally, in any potentiometric sensor, the activity of the element of interest at the reference electrode will be fixed at a constant value whereas its activity on the working electrode/electrolyte interface will be varying with the analyte gases admitted. Solid electrolyte based electrochemical sensors were classified into three category by Weppner into Type I, II and III ionic conductors depending on the determination of the partial pressure under conditions of equilibrium or electric current by applying an external voltage, across the solid electrolyte .

(a) Type I ionic conductor

This ionic conductor is based on the development of an emf across the solid electrolyte due to activity change across the reference-electrode|solid-electrolyte and solid-electrolyte|working-electrode interface. On the working electrode interface, the electrolyte will equilibrate with the gas phase and behaves as a permeable lead for the measurement. At the electrode|electrolyte interface there will be a potential drop. The chemical potential with respect to electrons is identical for both the reference and the working electrode due to high number density of electrons. The Nernst equation for the cell can be represented as:

$$E = \frac{kT}{z_i q} \ln \left( \frac{a_i^*'}{a_i^{*''}} \right) = \frac{1}{z_i q} (\mu_i^{*'} - \mu_i^{*''}) \quad (1.50)$$

where k is the Boltzmann constant, T is the absolute temperature,  $z_i$  is the number of electrons taking part in the electrochemical reaction, q is the elementary charge ( $1.602 \times 10^{-19}$  C),  $a_i^*$  and  $\mu_i^*$  represents the activity and chemical potential of the neutral species 'i' and ' and '' refers to the reference and the working electrode.

Thus activity and partial pressure ( $p_i$ ) for the component is related by the equation as:

$$\mu_i = \mu_i^0 + kT \ln a_i = \mu_i^0 + kT \ln p_i \quad (1.51)$$

where "0" represents the standard state.

During a continuous transition from electronic to ionic conduction the voltage will be reduced by a factor as shown in equation (1.52).

$$\Delta E = -\frac{1}{z_i q} \int t_e d\mu_i^* \quad (1.52)$$

where  $t_e$  is the transference number of the electrons.

(b) Type II ionic conductors

In these types of conductors, the partial pressure is determined for the component which is different from the predominantly mobile species. In such electrochemical cells:

$$SdT - VdP + \sum_i n_i d\mu_i^* = 0 \quad (1.53)$$

where S, V and  $n_i$  are entropy, volume and number of species of the component 'i'. T represents the temperature and P is the pressure. The Gibbs energy and the absolute values of chemical potential are related by:

$$G = \sum_i n_i \mu_i^* \quad (1.54)$$

$$\Delta G_f^0 = \sum_i n_i (\mu_i^* - \mu_i^0) = kT \sum_i n_i \ln a_i^* \quad (1.55)$$

where  $\Delta G_f^0$  is the standard Gibbs energy of the formation. The above relation holds only for binary compounds  $A_i B_j$ . The chemical potential difference at both the interface is given as:

$$\mu_i^{*' } - \mu_i^{*''} = -\delta (\mu_j^{*' } - \mu_j^{*''} ) \quad (1.56)$$

where ' and '' are the interface of reference and working electrode respectively.  $\delta$  represents the correlation for the valencies of  $A_i$  and  $B_j$  as  $z_i = -\delta z_j$ .

For an electrochemical cell with fixed activity of the reference electrode can be represented by the Nernst equation given below:

$$E = \frac{\mu_i^* - \mu_i^{*'}}{z_i q} = \frac{RT}{nF} \ln \left( \frac{a_i^*}{a_i^{*'}} \right) \quad (1.57)$$

If the activity of the reference electrode is fixed as unity, then the emf of the cell reduces to:

$$E = \frac{RT}{nF} \ln \left( \frac{1}{a_i^*} \right) \quad (1.58)$$

(c) Type III ionic conductors (amperometric gas sensors)

In such ionic conductors, the electric current or change in electric current is measured across the solid electrolyte through an external circuit by applying a voltage E. The cell voltage for such ionic conductor is given as:

$$E = I \int_0^x (\sum_i \sigma_i)^{-1} dx - q^{-1} \int_0^x \sum_i \left( \frac{t_i}{z_i} \right) d\mu_i \quad (1.59)$$

where x and  $\sigma$  represents the diffusion length and electrical conductivity. The control on the kinetics and also the cell reaction can be achieved by using such amperometric cells. The selectivity of such sensors is also very high when the electrolyte is used as a membrane. Such cell reactions are controlled by diffusion:

$$J = -D \frac{dc_i}{dx} = -D \frac{\Delta c_i}{d} \quad (1.60)$$

where  $\Delta c_i$  is the concentration difference across the membrane of thickness d and D is the effective diffusion coefficient. Based on the knowledge of d and D, the concentration of the gas independent of the reference electrode can be calculated.

## 1.12 OTHER APPLICATIONS OF POTENTIOMETRIC CELLS USING SOLID ELECTROLYTES

Solid electrolytes used for potentiometric applications are basically of three types: simple or complex halides, simple or complex oxides or oxide solid solutions. The uniqueness in structure of solid electrolytes gives them the highest conductivities in solid state compared to materials having intrinsic defects ( $\sim 10^{-3} \Omega^{-1} \text{ cm}^{-1}$ ). These solids act as an impervious barrier to gases and liquids, conducting only through one or more ions either under the influence of an external voltage or a chemical potential gradient [57]. Thus, solid electrolytes loaded potentiometric cells can be used for the following applications:

(a) Measurement of Gibbs energy formation of oxides:

Solid electrolytes are widely used for measuring thermo chemical properties at elevated temperatures. Solid electrolytes used for these applications should predominantly conduct by ions and the ionic transference number should be greater than 0.99, i.e. the measurements should be carried out within the electrolytic domain boundaries of the solid electrolyte. It is also to be noted that different solid electrolytes possess different electrolytic domain boundaries. Galvanic cells can be constructed using solid oxide electrolytes for emf measurements. Any such cell can be represented as



where  $\mu'_{\text{O}_2}$  and  $\mu''_{\text{O}_2}$  are the chemical potentials of oxygen at the two electrodes. The emf of the cell is given by:

$$E = \frac{1}{nF} \int_{\mu'_{\text{O}_2}}^{\mu''_{\text{O}_2}} t_{\text{ion}} d\mu_{\text{O}_2} \quad (1.62)$$

where  $n$  is the number of charges involved in the transport of one oxygen molecule,  $F$  is the Faraday constant and  $t_{\text{ion}}$  is the ionic transference number of the solid electrolyte.

When the measurements are carried out in the electrolyte boundary,  $t_{\text{ion}} \sim 1$  and therefore:

$$E = \frac{1}{4F} \int_{\mu_{O_2}}^{\mu_{O_2}''} t_{ion} d\mu_{O_2} = \frac{RT}{4F} \ln \frac{p_{O_2}''}{p_{O_2}} \quad (1.63)$$

Thus, the measurement of emf at different partial pressures, one can calculate the Gibbs energy formation of the compound in different phases (with differing oxygen equilibrium) of the oxide electrolyte used. Similarly, the Gibbs energy formation of the halides can be calculated using a halide ion conducting electrolyte in the potentiometric cell given in equation (1.61).

(b) Determination of the chemical potential of a component in alloy

Determination of chemical potential of a component  $i$  in an alloy phase ( $\alpha$ ),  $\mu_i^\alpha$ , is a sufficient tool for characterising an alloy system. Even though no single experiment would provide reliable results, a comparison of results obtained from various techniques like Galvanic cell method, calorimetry, etc. can be used to reach a conclusion for the determination of the chemical potential of the component in the alloy. The use of Galvanic cell method which applies the principle of emf based on the solid electrolyte, has added valuable information to high temperature calculations. The representation of a typical cell configuration used for the determination of activity of the component of an alloy system is given as:



where  $A$  is a metal of the alloy  $[A]_B$  and  $AO$  is the oxide of 'A' in equilibrium with metal  $A$  in the conditions of measurements. The electrode reactions are:



Assuming the oxide  $AO$  as a stoichiometric oxide under chemical equilibrium with the electrodes, the emf of the cell can be given as:

$$E = -\frac{RT}{nF} \ln a_A \quad (1.67)$$

Thus, the activity of the component A in the alloy can be calculated by measuring the emf of a typical cell represented in equation (1.64).

### (c) Kinetic studies based on potentiometric cells

As a matter of completion of the above applications of solid electrolytes towards determination of thermodynamic properties, the electrochemical cell can be used to understand the kinetics of the electrode reaction. The kinetic studies using solid electrolyte involves the determination of transport phenomena and polarisation studies. Generally, the current or voltage across the electrode-electrolyte interface is measured with respect to time. Solid electrolyte based kinetic studies can also determine diffusion coefficient of oxygen in liquid or solid metal and the materials can be used to understand the chemical diffusivity in non-stoichiometric compounds and alloys. The kinetic studies using solid electrolyte cells reveal the kinetics of the phase boundary and diffusion controlled reactions at the electrode-electrolyte interfaces.

### 1.13 STRUCTURE OF AgI

Solid electrolytes which conduct at low temperature have activation energy around 0.1-0.2 eV. But, for solid electrolytes which work at high temperature, for migration of ion in a lattice, the activation energy required will be greater than 1 eV. In contrast, in solid electrolytes, the activation energy may be much lower, as low as 0.03 eV in AgI, 0.45 eV in  $\beta$ -alumina and  $\sim 0.9$  eV in yttria stabilised zirconia [58]. A few of the solid electrolytes like NASICON,  $\text{Pb-}\beta\text{-Al}_2\text{O}_3$ , etc. show temperature dependent variation in activation energy. The migration of ions in these crystals can happen mainly by (a) vacancy diffusion and (b) interstitial diffusion. The available vacant sites in solid electrolyte are more than the number of ions migrating. Such vacant passages for the movement of ion are generally created, when the polyhedral are face-centred [59]. The corner, edge and

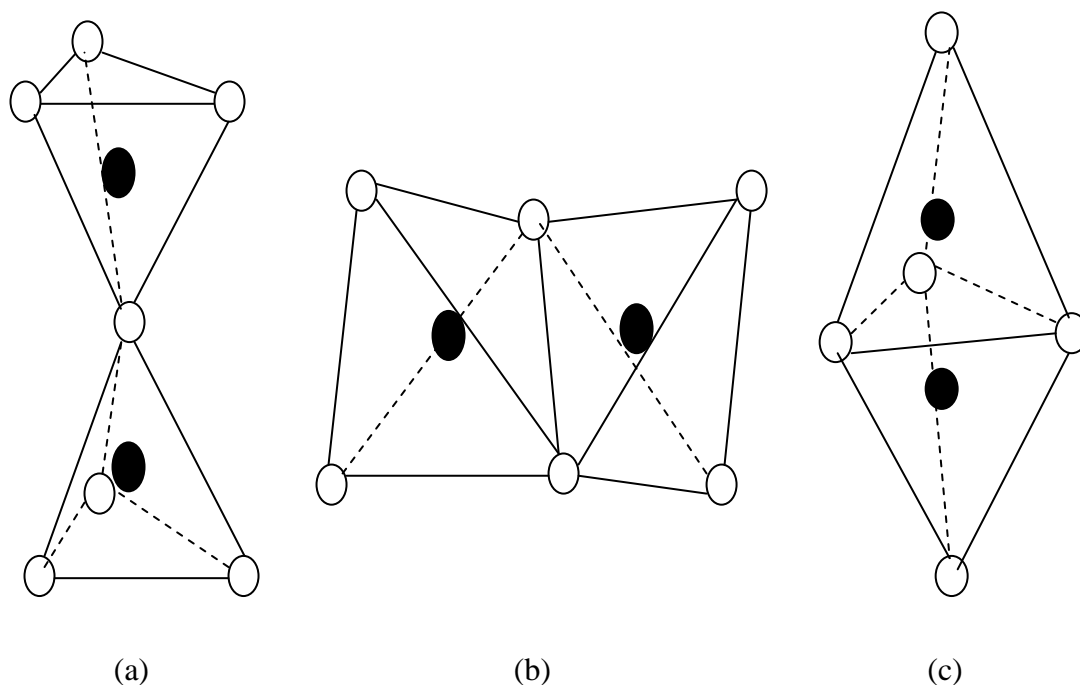


**Fig. 1.8 Tetrahedra with (a) corner shared (b) edge shared and (c) face shared atoms [60] where the black balls represent the cations and white balls represent the anions**

face centred tetrahedral are shown in Fig. 1.8. Face-centred polyhedra are generally formed by anions having large ionic radii [60]. The sharing of faces and edges of the polyhedra are energy intensive and this probability of sharing decreases with increasing size of the central cation. This is due to the increase in the proximity of the cations with polyhedra shared by faces or edges. Silver ion conducting solid electrolytes like  $\text{RbAg}_4\text{I}_5$ , potassium ion substituted  $\text{RbAg}_4\text{I}_5$  or  $\alpha\text{-AgI}$  contains face sharing tetrahedra/octahedra which provides the structure with channels for cation to migrate. This is the basis of high ionic conductivity in compounds with large ionic radii having iodide ion (ionic radii of I being  $2.2 \text{ \AA}$  [61]). Among the solid electrolytes, limited literature is available in the use of silver ion conducting solid electrolyte namely, AgI as a material for sensing application. Structural details of AgI and the influence of anionic substitution are discussed below. AgI exists in three allotropic modifications in the temperature range of 298-673 K. The  $\beta$  and  $\gamma$  phases are reported as poorly-conducting phases [62] whereas the  $\alpha$ -phase is the highly conducting phase above the temperature of  $\sim 420 \text{ K}$  until it melts at  $\sim 831 \text{ K}$  [63].

The crystal structure of the three allotropes at normal pressure is shown in Fig. 1.9.  $\gamma$ -phase exists along with  $\beta$ -phase at room temperature.  $\gamma$ -phase exhibits BCC structure with anion close packing whereas  $\beta$ -phase exhibits hexagonal structure at room temperature. Above the  $\beta$  to  $\alpha$  transition temperature, the wurtzite structure of  $\alpha$ -AgI is stable until AgI melts.

The structure of  $\alpha$ -AgI is highly conducting phase above  $\sim 420$  K compared to  $\beta$  and  $\gamma$  polymorphs of AgI. This conductivity arises due to the 42 interstitial voids which are present in the wurtzite structure of  $\alpha$ -AgI. The figure representing the void networks of  $\alpha$ -AgI is shown in Fig. 1.10.

There are 6 octahedral, 12 tetrahedral and 24 trigonal sites in a unit cell for  $\alpha$ -AgI. The movement of two  $\text{Ag}^+$  ions in all these interstitial voids gives high conductivity for AgI in  $\alpha$ -phase. The reported bulk conductivity for  $\alpha$ -phase of AgI is around  $0.4$  to  $0.6 \text{ Scm}^{-1}$  [66, 67]

#### **1.14 SUBSTITUTION OF CATIONIC OR ANIONIC SPECIES IN AgI**

With an objective to bring better ionic conductivity at lower temperatures, AgI preparation was adopted with different methodologies. The reduction in the particle size of AgI [63, 68], superionic transitions under pressurised conditions [67] and substituting the cation or anion with different sizes of ions [66, 67, and 70] were the different procedures adopted in literature. An admixture of AgI and  $\text{Ag}_2\text{CsI}_3$  was also reported to show better conductivity compared to AgI [71]. The significance of adding a cation like  $\text{Cu}^+$  (ionic radius:  $0.77 \text{ \AA}$ ) in AgI [67, 70] was with the intention of substituting a second mobile ion ( $\text{Cu}^+$  ion) in AgI. Both  $\text{Cu}^+$  and  $\text{Ag}^+$  are having good ionic conduction in solids [72]. Introduction of larger ions like  $\text{Cs}^+$  (ionic radius:  $1.67 \text{ \AA}$  [61]) will cause the lattice loosening [73] due to the incorporation of larger  $\text{Cs}^+$  ion compared to  $\text{Ag}^+$  ion (ionic radius:  $1.15 \text{ \AA}$ ) [67 and 71].

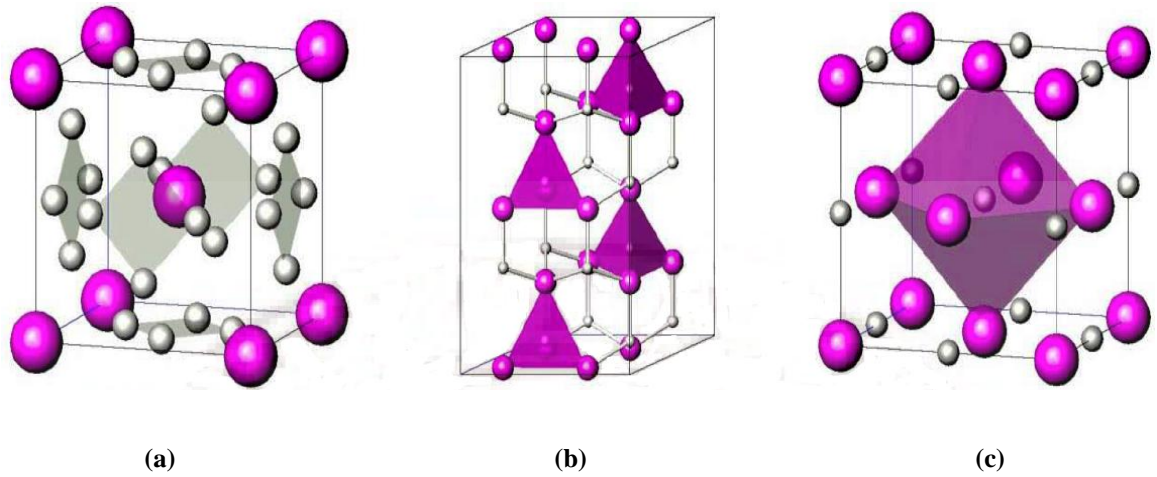


Fig. 1.9 Crystal structure of (a)  $\gamma$ -AgI (b)  $\beta$ -AgI and (c)  $\alpha$ -AgI [64]

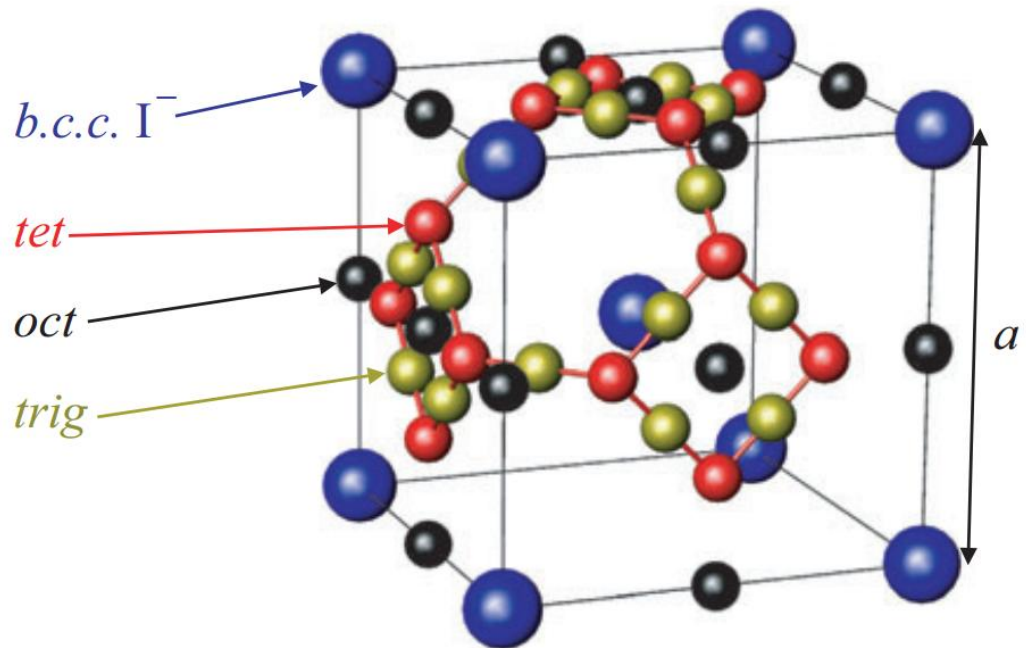


Fig. 1.10 Crystal structure of  $\alpha$ -AgI representing the 42 interstitial voids. tet represents tetragonal, oct represent octahedral void and trig represents trigonal void [65]

Thus, by perturbing the crystal structure by substitution with different size of cations, results in lattice loosening. Further, it was reported that such approaches increase the bulk conductivity and reduce the phase transition temperature of  $\beta$  to  $\alpha$  phase in AgI considerably. The reported literature shows a reduction down to 397 K in the case of Cd

substituted AgI [74]. Cs substituted AgI reported by Bazan and Pettigrosso [66] also established the solubility limit of CsI in AgI ~4 mol%.

The substitutions of anions in various crystals and the study of their solubility limit in various silver ion based compounds are reported in literature [73,76]. According to Hume-Rothery rules [77], for the formation of solid solution, the ionic radii differences must be below ~15 %. The rule also emphasises the need for similar crystal structure and electronegativity of the mixing ions. The crystal structure of AgCl is cubic structure [78]. The solid solution formation between AgCl and AgI will be limited as the crystal structure is different for both AgCl and AgI and there is ~17 % difference between the ionic radii of Cl<sup>-</sup> and I<sup>-</sup> ( $r_{\text{Cl}^-}$ :1.81Å and  $r_{\text{I}^-}$ :2.2Å [61]).

The need for Cl<sup>-</sup> substitution in AgI was steered by the reduction in  $\beta$  to  $\alpha$  phase transition temperature in AgI [79]. Thus, it is possible to bring the conducting phases to lower temperatures of operation. A sensor which works at 420 K using AgI may work at still lower temperatures when Cl<sup>-</sup> added. The  $\alpha$ -phase is stable at lower temperatures in anion substituted AgI compared to that of pure AgI. Also, from the basics of potentiometric cells, to selectively detect the gas of interest, we need to incorporate the analyte ion itself in the matrix for Type I and II ionic conductors mentioned in section 1.11.

### **1.15 SCOPE OF THE THESIS**

From the previous sections describing the halogens pertaining to nuclear industry, the need for iodine and chlorine sensor during an accidental leak of the fission products into the coolant streams are already emphasised. Iodine can reach the reactor containment building during the breach of the structural materials both in the thermal as well as the fast reactors. Radioiodine can also get released in the chopping areas of reprocessing sector in a closed fuel cycle reactor system. Thus, monitoring of iodine is essential as an

alternative safety measure for healthy operation of reactor and also the reprocessing facility.

Chlorine on the other hand plays a major part in the pyroprocessing of nuclear fuels. An unforeseen leak of chlorine, during the breach of the electrochemical cell containment, into the glove box containing the cell can happen during an accidental situation. Similar to monitoring iodine, chlorine needs to be monitored in the operating area of pyroprocessing.

Solid state sensors based on AgI shows good ionic conduction above 423 K due to its open crystal structure. Such compounds with high ionicity are ideal to be used as electrolyte in a potentiometric sensor. The affinity of  $\text{Ag}^+$  ion in AgI to maintain equilibrium with iodine and chlorine is the driving force for selecting AgI as the base matrix for sensing material. The need for substituting I<sup>-</sup> with Cl<sup>-</sup> was to bring down the  $\beta$  to  $\alpha$  transition temperature. Thus, it would be possible to operate the sensor material containing appropriate AgCl content, at much lower temperature compared to pure AgI. Also, the presence of Cl<sup>-</sup> in AgI will increase the selectivity of the electrochemical sensor towards chlorine gas.

The solubility limit of AgCl in AgI prepared through a novel solution route was established by using different physicochemical techniques. The gradation in other physical properties like  $\beta$  to  $\alpha$  transition temperature, ionic transference number and bulk conductivity observed for  $\text{AgI}_{1-x}\text{Cl}_x$  was compared with solubility limit studies.

Sensor studies were carried out on  $\text{AgI}_{1-x}\text{Cl}_x$  towards iodine and chlorine. The peculiar behaviour of AgI towards chlorine gas was studied by an in-house fabricated three electrode configuration using dielectric spectroscopic technique. The results were then corroborated with the XPS studies to confirm the findings from the capacitance measurements. The demonstration of the miniaturised chlorine sensor was carried out to

study the sensing characteristics of  $\text{AgI}_{0.95}\text{Cl}_{0.05}$  towards trace levels of chlorine. The advantage of miniaturisation and the improvement in detecting lower concentration are further discussed in different chapters.

## 1.16 REFERENCES

1. T. Kaiho, 2015, Iodine chemistry and application, 1<sup>st</sup> ed., John Wiley and Sons, Inc., New Jersey, 656 pp
2. R. Fuge and C.C. Johnson, 1986, The geochemistry of iodine - a review, Environment Geochemistry Health, , 8 (2), 31-54
3. J.E. Moran, 2002, Sources of iodine and iodine 129 in rivers, Water Resources Research, 38, No.8, 1149, 24-1 to 24-10
4. Data research analyst, Chlorine role in day to day life, World of chemicals.com. [www.worldofchemicals.com/435/chemistry-articles/chlorine-role-in-day-to-day-life.html](http://www.worldofchemicals.com/435/chemistry-articles/chlorine-role-in-day-to-day-life.html), [Accessed on 08<sup>th</sup> June 2017]
5. A.J. Elias, World production of halogens, 2016, Elias Lecture, IIT Delhi, India, 26 pp., [web.iitd.ac.in/~elias/links/Elias\\_lecture\\_of\\_chlorine\\_2016\\_nov.pdf](http://web.iitd.ac.in/~elias/links/Elias_lecture_of_chlorine_2016_nov.pdf), [Accessed on 02<sup>nd</sup> June 2017]
6. The essential chemical industry, Iodine, Centre for industry education collaboration, Department of Chemistry, University of York, United Kingdom. [www.Essetialchemicalindustry.org/chemicals/iodine.html](http://www.Essetialchemicalindustry.org/chemicals/iodine.html), [Accessed on 02<sup>nd</sup> June 2017]
7. Nuclear Energy Today, 2012, 2<sup>nd</sup> ed., OECD, Nuclear Development, Nuclear Energy Agency, 123 pp. <https://www.oecd-nea.org/pub/nuclearenergytoday/6885-nuclear-energy-today.pdf>, [Accessed on 02<sup>nd</sup> June 2017]
8. A.V. Nero Jr., 1979, Nuclear Reactors, University of California Press, California, 281 pp

9. K.V. Suresh Kumar, A. Babu, B. Anadapadmanaban and G. Sreenivasan, 2011, Twenty five years of operating experience with fast breeder test reactor, Energy Procedia 7, 323-332
10. Nuclear data for safeguards, Updated on 2016, Cumulative fission yields, International Atomic Energy Agency, [www-nds.iaea.org](http://www-nds.iaea.org), [Accessed on 03<sup>rd</sup> March 2017]
11. A.W. Castleman Jr., 1970, A review of current status of research on the physical and chemical aspects of liquid metal cooled fast breeder reactor safety I. Fission product behaviour in sodium, Brookhaven National Laboratory, 43 pp
12. Spent fuel reprocessing options, 2008, IAEA-TECDOC-1587, International Atomic Energy Agency, Nuclear Fuel Cycle and Materials Section , Austria, 151 pp. [http://www-pub.iaea.org/MTCD/publications/PDF/te\\_1587\\_web.pdf](http://www-pub.iaea.org/MTCD/publications/PDF/te_1587_web.pdf), [Accessed on 10<sup>th</sup> June 2017]
13. P. Souček, R. Malmbeck, C. Nourry and J.P. Glatz, 2010, Pyrochemical reprocessing of spent fuel by electrochemical techniques using solid aluminium cathodes, Asian Nuclear Prospects, Energy Procedia 7, 396-404
14. S. Glasstone and A. Sensonske, 1994, Nuclear Reactor Engineering, Reactor system engineering, Vol.2, 4<sup>th</sup> ed., Springer Science with Business Media, Singapore, 839 pp
15. J.J. Laidler, J.E. Battles, W.E. Miller, J.P. Ackerman and E.L. Carles, 1996, Development of pyroprocessing technology, Progress in Nuclear Engineering, 31, No.1/2, 131-140
16. D.A. Mc Quarrie, P.A. Rock and E.B. Gallogly, 2011, The Halogens, General Chemistry, 4<sup>th</sup> ed., University Science Books, CA, 1149 pp

17. J. Robins and A.B. Schneider, 2000, Thyroid cancer following exposure to radioactive iodine, *Reviews in Endocrine and Metabolic Disorder*, 1(3), 197-203
18. C.H. Keamy, 1980, Nuclear war survival skills, NWS Research Bureau, Oregon, 221 pp
19. Managing hazardous materials incidents: Medical management guideline for acute chemical exposure, 2001, Vol. III, US department of health and human services, Public Health Services, Agency for toxic substances and disease registry, Atlanta, 295 pp. [https://www.atsdr.cdc.gov/mhmi/mhmi\\_v1\\_2\\_3.pdf](https://www.atsdr.cdc.gov/mhmi/mhmi_v1_2_3.pdf), [Accessed on 04<sup>th</sup> June 2017]
20. A.M. Leung and L.E. Braverman, 2014, Consequence of excess iodine, *Nature Reviews Endocrinology*, 10, 136-142
21. J.F. Coindet, 1821, Nouvelles recherches sur les effects de l'iode, et sur les précautions à suivre dans le traitement de goitre par le nouveau remède [French], *Annales de Chimie et de Physique*, 16, 252-256
22. P. Pramyothin, A.M. Leung, E.N. Pearce, A.O. Malabanan, L.E. Braverman, Clinical problem solving, A hidden solution, 2011, *New England Journal of Medicine*, 365, 2123-2127
23. Tolerable upper intake levels for vitamins and minerals, Scientific Committee on Food, Scientific panel on allergies, European Food Safety Authority, 482 pp. [http://www.efsa.europa.eu/sites/default/files/efsa\\_rep/blobserver\\_assets/ndatolera\\_bleuil.pdf](http://www.efsa.europa.eu/sites/default/files/efsa_rep/blobserver_assets/ndatolera_bleuil.pdf), [Accessed on 15<sup>th</sup> June 2017]
24. Managing hazardous materials incidents: Medical management guideline for acute chemical exposure, 2001, Vol. III, US department of health and human services, Public Health Services, Agency for toxic substances and disease registry, Atlanta,

- 295 pp, [https://www.atsdr.cdc.gov/mhmi/mhmi\\_v1\\_2\\_3.pdf](https://www.atsdr.cdc.gov/mhmi/mhmi_v1_2_3.pdf), [Accessed on 15<sup>th</sup> June 2017]
25. R.D. Harbison, M.M. Bourgeois, G.T. Johnson, 2015, Hamilton and Hardy's industrial toxicology, 6<sup>th</sup> ed., John Wiley and Sons Inc, New Jersey, 1376 pp
  26. C.W. White and J.G. Martin, 2010, Chlorine gas inhalation: Human Clinical evidence of toxicity and experience in animal models, Proceedings of American thoracic society, 7, 257-263
  27. W.M. Haynes, 2016, CRC Handbook of Chemistry and Physics, 97<sup>th</sup> ed., Taylor and Francis Group, UK, 2652 pp
  28. P. Grundler, 2007, Chemical Sensors, 1<sup>st</sup> ed., An introduction to scientists and engineers, Springer-Verlag Berlin Heidelberg, 274 pp
  29. F.N. Dultsev, 2008, Polymeric film based on long chain acetylenes as sensors for iodine vapour, Sensors and Actuators B, 129, 171-175
  30. C.X. Jiao, Q. Shen, S.Y. Huan, G.L. Shen, R.Q. Yu, 2005, Conjugated carbazole dimer as fluorescence carrier for preparation of iodine-sensitive chemical sensor, Analytica Chimica Acta, 528, 229-234
  31. M.E. Sola, H.G. Rotstein and J.C. Bazán, 2002, The Ag(s)/AgI(s)/graphite solid cell as iodine sensor: speed of response and use of Cs doped AgI as electrolyte, Journal of Solid State Electrochemistry, 6 (4), 279-283
  32. D. James and T.P. Rao, 2012, Potentiometric sensing of iodide using polymeric membranes of microwave stabilised  $\beta$ -AgI, Electrochimica Acta, 66, 340-346
  33. Z.H. Ibupoto, K. Khun and M. Willander, 2013, A selective iodide ion sensor electrode based on functionalised ZnO nanotubes, Sensors, 13, 1984-1997

34. R. Saini, A. Majan, R.K. Bedi, D.K. Aswal, A.K. Debnath, 2014, Room temperature ppb level Cl<sub>2</sub> detection and sensing mechanism of highly selective and sensitive phthalocyanine nanowires, *Sensors and Actuators B*, 203, 17–24
35. A. Chaparadza and S.B Ranannavare, 2008, Room temperature Cl<sub>2</sub> sensing using thick nanoporous films of Sb-doped SnO<sub>2</sub>, *Nanotechnology*, 19, 245501, 1-8
36. D.R. Patil and L.A. Patil, 2007, Room temperature chlorine gas sensing using surface modified ZnO thick film resistor, *Sensors and Actuators B*, 123, 546-55
37. D.H. Dawson and D.E. Williams, 1996, Gas sensitive resistors: surface interaction of chlorine with semiconducting oxides, *Journal of. Material Chemistry*, 6, 409-14
38. X.F. Chu, 2003, High sensitivity chlorine gas sensors using CdIn<sub>2</sub>O<sub>4</sub> thick film prepared by co-precipitation method, *Materials Research Bulletin*, 38, 1705-1711
39. A. Galdikas, Z. Martunas and A. Setkus, 1992, SnInO-based chlorine gas sensor, *Sensors and Actuators B*, 7, 633-636
40. X.F. Chu and M.C. Zhimming, 2004, High sensitivity chlorine gas sensors using CdSnO<sub>3</sub> thick film prepared by co-precipitation method, *Sensors and Actuators B*, 98, 215-217
41. M.D. Mahanubhav and L.A. Patil, 2007, Studies on gas sensing performance of CuO-modified CdIn<sub>2</sub>O<sub>4</sub> thick film resistors, *Sensors and Actuators B*, 128, 186-192
42. J. Tamaki, J. Niimi, S. Ogura and S. Konishi, 2006, Effect of micro-gap electrode on sensing properties to dilute chlorine gas of indium oxide thin film microsensors, *Sensors and Actuators B*, 117, 353-358
43. T. Miyata, T. Hikosaka and T. Minami, 2000, High selectivity chlorine gas sensors using multicomponent transparent conducting oxide thin films, *Sensors and Actuators B*, 69, 16-21

44. T. Miyata and T. Minami, 2005, Chlorine gas sensors with high sensitivity using Mg-phthalocyanin thin films, *Applied Surface Science*, 244, 563-567
45. S. Jain, A.B. Samui, M. Patri, V.R. Hande and S.V. Bhorasker, 2005, FEP/polyaniline based multilayered chlorine sensor, *Sensors and Actuators B*, 106, 609-613
46. T. Miyata, S. Kawaguchi, M. Ishii and T. Minami, 2003, High sensitivity chlorine gas sensors using Cu-phthalocyanine thin films, *Thin Solid films*, 425, 255-259,
47. F. Bender, C. Kim, T. Mlsna and J.F. Vetelino, 2001, Characterisation of a WO<sub>3</sub> thin film chlorine sensors, *Sensors and Actuators B*, 77, 281-286
48. J. Tamaki, C. Naruo, Y. Yamamoto and M. Matsuoka, 2002, Sensing properties to dilute chlorine gas of indium oxide based thin film sensors prepared by electron beam, *Sensors and Actuators B*, 83, 190-194
49. C.V.G. Reddy, S.V. Manorama and V.J. Rao, 1999, *Sensors and Actuators B*, Semiconducting gas sensors for chlorine sensor based on inverse spinel structure 55, 90-95
50. G. Hotzel and W. Weppner, 1987, Potentiometric gas sensors based on fast solid electrolyte, *Sensors and Actuators*, 12, 449-453
51. W. Weppner, 1987, Solid-state electrochemical gas sensors, *Sensors and Actuators*, 12, 107-119
52. A. Menne and W. Weppner, 1990, Selectivity, response time and chemical aspects of gas sensitive AgCl layers for gas sensors, *Solid State Ionics* 40/41, 468-471
53. Y. Ding, J. Ling, J. Cai, S. Wang, X. Li, M. Yang, L. Zha and J. Yan, 2016, A carbon dot based hybrid fluorescent sensor for detecting free chlorine in water medium, *Analytical Methods*, 8, 1157-1161

54. G.F. Knoll, 2010, Radiation detection and measurements, 4<sup>th</sup> ed., John Wiley and Sons, Inc. New Jersey, 819 pp
55. Isotopes and radiation technology, 2006, Isotopes Vol. 3-4, Atomic Energy Commission
56. Y. Miyake, H. Matsuzaki, T. Fujiwara, T. Saito, T. Yamagata, M. Honda, Y. Maramatsu, 2012, Isotopic ratio of radioactive iodine (<sup>129</sup>I/<sup>131</sup>I) released from Fukushima Daiichi NPP accident, *Geochemical Journal*, 46, 327-333
57. E.C. Subbarao (ed.), 1980, Solid electrolytes and their application, New York, Plenum Press, 298 pp
58. P.G. Bruce (ed.), 1995, Solid state electrochemistry, Cambridge University Press, Scotland, 333 pp
59. S. Geller (ed.), 1977, Solid electrolytes, Springer-Verlag Berlin Heidelberg, New York, 223 pp
60. T. Chen, 2015, Data analysis to understand coordination and topological environments in oxides, Ph.D. Dissertation, Massachusetts Institute of Technology, UK, 52 pp
61. R.D. Shannon, 1976, Revised Effective Ionic Radii and Systematic Studies of interatomic distances in halides and chalcogenides, *Acta Crystallographica Section A*, A32, 751-767
62. L.B. Pankratz, 1984, Thermodynamic properties of halides, Bulletin 874, US department of the interior, Bureau of mines, 830 pp
63. R. Makiura, T. Yonemura, T. Yamada, M. Yamauchi, R. Ikeda, H. Kitagawa and M. Takata, 2009, Size controlled stabilisation of the superionic phase at room temperature in polymer coated AgI nanoparticle, *Nature Materials*, 8, 476-480

64. A compilation of Ph.D. thesis, Ph.D. Dissertation, 23 pp.  
shodhganga.inflibnet.ac.in/bitstream/10603/77260/7/07\_chapter%201.pdf,  
[Accessed on 2<sup>nd</sup> May 2017]
65. S. Hull, 2001, Superionics: Crystal structure and conduction process, Reports in Progress in Physics, 67, 1233-1314
66. J.C. Bazan and R.S. Pettigrosso, 1994, A DSC and conductivity study of the influence of caesium ion on the beta-alpha transition in silver iodide, Solid state ionic materials, 69, 205-210
67. J.C. Bazan, J.A. Schimdt and R.S.P. De Miraglia, 1982, Influence of Cs<sup>+</sup> ion on the co-ionic conductivity in the AgI-CuI solid system, Solid State Ionics, 6, 171-173
68. G.G. Gospodinov, M. Hanaya, 2004, XRD and thermal studies of AgI confined in nanosize pores by forming porous silica AgI composites, Journal of Thermal Analysis, 26, 529-536
69. D.A. Keen and S. Hull, 1991, Powder neutron diffraction study of the pressure induced phase transition within silver iodide, Journal of Physics of Condensed Matter, 5, 23-32
70. J.C. Bazan and J.A. Schmidt, 1976, A Cu(I) ion conductor obtained by replacement of Ag(I) in  $\alpha$ -AgI, Journal of Applied Electrochemistry, 6, 411-415
71. L.A. Rodríguez, J. Zapata, R.A. Vargas, D. Peña Lara and J. E. Diosa, 2016, Superionic behaviour in the  $x\text{AgI}(1-x)\text{CsAg}_2\text{I}_3$  polycrystalline system, Journal of Physics and Chemistry of Solids, 93, 126-130
72. R.D. Armstrong, R.S. Bulmer, and T. Dickinson, 1973, Some factors responsible for high ionic conductivity in simple solid compounds, Journal of Solid State Chemistry 8 (3), 219-228

73. K. Shahi and J. B. Wagner Jr., 1980, Phase transition and the  $\text{Ag}^+$  ion diffusion in  $\text{AgI}$ : Effect of homovalent  $\text{Br}^-$ -ion substitution, *Physical Review B*, 23, 6417-6421
74. M. Hassan, 2007, A superionic conducting phase in Cd substituted  $\text{CsAg}_2\text{I}_3$ , *Solid State Communication*, 144, 293-295
75. M.E. Kettai, J.P. Malugani, R. Mercier and M. Tachez, 1986, Phase transitions and conductivity in superionic  $\text{Ag}_3\text{SI}_{1-x}\text{Br}_x$  solid solution, *Solid State Ionics*, 20, 87-92
76. R.B. Beeken, T.J. Wright and T Sakuma, 1999, Effect of chloride substitution in the fast ion conductor  $\text{Ag}_3\text{SBr}$ , *Journal of Applied Physics* 85, 7635-7638
77. A.R. West, 2007, *Solid state chemistry and its applications*, John Wiley and Sons Pvt. Ltd., New Jersey, 720 pp
78. A.B. Kunz, 1982, Electronic structure of  $\text{AgF}$ ,  $\text{AgCl}$  and  $\text{AgBr}$ , *Physical Review B* 26, 2070-2075
79. S. Ihara, Y. Warita and K. Suzuki, 1984, Ionic conductivity in  $\text{AgI}_{1-x}\text{Cl}_x$ , *Physica Status Solidi A*, 86, 729-734

## CHAPTER 2

### EXPERIMENTAL METHODS PRINCIPLES AND APPLICATIONS

#### 2.1 INTRODUCTION

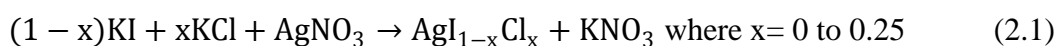
Methodologies and detection limits play a key role in analysing the compositions for different applications. This chapter briefs about the preparation of the samples, methodologies used for their characterisation, calibration standards employed for normalising the measurements and also the details of the experimental facilities used for these characterisation.

#### 2.2 EXPERIMENTAL

The preparation, characterisation and gas sensing behaviour of  $\text{AgI}_{1-x}\text{Cl}_x$  are presented in the thesis. Employing the precipitation and co-precipitation routes for the preparation of the samples, discussion on different parameters like temperature, concentration, etc. and procedures adopted, related to the study of the solubility limit of  $\text{AgCl}$  in  $\text{AgI}$ , their sensing characteristics and mechanism of sensing are dealt with in this chapter. The details of the fabrication of different electrochemical cells for various measurements are also described.

#### 2.3 PREPARATION OF $\text{AgI}_{1-x}\text{Cl}_x$

The powders of  $\text{AgI}$  and  $\text{AgI}_{1-x}\text{Cl}_x$  were synthesised by the precipitation and co-precipitation methods respectively, using solutions of  $\text{KI}$ ,  $\text{KCl}$  and  $\text{AgNO}_3$  (99.9 % pure, Alfa-Aesar make). For these preparations, stoichiometric quantities of silver nitrate, potassium iodide and potassium chloride solutions were taken. The weights of the compounds taken for making the respective solutions were calculated using the following equation:



To prepare AgI, a solution of silver nitrate was added to potassium iodide solution slowly with continuous stirring. After the completion of addition of silver nitrate solution into potassium iodide, stirring was continued for next 2 h. Once the digestion of the precipitate was completed after 24 h, in both the processes, the product was filtered and kept for drying at 373 K for two days. After drying the precipitate, the powder was ground and was calcined to 473 K for 48 h. The final product was subjected to different characterisation methods to confirm the formation of AgI. Precautions were taken to avoid the interference from light during the preparation and the reactions were carried out in dark.

AgI<sub>1-x</sub>Cl<sub>x</sub> powders were pressed into pellets with diameter of ~8-10 mm and thickness of around 1.7 mm. The pellets were made under a pressure of ~20000 kPa. The geometrical densities for the pellets were around ~98 % theoretical density. High percentage theoretical densities are good for electrical conductivity and sensor studies. A list of compositions and their geometries used for different characterisation studies are given in Table 2.1.

**Table 2.1 Composition and geometry of the samples studied under each characterisation technique**

| Sample                                    | XRD  | AAS            | DSC                            | SEM                           | Transport measurements  | Electrical Conductivity            |                 | Sensor Studies                    | XPS                  |
|---|--|----------------|--------------------------------|-------------------------------|-------------------------|------------------------------------|-----------------|-----------------------------------|----------------------|
|   |  |                |                                |                               |                         | Two electrode                      | Three electrode |                                   |                      |
| AgI <sub>1-x</sub> Cl <sub>x</sub><br>(x) | 0,<br>0.025,<br>0.05,<br>0.06,<br>0.1,<br>0.25 | 0.025,<br>0.05 | 0,<br>0.025,0.05,<br>0.06, 0.1 | 0,<br>0.025,<br>0.05,<br>0.06 | 0, 0.025, 0.05,<br>0.06 | 0,<br>0.025,<br>0.05,<br>0.06, 0.1 | 0               | 0,<br>0.025,<br>0.05,<br>0.06,0.1 | 0,<br>0.025,<br>0.05 |
| <b>Geometry of material</b>               | Powder   | Powder         | Powder                         | Pellet                        | Pellet                  | Pellet                             |                 | Pellet                            | Pellet and powder    |

## 2.4 X-RAY DIFFRACTION

X-ray diffraction is based on constructive interference of monochromatic X-rays and a crystalline sample. These X-rays are generated by a cathode ray tube, filtered to produce monochromatic radiation, collimated to concentrate, and directed towards the sample. The interaction of the incident rays with the sample produces constructive interference

(and a diffracted ray) when conditions satisfy Bragg's Law ( $n\lambda = 2d \sin \theta$ ). This law relates the wavelength of electromagnetic radiation to the diffraction angle and the lattice spacing in a crystalline sample. The diffracted X-rays from the sample are then detected, processed and counted. By scanning the sample through a range of  $2\theta$ , all possible directions for diffraction of the lattice should be attained due to the random orientation of the powdered material. Conversion of the diffracted peaks to d-spacing allows identification of the crystal structure of the sample because each sample has a set of unique d-spacing. Typically, this is achieved by comparison of d-spacing with standard reference patterns. A schematic of X-ray diffraction phenomena is shown in Fig. 2.1.

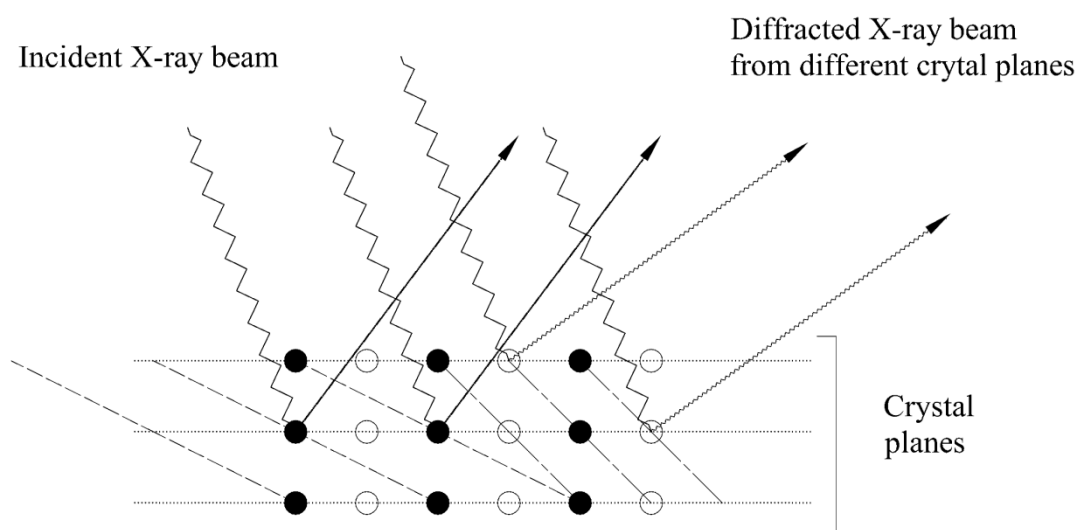


**Fig. 2.1 Schematic representation of Bragg's law [1]**

The quantitative calculation of the lattice loosening [2] of the crystal structure of AgI with the addition of AgCl from the unit cell volume [3] was calculated and the results of the calculation are presented in the chapter 3. The crystallite sizes of  $\text{AgI}_{1-x}\text{Cl}_x$  were calculated using HOCT software (in-house written software by Dr. S. Senbhagaraman, Materials Research Centre, IISC, Bangalore which uses linear least square fit for computing lattice parameter and crystallite size for hexagonal, orthorhombic, cubic and tetragonal system). Samples of  $\text{AgI}_{1-x}\text{Cl}_x$  were studied using XRD facility (Model No. D500, M/s Siemens, Germany).

## **2.5 SCANNING ELECTRON MICROSCOPY (SEM) [4,5]**

Secondary electrons and backscattered electrons are commonly used for imaging samples: secondary electrons are the most valuable for showing morphology and topography of samples and backscattered electrons, illustrating contrasts in composition in multiphase samples (i.e. for rapid phase discrimination). Energy Dispersive X-ray Analysis (EDAX) is one of the salient features of SEM and can be used to determine the elemental composition of the surface of the samples. By measuring the energy of the characteristic X-rays of the elements, information about the elemental composition of the sample surface can be obtained. Morphological characterisations of the samples were carried out using scanning electron microscopy Model XL30, M/s Philips, Netherlands. The images were recorded with different magnifications. Quantitative estimation of  $\text{AgI}_{1-x}\text{Cl}_x$  using EDAX was also carried out and is presented in chapter 3. The correlation between the solubility limit and precipitation of the impurity peak in EDX and changes in morphology for  $\text{AgI}_{1-x}\text{Cl}_x$  will be described in chapter 3.

## **2.6 DIFFERENTIAL SCANNING CALORIMETRY (DSC)**

Differential Scanning Calorimetry (DSC) is a thermo-analytical technique in which the difference in the amount of heat required to increase the temperature of a sample and reference are measured as a function of temperature [6, 7]. Both the sample and reference are maintained at nearly the same temperature throughout the experiment. Generally, the temperature program for a DSC analysis is designed such that the sample holder temperature increases linearly as a function of time. The reference sample should have a well-defined heat capacity over the range of temperatures to be scanned. The main application of DSC is in studying phase transitions, such as melting, glass transitions, or exothermic decompositions. These transitions involve energy changes or heat capacity changes that can be detected by DSC with great sensitivity.

Differential scanning calorimetric experiments were carried out using a calorimeter, Model: HPDSC827, supplied by M/s Metler Toledo, Switzerland. A known quantity of the nominal composition of  $\text{AgI}_{1-x}\text{Cl}_x$  (~50 mg) was sealed inside a thin aluminium crucible on the sample side. An empty aluminium crucible was employed as reference. A heating rate of ~ 5 K/min was used for the present study.

## 2.7 ATOMIC ABSORPTION SPECTROMETRY (AAS)

A given population of free atom exists at various electronic levels [8]. The distribution of atoms in the energy levels is given by the Boltzmann distribution equation given below:

$$\frac{N_2 E}{\tau} = \frac{N_1 E g_1}{\tau g_2} e^{-\left(\frac{E}{kT}\right)} \quad (2.3)$$

where  $N_1$  is the number of atoms of the ground state,  $N_2$  is the number of atoms in the excited state,  $E$  is the energy difference between the ground state and the excited state,  $\tau$  is the lifetime in this excited state,  $g_1$  and  $g_2$  is the statistical weights of the atoms in the ground and excited state,  $K$  is the Boltzmann constant and  $T$  is the temperature of the system. The absorption of light could be measured if the radiation from the continuous light source, such as hydrogen lamp, is passed through the population of free atom and then through a monochromator and finally to the detection system. For all the elements, the spectrum consists of a few absorption lines. The absorption peak for silver ion falls in the wavelength of 328.1 nm [9].

$\text{AgCl}$  is preferentially dissolved in ammonia solution compared to  $\text{AgI}$ . The  $K_{sp}$  values of the  $\text{AgI}$  and  $\text{AgCl}$  are  $1.8 \times 10^{-17}$  and  $8.3 \times 10^{-10}$  respectively at 298 K [10].  $\text{Ag}^+$  ions reacts with excess ammonia to form the stable complex ion  $[\text{Ag}(\text{NH}_3)_2]^+$  [11]. As a result,  $\text{AgCl}$  is quite stable in ammonia solution. Above the solubility limit of  $\text{AgCl}$  in  $\text{AgI}_{1-x}\text{Cl}_x$ ,  $\text{AgCl}$  precipitates out from the matrix. This precipitated  $\text{AgCl}$  can be dissolved in ammonia solution and the  $\text{Ag}^+$  ion can be estimated by using AAS.

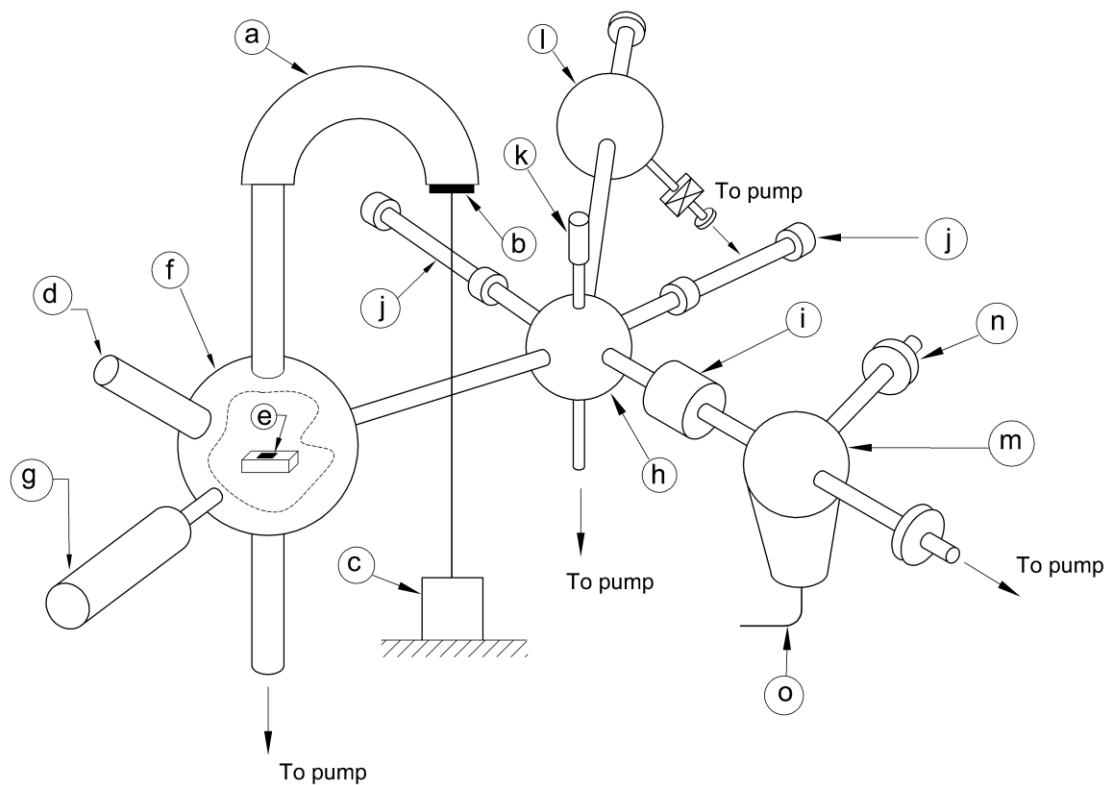
Atomic absorption spectrometric measurements were carried out in two sets: (a) on AgI (b) on  $\text{AgI}_{0.975}\text{Cl}_{0.025}$  and  $\text{AgI}_{0.95}\text{Cl}_{0.05}$ . The powders of  $\text{AgI}_{0.975}\text{Cl}_{0.025}$  and  $\text{AgI}_{0.95}\text{Cl}_{0.05}$  were studied using the as-prepared compositions and the powders calcined to a temperature of 473 K for 20 h. After mixing the respective powders with suitable ammonia solution followed by filtration, the decanted solution was analysed for  $\text{Ag}^+$  ions using atomic absorption spectrometer (M/s GBC Avanta /GFC 3000, Australia), after suitable dilution and acidification.

## 2.8 X-RAY PHOTOELECTRON SPECTROSCOPY

X-ray Photoelectron Spectroscopy (XPS) is a surface analysis technique in which a solid surface in vacuum is irradiated with X-rays to produce photoelectrons by direct transfer of energy from the X-ray photons to core level electrons in the atoms of the sample [12, 13]. The kinetic energy of the photoelectron  $E_K$  would be equal to  $(E_X - E_{BE})$ , where  $E_X$  is the energy of the X-ray used and  $E_{BE}$  is the binding energy of the respective elements. The distribution in the kinetic energy is measured and photoelectron spectrum is made after including the calibration factors of the instrument. The s-orbit electrons will appear as a single photoelectron peak whereas electrons from other orbitals will appear as doublet due to spin orbit coupling. A shift in the photoelectron peaks will reflect the change in the chemical environment of the atom, due to surface charging (if the material is non-conducting). Sketch of XPS facility used for conducting the experiments is shown in Fig. 2.2. The facility was used for studying two different kinds of problem: (a) XPS of  $\text{AgI}_{0.975}\text{Cl}_{0.025}$  and  $\text{AgI}_{0.95}\text{Cl}_{0.05}$  were taken for both as-prepared and calcined samples to understand the solubility limit of AgCl in AgI. The change in the chemical environments of both  $\text{Ag}^+$  and  $\text{I}^-$  ion will show the presence of an impurity or phase beyond the solubility of AgCl in AgI and (b) XPS patterns of AgI before and after exposure to chlorine to validate the formation of AgCl on the surface of AgI. X-ray photoelectron

spectra of the compounds were recorded using M/s SPECS make (Germany) spectrometer with 150 mm hemispherical analyser with a pass energy of 20 eV. Al  $K_{\alpha}$  X-ray radiation of 1486.6 eV was used. Powder samples were pressed on to carbon tape and XPS analyses were carried out at room temperature under a vacuum close to  $10^{-10}$  mbar. The binding energy value of Au 4f was also recorded for binding energy correction arising out of charging of samples.

The anode was operated at a voltage of 13 kV and source power level was set to 300 W. Spectra were collected using the PHOIBOS 150 analyser with a resolution of 0.6 eV for ~600 kcps at band pass energy of 20 eV. The spectrometer was calibrated using a standard silver sample. Data were processed by SpecsLab2 software. The binding energy value of Au  $4f_{7/2}$  at 84.4 eV was used as the reference to account for any charging of the sample and the peak positions were compared to standard values for identification of different elements and their oxidation states [14]. Curve fitting was carried out using Casa XPS software version 2.3.16.



- |                             |                                 |
|-----------------------------|---------------------------------|
| (a) Hemispherical analyser  | (i) Gate valve                  |
| (b) Detector                | (j) Transfer rod                |
| (c) Data acquisition system | (k) Manual control for aligning |
| (d) Monochromator           | (l) Load lock chamber           |
| (e) Sample                  | (m) Reaction chamber            |
| (f) Analysis Chamber        | (n) Gas inlet                   |
| (g) X-ray source            | (o) IR lamp                     |
| (h) Transfer chamber        |                                 |

**Fig. 2.2 Sketch of the XPS facility**

## 2.9 IONIC TRANSPORT MEASUREMENTS

In solid electrolytes, the major charge carriers would be ions, but, in some cases significant concentration of carriers can be either electrons (holes) or ions. Hebb [15] and Wagner [16] devised a method to measure the conductivity due to electrons or holes in these materials, particularly when their contribution to total conductivity is low. This method is called as ion blocking method and is also called as the DC polarisation or Wagner's asymmetric polarisation method. In this method, a small DC voltage signal 'V'

below the decomposition potential is applied to the sample, which is sandwiched between an electrode reversible with respect to the conducting ion and an inert electrode block the flow of ions. Ionic migration will occur in the sample until the cell is completely polarised. After the cell becomes completely polarised, the residual current is carried only by the electrons or holes present, in the ionic solid, while the initial value of conductivity is due to total ions and electrons/holes. In the steady state, current is due to electrons/holes only. From these measured currents, the ionic and electronic transport numbers of the solid electrolyte can be calculated.

The ionic transport number is the fraction of the total current (cationic, anionic, and electronic) carried by ions and is given by:

$$t_{\text{ion}} = \frac{i_{\text{initial}} - i_{\text{final}}}{i_{\text{initial}}} * 100 \quad (2.4)$$

$$\text{Similarly, } t_e = 100 - t_{\text{ion}} \quad (2.5)$$

where  $t_{\text{ion}}$  is the ionic transport number  $t_e$  is the electronic transport number  $i_{\text{initial}}$  is the initial current at time  $t = 0$  and  $i_{\text{final}}$  is the final current at the saturation current. Transport measurements were carried out on  $\text{AgI}_{1-x}\text{Cl}_x$  ( $x = 0-0.06$ ) using platinum stopping electrode by applying a potential of  $\sim 0.5$  V DC using Keithley 238, high current source measurement unit. Experiments were carried out in the temperature range of 298-473 K. The set-up used for the measurement is given in Fig. 2.3 for the cell configuration  $\text{Pt}|\text{AgI}_{1-x}\text{Cl}_x|\text{Pt}$ .

## 2.10 DIELECTRIC IMPEDANCE SPECTROSCOPY [17, 18 AND 19]

Impedance spectroscopy is a powerful method of characterising many of the electrical properties of the material and their interface with electronically conducting electrodes. The process involved in the bound or mobile charges in the bulk or interfacial regions of solid or liquid material, ionic, semiconducting, mixed electronic-ionic and even insulators (dielectric) can be understood using impedance spectroscopy. Of different types of

stimulus provided, generally used is a single frequency voltage or current to measure the phase shift or amplitude. Monochromatic signal  $V(t) = V_m \sin(\omega t)$  involving single frequency  $\nu = \frac{\omega}{2\pi}$  is applied to a cell and the resulting steady state current  $I(t) = I_m \sin(\omega t + \phi)$  is measured.  $V_m$  and  $I_m$  represent the amplitude of the potential and the current.  $\phi$  represents the change in the phase after the potential crosses the material of interest. Impedance ( $Z$ ) of the material can be calculated as:

$$Z = \frac{V}{I} = \frac{V_m}{I_m} \exp(-i\phi) = Z_m \exp(-i\phi) \quad (2.6)$$

where  $i = \sqrt{-1}$  and  $\phi$  is phase angle. From Euler's equation,

$$Z = Z_{\text{real}} + Z_{\text{imaginary}} \quad (2.7)$$

$$Z = Z_m \cos \phi + Z_m \sin \phi \quad (2.8)$$

The real and imaginary parts are given by  $Z_{\text{real}} = Z_m \cos \phi$  and  $Z_{\text{imaginary}} = Z_m \sin \phi$ . The plot of real versus imaginary part (known as Nyquist plot) appears as semi-circles and in some cases as a straight line. The frequency response of an elementary process can be modelled using simple electrical circuits. For example, the complex impedance plot of a parallel connection of a resistor and a capacitor gives a semicircle as shown in Fig. 2.3. Here  $R$  represents resistance,  $C$  the capacitance,  $\text{Im}\{Z\}$  and  $\text{Re}\{Z\}$  belonging to y and x axis is the imaginary and the real impedance, 'i' is the notation for the imaginary component,  $\omega$  is the angular frequency and  $\tau$  is the relaxation time for the parallel circuit. A cell with material exhibiting both ionic and electronic conduction can be considered to consist of network of resistors and capacitors parallel to each other. Each sub circuit represents different conducting processes.

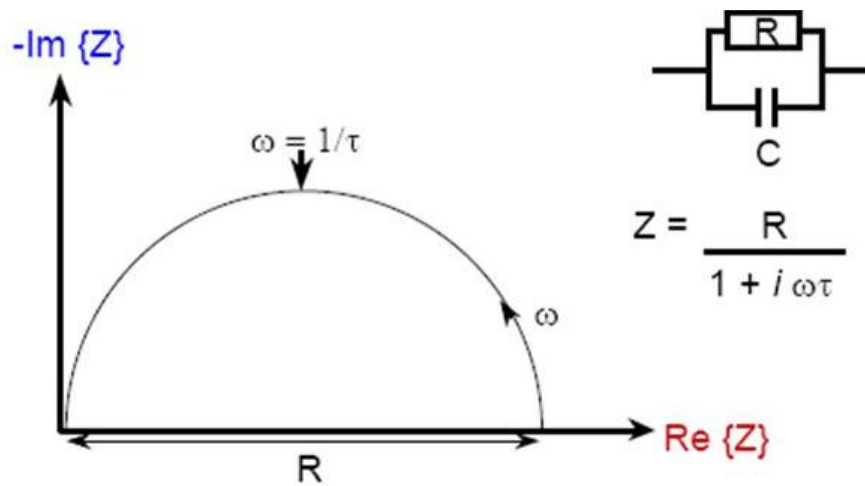


**Fig.2.3 Impedance plot of parallel combination of resistor and capacitor**

Data corresponding to high frequency region is associated with the ionic conduction process through grain bulk (intragrain), followed by process through the grain boundary (intergrain). Electrode processes are represented by the semicircle at low frequency region. These semicircles associated with different processes are separated in the impedance plane only when their time constants differ by more than two orders of magnitude. Otherwise, these semicircles would overlap. Capacitance values calculated for each semicircle is an indicator of the process associated with it. Generally, equivalent circuits employed in fitting the impedance plot will be based on simple resistors, capacitors and inductors. Practically, an electrochemical cell may have properties which are independently distributed in space [18]. The use of ideal circuit elements may not correctly fit for the curve fitting procedure adopted for such materials. The usage of distributed impedance elements like constant phase element will aid a better fit compared to the incorporation of ideal elements for curve fitting. To obtain the best fit for the material under study comes from physical intuition along with thorough literature survey for curve fitting carried out on similar materials. Impedance, admittance (inverse of impedance) and Bode (phase or amplitude) plots are commonly employed for solids. Bode plot represents a frequency response of a system with respect to the electrical property (impedance, admittance or capacitance). Bulk conductivity measurement were

carried out on  $\text{AgI}_{1-x}\text{Cl}_x$  ( $x = 0-0.1$ ), using platinum as the measuring electrode. The perturbation potential applied Bulk conductivity measurements were carried out on  $\text{AgI}_{1-x}\text{Cl}_x$  ( $x=0$  to  $0.1$ ), using platinum as the measuring electrode. The perturbation potential was 150 mV and the measurements were carried out in the range of 1 Hz-1 MHz in the temperature range of 298-473 K using air. A frequency response analyser (Model SI 1260, Solartron, M/s Schlumberger, UK) coupled with an electrochemical interface (Model 1287, Solartron, M/s Schlumberger, UK) was used. At each temperature, the specimen was allowed to equilibrate for 8 h before recording the impedance spectra. Impedance spectra were also recorded during cooling cycle using the same cooling schedule. The sketch of the two electrode set-up used for bulk conductivity studies for  $\text{AgI}_{1-x}\text{Cl}_x$  ( $x = 0-0.1$ ) is shown in the Fig. 2.4.

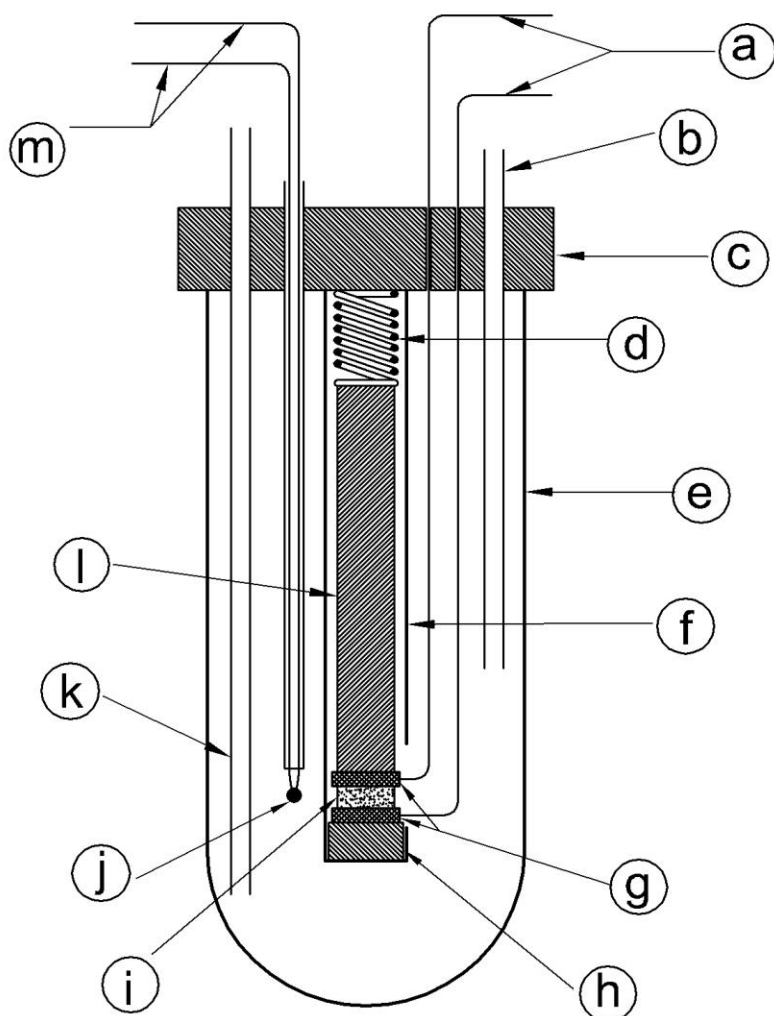
### **2.10.1 Exchange current density measurements using three electrode configuration**

At equilibrium, the potential observed is thermodynamic potential for a given chemical reaction. When there is a difference in the applied potential and the thermodynamic potential, there will be an overpotential leading to a net current flow across the cell. Under conditions of equilibrium, the concentration of the reactants and the products do not change. This means that the forward and the backward reactions take place in the same rate. Similarly, in an electrochemical cell forward and backward reactions occur simultaneously



There will be no current flowing in or out of the system under equilibrium. The current density of the forward and the backward reaction will be the same. This current density which is a kinetic parameter is called the exchange current density which depends on the type of the electrochemical reaction and the nature of the electrode. The magnitude of

exchange current density determines how easily the electrochemical reaction takes place on the electrode surface [19].



- |  |  |
|--|--|
| (a) Measurement leads                    | (h) Ceramic support                      |
| (b) Gas outlet                           | (i) $\text{AgI}_{1-x}\text{Cl}_x$        |
| (c) SS coupling                          | (j) Thermocouple                         |
| (d) SS springs                           | (k) Gas inlet                            |
| (e) Quartz tube                          | (l) Central quartz tube for cell support |
| (f) Inner quartz tube for sample loading | (m) Thermocouple leads                   |
| (g) Platinum foil                        |  |

**Fig. 2.4 Sketch of the fabrication cell for ionic transport measurements**

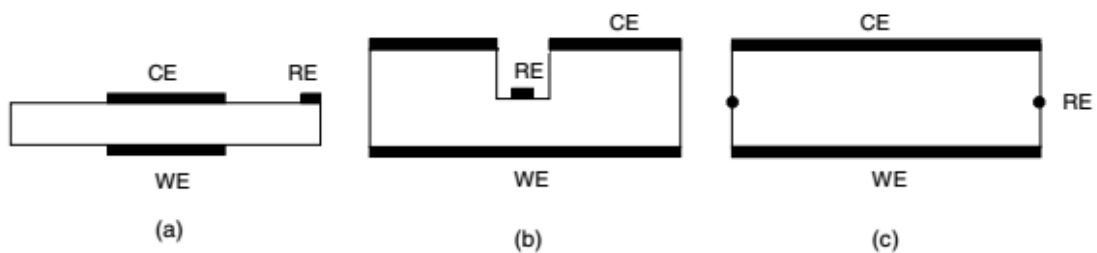
This in turn depends on the charge transfer resistance which is the barrier for electron to cross the electrolyte-electrode interface. This charge transfer is also related to overpotential. At very low over potential the exchange current density can be obtained from simplified Butler-Volmer [19] equation:

$$i = \frac{i_o n_\alpha F \eta}{RT} \quad (2.9)$$

where  $i$  is the net current,  $i_o$  is the exchange current density,  $n_\alpha$  is the apparent electron number ( $n_\alpha$  is used when there is multielectron transfer due to different electrochemical reactions in a cell),  $F$  is the Faraday's constant,  $\eta$  is the overpotential,  $R$  is universal gas constant and  $T$  is the absolute temperature. In terms of the charge transfer resistance ( $R_{CT}$ ), the equation (2.9) can be modified as

$$R_{CT} = \frac{RT}{i_o n_\alpha F} \quad (2.10)$$

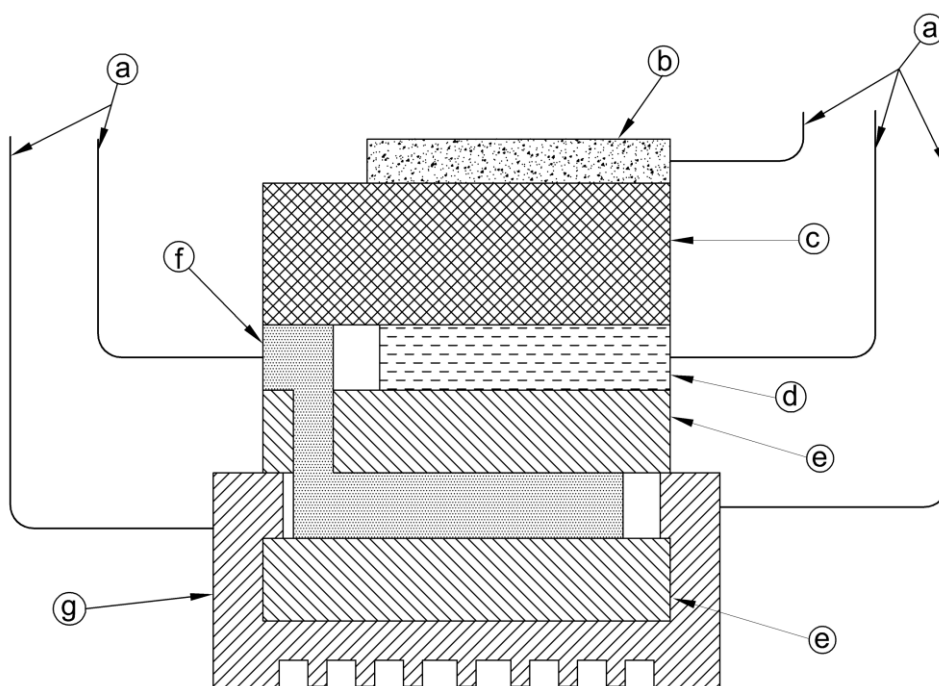
A methodology based on three electrode configuration for studying the working electrode-electrolyte interface was used to calculate the charge transfer resistance and in-turn the exchange current densities. Thus, the potential is applied across the reference and the working electrode and the current is measured across the counter and working electrode. Of the three configurations given below in Fig. 2.5, the first configuration was chosen for further studies. The counter electrode was chosen as gold, working electrode as platinum and reference electrode as silver thick films which were coated by screen printing technique. The reference and the working electrode were similar to the ones used in the sensing characterisation.



*CE: Counter Electrode, WE: Working electrode, RE: reference electrode*

**Fig. 2.5 Cell arrangements (a), (b) and (c) for studying three electrode configuration [18]**

The frequency at which the diffusion process or the formation of a capacitive layer can be resolved using the impedance spectroscopy. Such frequency dependence (dispersion) is due to the fact that all slow electrode processes are eliminated from the measurements at the increase in the frequency. In the ideal case, at high frequencies, only bulk-resistance of electrolyte,  $R_e$  and capacitance of the electric double layer,  $C_{dl}$  are measured, with respect to the charge transport in the solid electrolyte. As the frequency decreases, on the contrary, slow processes occurring in the electrolyte near electrode layers can be included in the measurements, such as diffusion and adsorption at the electrode interface and also electrochemical reactions are complicated by slow chemical transitions. Different combinations of equivalent circuits for different electrochemical processes of adsorption, diffusion, etc. are explained in Bukun and Ukshe [20]. A sketch of the cell used for the three electrode measurement in the present investigations is shown in Fig. 2.6.



- |   |                                |
|---|--------------------------------|
| (a) Gold leads                          | (d) Gold counter electrode     |
| (b) Platinum working electrode          | (e) Alumina                    |
| (c) $\text{AgI}_{0.95}\text{Cl}_{0.05}$ | (f) Silver reference electrode |
|   | (g) Platinum heater            |

**Fig. 2.6 Sketch of the three electrode configuration**

The platinum heater in the configuration (Fig. 2.6) was calibrated by placing a thermocouple on top of the alumina substrate, where the pellet was mounted. The voltage and the current, required to maintain the desired temperature on the top of the pellet, was measured using digital panel meter. The temperature above the pellet was then fixed at 428 K facing the working electrode. The perturbation potential of 150 mV was given by using Autolab work station (M/s Autolab Ecochiemie BV, PGSTAT 302). After thermal equilibration, blank runs were carried out on the sample at 428 K. Iodine gas was admitted using dry air maintaining the concentration around 40 vppm. The impedance patterns were recorded after 7 min of the gas injection. After the measurement, iodine in the chamber was removed by flowing dry air. The experiment was repeated three times to observe the consistency with an interval of 2 h. A concentration of 500 vppb of chlorine

was injected into the cell and the impedance patterns were recorded after 7 min of injection. The impedance pattern of the cell was recorded after every 2 h of injection. The pellet was then removed and taken for XPS analysis.

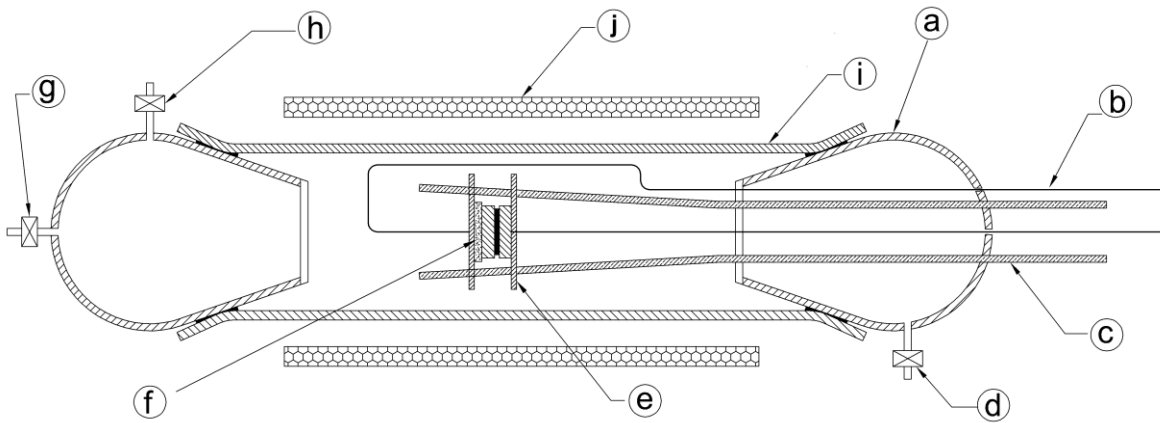
## 2.11 SENSOR SET-UP

Selectivity for the specific analyte gas and the functional independence from geometry make potentiometric sensors more significant in the chemical sensor regime [21]. The potentiometric sensor employed for sensing iodine and chlorine is of the following configuration:

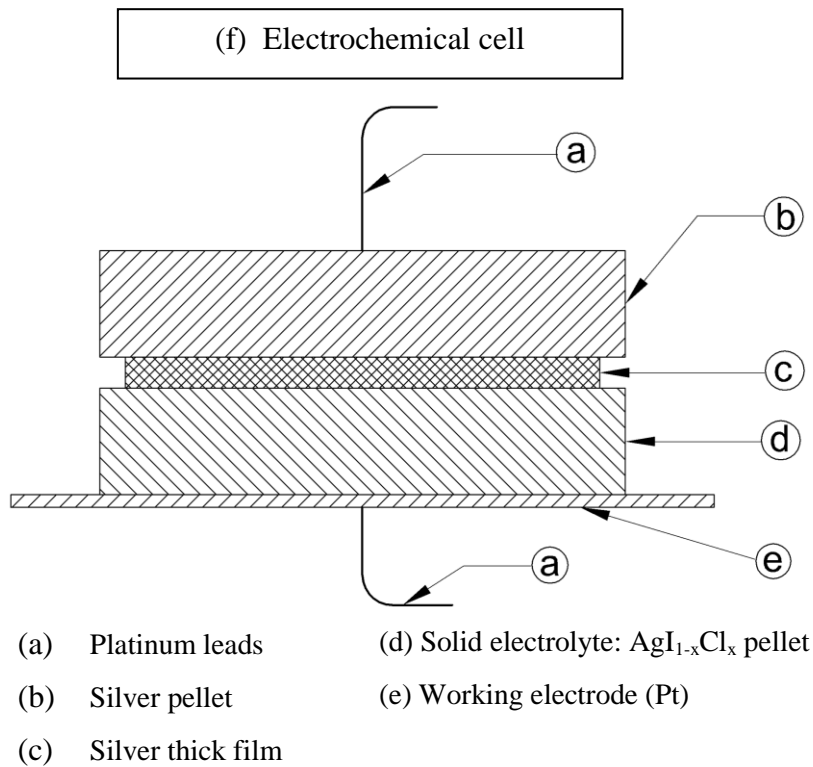


where,  $\text{X}_2=\text{I}_2/\text{Cl}_2$ . The sketch of the sensor assembly used for studying the sensing characteristics of the respective electrolytes is shown in Fig. 2.7. The enlarged version of the electrochemical cell is also shown in Fig. 2.7.

In this configuration, a pellet of  $\text{AgI}_{1-x}\text{Cl}_x$  was packed between the platinum (foil) working electrode and the silver reference electrode. The platinum lead wires are connected to the platinum foil and silver pellet (in contact with the thick film of silver employed as reference). A thermocouple placed on the glass chamber measures the temperature of the central zone of the furnace. The sample pellet was placed in the central zone, which is maintained at  $\pm 1\text{K}$ .



- |                                  |                          |
|----------------------------------|--------------------------|
| (a) Ground joint (glass chamber) | (f) Electrochemical cell |
| (b) Platinum leads               | (g) Gas injection port   |
| (c) Supporting rod               | (h) Gas inlet            |
| (d) Gas outlet                   | (i) Glass chamber        |
| (e) Pyrophyllite support         | (j) Furnace coils        |



- |                       |   |
|-----------------------|---|
| (a) Platinum leads    | (d) Solid electrolyte: $\text{AgI}_{1-x}\text{Cl}_x$ pellet |
| (b) Silver pellet     | (e) Working electrode (Pt)                                  |
| (c) Silver thick film |   |

**Fig. 2.7 Sketch of the sensor set-up used for studying bulk pellets**

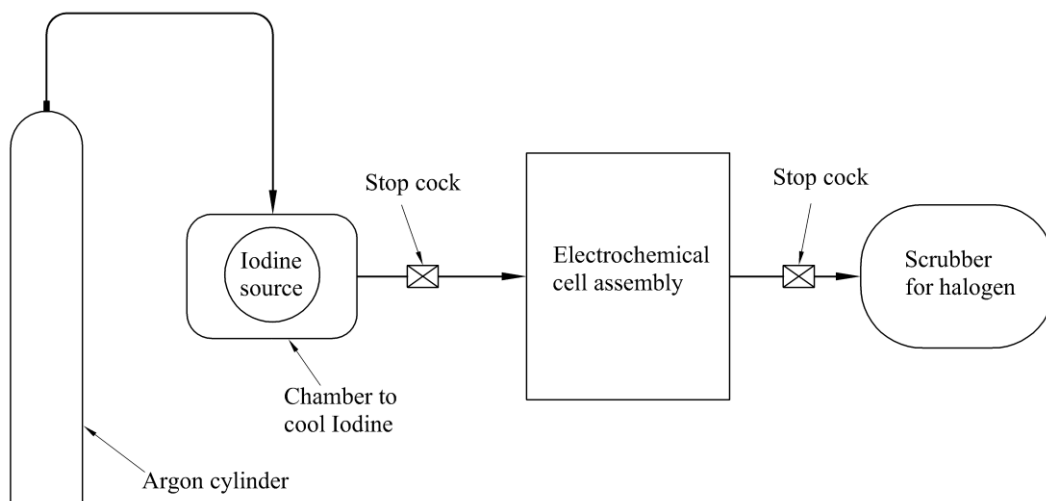


**Fig. 2.8 Schematic of the dynamic flow experiment for iodine sensing studies**

Iodine was admitted into the cell in a dynamic mode where the flow rate of the Ar gas was fixed at 10 mL/min. The flowchart of the dynamic flow experiment is shown in Fig. 2.8, where the partial pressure of the gas is fixed maintaining the temperature of the iodine chamber. The iodine chamber temperature was reduced by using a cryogenic bath, which will in turn control the partial pressure of iodine. From the partial pressure of iodine at the temperature of study, the concentration of iodine was calculated using the partial pressure vs temperature plot reported [22]. The range of iodine concentration studied for  $\text{AgI}_{1-x}\text{Cl}_x$  was from ~6-60 vppm.

Chlorine was injected into the cell using a syringe. The silicone septum attached to a PTFE veeco fitting was used as a port for injecting gas into the chamber using a syringe. The range of chlorine gas studies for bulk pellets were from 20 to 100 vppb in air at 428 K.

### 2.11.1 Miniaturised chlorine sensor

A miniaturised form of the potentiometric cell was fabricated with  $\text{AgI}_{0.95}\text{Cl}_{0.05}$  as the solid electrolyte. The cell was tested towards chlorine gas in the concentration range of 17 to 15000 vppb at 428 K. A photograph of the miniaturised sensor is shown in Fig. 2.9.

- (a) Teflon vecco fittings to inject the gas
- (b) Glass chamber
- (c) Gas inlet for purging dry air
- (d) Electrochemical cell
- (e) Gas outlet
- (f) Teflon wires connecting to instrument

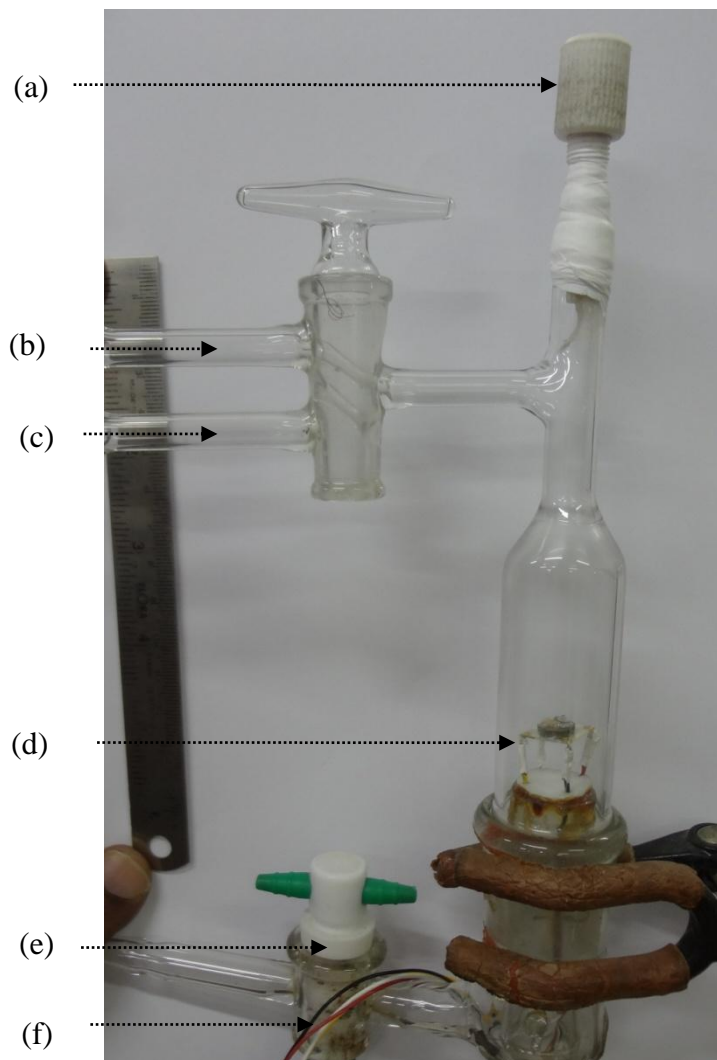


**Fig. 2.9 Photograph of miniaturised chlorine sensor**

## 2.12 CONCLUSIONS

The results and patterns obtained from these experimental techniques of characterisation are analysed in Chapter 3 and the results will be presented in the same chapter. The comparisons of results from different parameters derived are also highlighted in the chapter. The use of the fabricated set-up for sensing of iodine and chlorine is presented in chapter 4 for studying the sensing characteristics of  $\text{AgI}_{1-x}\text{Cl}_x$ . Finally, the chlorine sensing of  $\text{AgI}$ , explored using the three electrode configuration, is discussed in chapter 5. The miniaturisation of the potentiometric cell for sensing chlorine using  $\text{AgI}_{0.95}\text{Cl}_{0.05}$  is highlighted in chapter 6.

## 2.13 REFERENCES

1. Limit of resolution: X-ray diffraction, 2000, Elementary physics II, Physics Department, Boston University, United Kingdom, Summer 2000, <http://physics.bu.edu/py106/notes/Resolution.html> [Accessed on 05<sup>th</sup> June 2017]
2. S. Ihara, Y. Warita and K. Suzuki, 1984, Ionic conductivity in  $\text{AgI}_{1-x}\text{Cl}_x$ , *Physica Status Solidi A*, 86, 729-734
3. B.D. Cullity, 1956, *Elements of X-ray diffraction*, Addison Wesley Publishing Company Inc., 509 pp
4. P. Echlen, C. E. Fiori, D. E. Newbury, D.C Joyand and J. I. Goldstein, 1986, *Advanced scanning electron microscopy and X-ray microanalysis*, Springer Unites States, 454 pp
5. F.V. Voort, 2004, *Metallography and microstructure*, ASM International, 752 pp
6. W.M. Wendlandt, 1974, *Thermal methods of analysis*, 2<sup>nd</sup> ed., Wiley Interscience, New York, 505 pp
7. J.W. Dodd and K.H. Tonge, 1987, *Thermal methods*, ACO/Wiley, London, 377 pp
8. J.E. Cantle, 1986, *Atomic absorption spectrometry*, Elsevier Scientific Publishing Company, 447 pp
9. M.A. Karimi, S.Z. Mohammadi, A. Mohadesi, A.H. Mehrjardi, M.M. Ardakani, L.S. Korani and A.A. Kabir, 2011, Determination of silver (I) by flame atomic absorption spectrometry after separation/pre-concentration using modified magnetite nanoparticles, *Scienta Iranica*, Vol.18, Issue 3, pp 790-796
10. R.M. Barrer, 1941, *Diffusion in and through solids*, NY: The MacMillan Company, 460 pp
11. S.S. Zumdahl and D.J. Decoste, 2015, *Chemical principles*, 8<sup>th</sup> ed., Cengage Learning, United States of America, 888 pp

12. D. Briggs and M. P. Seah, 1990, Practical surface analysis by Auger and X-ray photoelectron spectroscopy, John Wiley and Sons, New York, 657 pp
13. M. Campagna, G. K. Wertheim, H. R. Shanks, F. Zumsteg, and E. Banks, 1975, Local character of many-body effects in X-ray photoemission from transition metal compounds:  $\text{Na}_x\text{WO}_3$ , Physical Review Letters, 34, 738-741
14. J.F. Moulder, W.F. Stickle, P.E. Sobol, K.D. Bomben and J. Chastain, 1991, Handbook of X-ray photo-electron spectroscopy, Physical Electronics Inc., 255 pp
15. M.H. Hebb, 1952, Electrical conductivity of  $\text{Ag}_2\text{S}$ , Journal of Chemical Physics, 20, 185-190
16. C. Wagner, 1956, Galvanische Zellen mit festen Elektrolyten gemischter Stromleitung, Zeitschrift für Elektrochemie, 4, 60-69
17. M.E. Orazem and B. Tribollet, 2008, Electrochemical impedance spectroscopy, John Wiley & Sons Inc, Canada, 518 pp
18. E. Barsoukov (ed.) and J.R. Macdonald (ed.), 2005, Impedance spectroscopy: theory, experiment, and applications, 2<sup>nd</sup> ed., John Wiley & Sons, New York, 616 pp
19. X.Z. Yuan, C. Song, H. Wang and J. Zhang, 2010, Electrochemical impedance spectroscopy in PEM fuel cells, Springer-Verlag Ltd., London, 413 pp
20. N. G. Bukun and A. E. Ukshe, 2009, Impedance of solid electrolyte system, Russian Journal of Electrochemistry, 45, No.1, 11-24
21. W. Weppner, 1987, Solid state electrochemical gas sensors, Sensors and Actuators, 12, 107-119
22. G.P. Baxter, C.H. Hickey, W.C. Holmes, 1907, The vapour pressure of iodine, Journal of American Chemical Society, 29, 127-136

**CHAPTER 3**  
**PHYSICOCHEMICAL CHARACTERISATION OF**  
**AgI<sub>1-x</sub>Cl<sub>x</sub> (x=0-0.25)**

**3.1 INTRODUCTION**

The phase identification and transformations, solubility limit of AgCl in AgI, morphological characterisation and electrical conductivity measurements were carried out on AgI<sub>1-x</sub>Cl<sub>x</sub> (x=0-0.25). Experiments to determine the solubility limit of AgCl in AgI was carried out using X-ray diffraction (XRD), X-ray photoelectron spectroscopy (XPS) and atomic absorption spectrometry (AAS) and the results from these studies are presented in this chapter. The correlations between the results from these techniques and scanning electron microscopy (SEM) for the solubility limit are also dealt with in this chapter. The results of phase transition from  $\beta$  to  $\alpha$  phase of AgI and its variation with the addition of AgCl is also described based on differential scanning calorimetric (DSC) studies and electrical conductivity measurements.

**3.2 EXPERIMENTAL**

As described in chapter 2, there are two sets of samples which were characterised and are discussed in this chapter: (a) as-prepared after the preliminary preparation and digestion of the precipitate and (b) samples calcined at 473 K. The measurements were carried out in duplicate to confirm the results obtained in all the measurements.

**3.3 X-RAY DIFFRACTION STUDIES (XRD)**

X-ray diffraction studies of the prepared AgI sample shows formation of dominant hexagonal  $\beta$ -AgI phase along with the face centred  $\gamma$ -AgI phase (Fig. 3.1 (a-c)). As  $\gamma$ -AgI shares the most intense XRD peaks along with  $\beta$ -AgI, the distinction for the presence of  $\gamma$ -AgI was obtained from the peaks at  $2\theta$  values of 56.66 and 62.25 corresponding to (400) and (331) reflections. The intensities of  $\beta$ -AgI phase from the ICDD pattern (ICDD-AgI-00-009-0374) [1] is represented in Fig 3.1(b). The  $\gamma$ -AgI phase of AgI with ICDD

index AgI-00-009-0399 is represented in Fig. 3.1(c). The  $\alpha$ -phase of AgI transforms into  $\beta$  and  $\gamma$  polymorphs [2] upon cooling from high temperature.

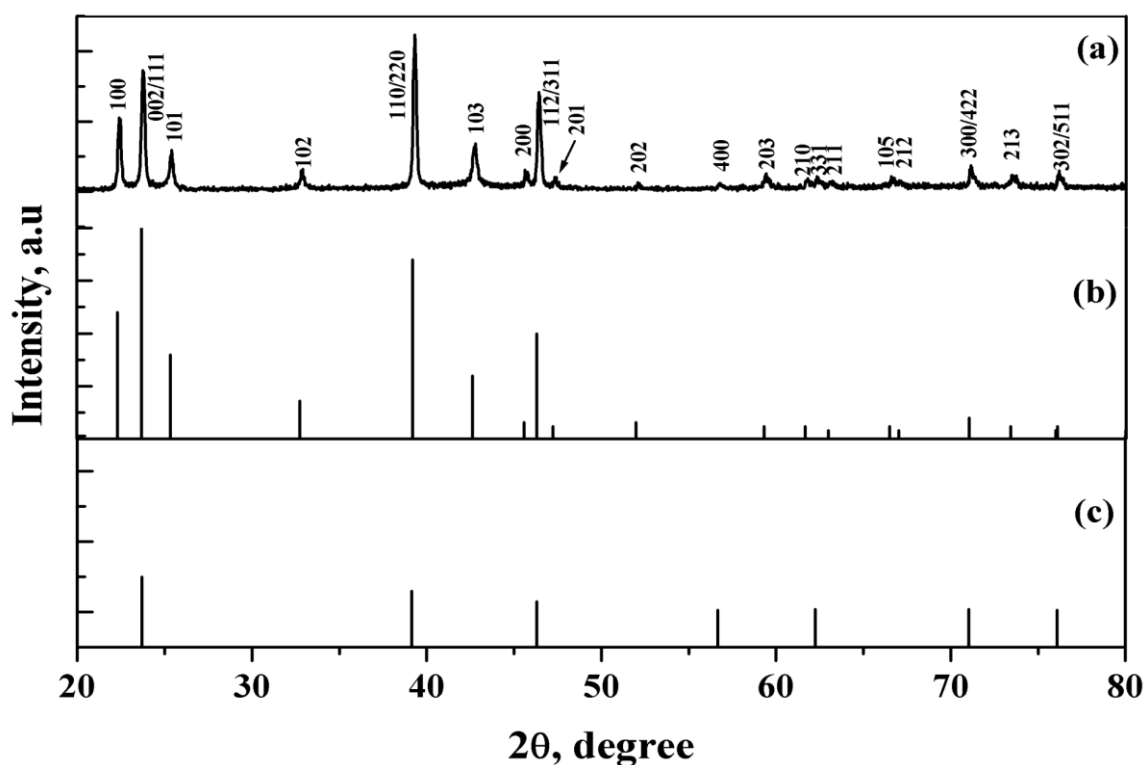


**Fig. 3.1 XRD pattern of (a) AgI as-prepared (Before slash (/) indexing:  $\beta$ -AgI and after indexing:  $\gamma$ -AgI and ICDD patterns of (b)  $\beta$ -AgI (ICDD-AgI-00-009-0374) and (c)  $\gamma$ -AgI (ICDD-AgI-00-009-0399)**

The XRD patterns of nominal compositions,  $\text{AgI}_{1-x}\text{Cl}_x$  ( $x = 0$  to  $0.25$ ) are shown in Fig. 3.2 (a) to (d). Major reflections of cubic AgCl at  $2\theta = 27.28$ ,  $31.58$  and  $45.38$  from the respective planes of (111), (200) and (220) (ICDD-AgCl-00-001-1013) were observed for compositions of  $x \geq 0.05$  in  $\text{AgI}_{1-x}\text{Cl}_x$ . The solubility limit of around 6 mol% of AgCl in AgI was reported by Ihara et al. by measuring the  $\beta$ -AgI to  $\alpha$ -AgI phase transition temperature [3] and also from the phase diagram of AgCl and AgI [4]. From the present studies using XRD, the solubility limit of AgCl in AgI is found to be less than 5 mol%, which is reasonably close to the reported solubility limit determined by Ihara et al. [3].

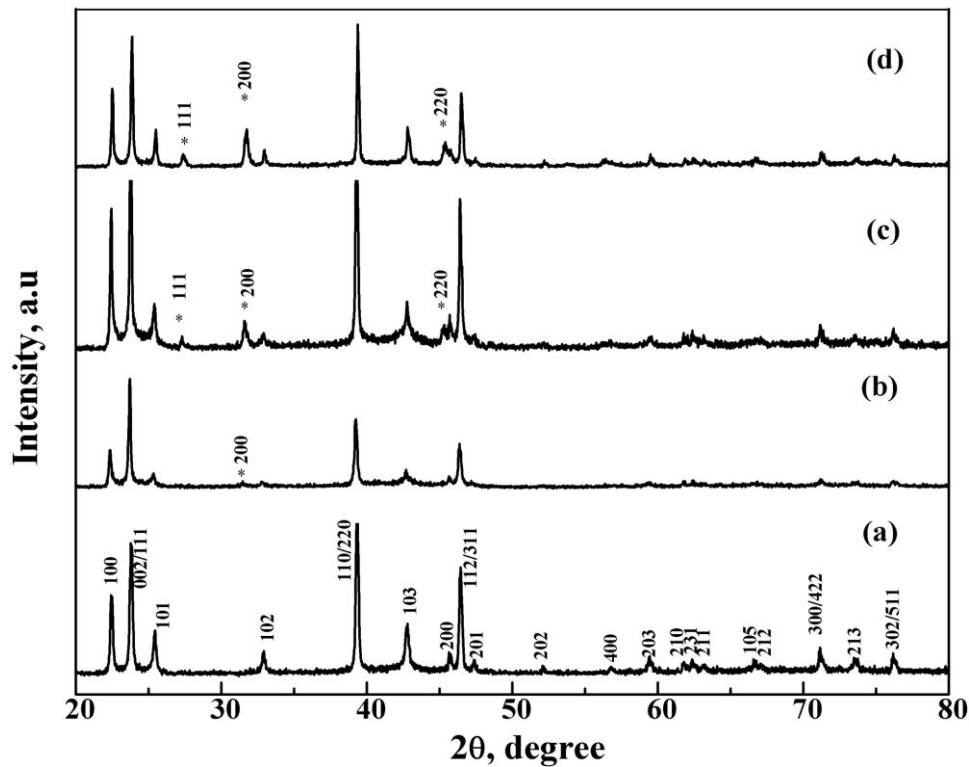


Fig. 3.2 XRD pattern of  $\text{AgI}_{1-x}\text{Cl}_x$  with  $x$  as (a) 0, (b) 0.05, (c) 0.1 and (d) 0.25.  
 (\*) represents the precipitated cubic AgCl phase (ICDD-AgCl-00-001-1013)

### 3.3.1 Unit cell volume calculation

The lattice parameters calculated using Scherrer formula [5] for the compositions of  $\text{AgI}_{1-x}\text{Cl}_x$  is given in Table 3.1 below. An error of ( $\pm$ ) 10 % was observed from the lattice parameter calculations carried out on  $\text{AgI}_{1-x}\text{Cl}_x$ .

Table 3.1 Lattice parameters of  $\text{AgI}_{1-x}\text{Cl}_x$  ( $x=0$  to 0.1)

| Sl.No | $\text{AgI}_{1-x}\text{Cl}_x$<br>$x$ is | Lattice parameter* |          |
|-------|---|--------------------|----------|
|       |   | $\text{\AA}$       |          |
|       |   | <b>a</b>           | <b>c</b> |
| 1.    | 0                                       | 4.58               | 7.46     |
| 2.    | 0.025                                   | 4.59               | 7.50     |
| 3.    | 0.05                                    | 4.59               | 7.49     |
| 4.    | 0.1                                     | 4.58               | 7.49     |

\*Deduced from the XRD patterns recorded. The error for the estimate is ( $\pm$ ) 10 %

Since the crystal structure of AgI and AgCl are hexagonal and cubic at room temperature respectively [6], the lattice parameter variation after incorporating AgCl in AgI will be different in different directions of unit cell. Therefore, the change in the cell dimension can be seen by calculating the unit cell volume for each composition. The unit cell

volume of  $\text{AgI}_{1-x}\text{Cl}_x$  from the lattice parameter for the composition was calculated based on the following equation [7]:

$$V = \sqrt{3} * a^2 * \frac{c}{2} = 0.866 * a^2 * c \quad (3.1)$$

The volume calculated using the above equation for respective compositions are given in Table 3.2. From the data, there was no appreciable change in cell volume with increasing  $\text{Cl}^-$  addition even though the ionic radius of  $\text{Cl}^-$  (ionic radii: 1.81 Å [8]) is smaller than that of  $\text{I}^-$  (ionic radii: 2.2 Å). The variation of the cell volume is within the error limit of estimation.

**Table 3.2 Cell volume of  $\text{AgI}_{1-x}\text{Cl}_x$  where (x=0 to 0.1)**

| Sl.No | $\text{AgI}_{1-x}\text{Cl}_x$<br>x is | Unit cell volume*<br>(Å) <sup>3</sup> |
|-------|---------------------------------------|---------------------------------------|
| 1.    | 0                                     | 135.92                                |
| 2.    | 0.025                                 | 136.94                                |
| 3.    | 0.05                                  | 136.69                                |
| 4.    | 0.1                                   | 136.38                                |

\*Calculated from the lattice parameters Table 3.1. Error for the estimate is ( $\pm$ ) 10 %.

There should be a decrease in the unit cell dimension due to the incorporation of  $\text{Cl}^-$  in AgI matrix as reported by Ihara et al. [3]. However, the present investigations did not reveal any change in the lattice parameter or volume. The values of lattice parameter obtained in the present study matched with that of the reported literature data. The quantitative value of lattice loosening ( $\eta$ ) [9] was calculated by using  $\frac{S_x}{S_{\text{Ag}}}$  as defined in the paper of Ihara et al., where,  $S_{\text{Ag}}$  is defined as  $\pi r_{\text{Ag}}^2$  ( $r$  is the ionic radius of the  $\text{Ag}^+$  ion).  $S_x$  for the above calculation [3] was taken from the respective ionic radius of the anions ( $\text{I}^-$  and  $\text{Cl}^-$ ) and the lattice parameters of the respective compositions and is given in equation (3.2). The calculated value of lattice loosening ( $\eta$ ) occurring due to the addition of  $\text{Cl}^-$  in AgI is given Table 3.3.

$$S_x = \frac{\sqrt{3}}{4} * a^2 * \frac{\pi}{2} \{ (1-x)r_{\text{I}^{(-)}}^2 - xr_{\text{Cl}^{(-)}}^2 \} \quad (3.2)$$

where  $a$  is the lattice parameter of  $\text{AgI}_{1-x}\text{Cl}_x$  ( $x=0-0.1$ ),  $x$  is the concentration of  $\text{Cl}^-$  ion,  $r_{\text{I}^-}$  is the ionic radius of  $\text{I}^-$  ion,  $r_{\text{Cl}^-}$  is the ionic radius of  $\text{Cl}^-$  ion.

**Table 3.3 Value of lattice loosening for  $\text{AgI}_{1-x}\text{Cl}_x$**

| Sl.No | $\text{AgI}_{1-x}\text{Cl}_x$<br>$x$ | Lattice loosening<br>$\eta = \frac{S_x}{S_{\text{Ag}}}$ |
|-------|--------------------------------------|---|
| 1.    | 0                                    | 0.166   |
| 2.    | 0.025                                | 0.159   |
| 3.    | 0.05                                 | 0.152   |
| 4.    | 0.1                                  | 0.142   |

From the above values there is no appreciable change in the lattice loosening as the calculated values are within ( $\pm$ ) 10 % deviation. Therefore, the substitution of  $\text{Cl}^-$  in  $\text{AgI}$  gives rise to negligible lattice loosening, which is also seen in the case of unit cell volume calculations.

### 3.4 MORPHOLOGICAL CHARACTERISATION

Scanning electron microscopy images are shown in Fig. 3.3 and 3.4. The images shows dense surface of  $\text{AgI}$  with average particle size of around 150 nm. The smaller grains are due to the coated gold particles used for conduction of the pellet under study in Fig. (3.3 (a) and (b)). On comparing the average particle size for  $\text{AgI}$  to  $\text{AgI}_{0.975}\text{Cl}_{0.025}$ , there was little variation in the average particle size (Fig. 3.3 (b)). There is a distinct change in the morphology in  $\text{AgI}_{0.95}\text{Cl}_{0.05}$  when compared with  $\text{AgI}$  (Fig. 3.4 (a)), where agglomerates are seen along with the main matrix. This could be due to the precipitation of  $\text{AgCl}$  from the  $\text{AgI}_{0.95}\text{Cl}_{0.05}$  as the composition  $\text{AgI}_{0.95}\text{Cl}_{0.05}$  is just above the solubility limit as observed in XRD patterns. The precipitate of  $\text{AgCl}$  is more pronounced in Fig. 3.4 (b) for  $\text{AgI}_{0.94}\text{Cl}_{0.06}$  which confirms that the agglomerates distinctly seen from the main matrix is due to the precipitation of  $\text{AgCl}$ . These results again corroborate the observations from X-ray diffracted patterns which show the reflection from  $\text{AgCl}$  planes above the 5 mol%  $\text{AgCl}$  in  $\text{AgI}$ .

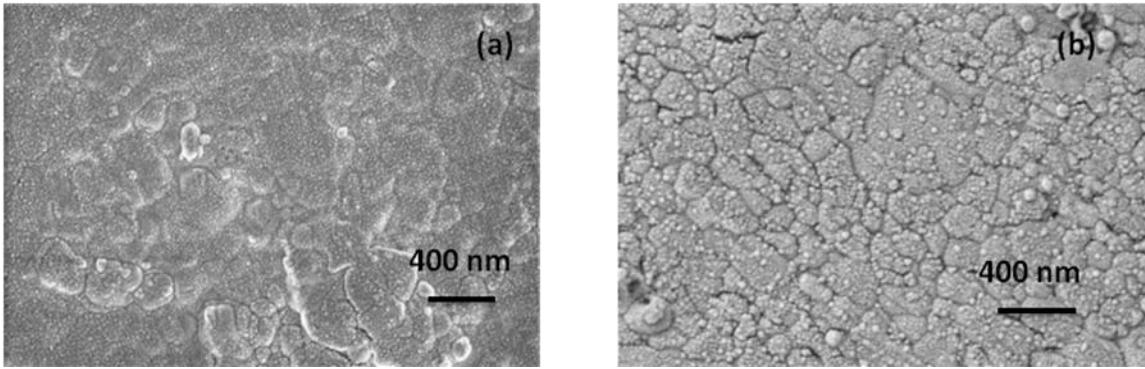


**Fig. 3.3** Scanning electron microscope images of (a) AgI and (b)  $\text{AgI}_{0.975}\text{Cl}_{0.025}$

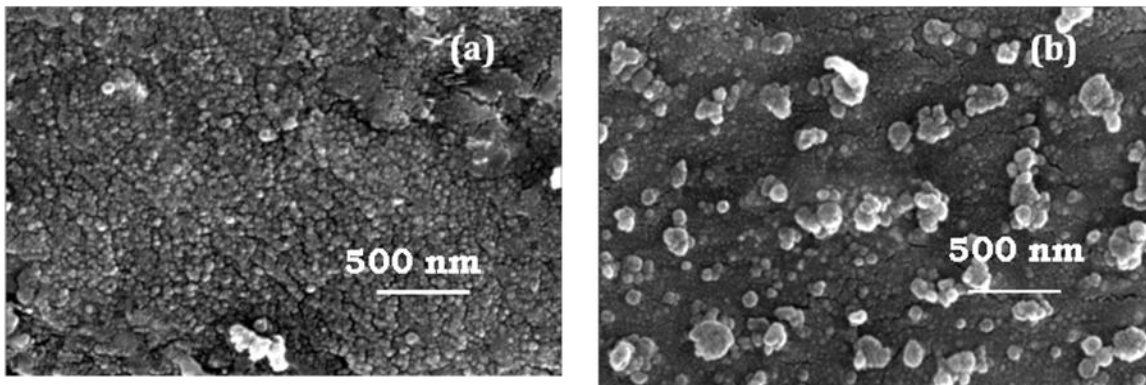


**Fig. 3.4** Scanning electron microscope images of (a)  $\text{AgI}_{0.95}\text{Cl}_{0.05}$  and (b)  $\text{AgI}_{0.94}\text{Cl}_{0.06}$

The EDX patterns (Fig. 3.5 and 3.6) for  $\text{AgI}_{0.975}\text{Cl}_{0.025}$  and  $\text{AgI}_{0.94}\text{Cl}_{0.06}$ , are observed to be significantly different from the morphologically different areas, showing a large variation in the  $\text{Cl}^-$  concentration in the regions which are brighter compared to darker regions. This corroborates the precipitation of AgCl in  $\text{AgI}_{1-x}\text{Cl}_x$  compositions as the observed solubility limit was around  $x \sim 0.05$  from XRD studies.

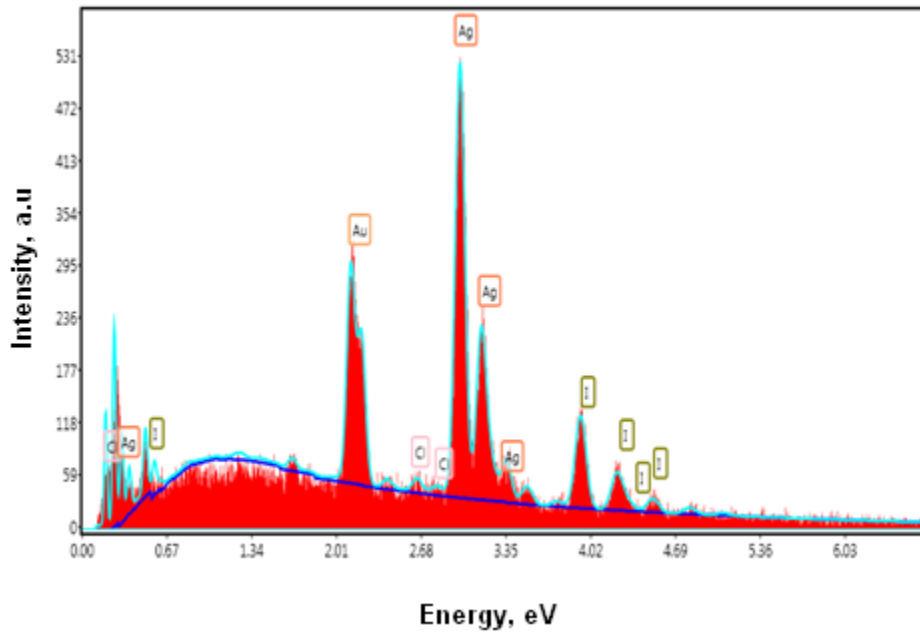


**Fig. 3.5** EDX of  $\text{AgI}_{0.975}\text{Cl}_{0.025}$  for the image shown in Fig. 3.3 (b) in a specified spot

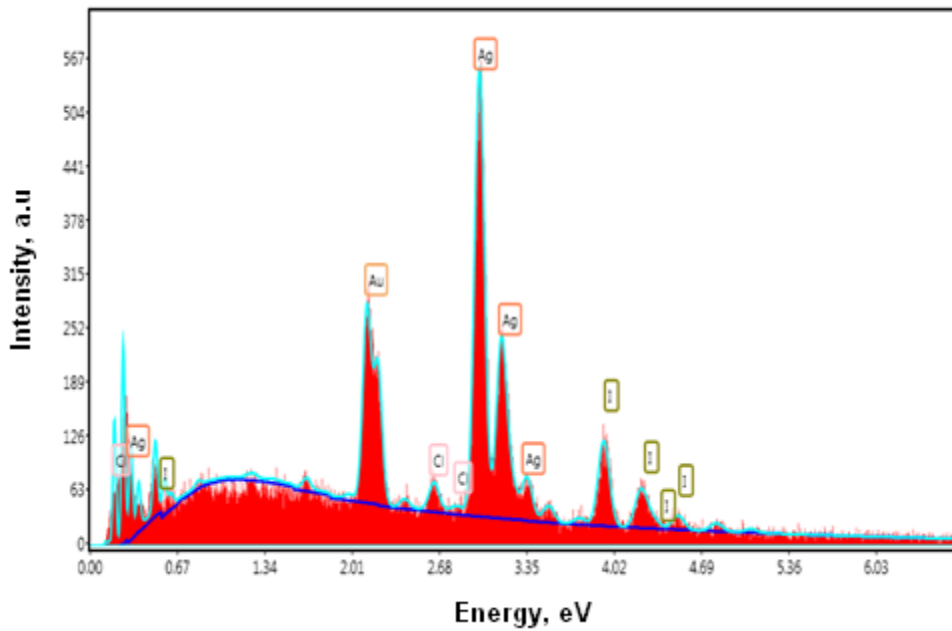


**Fig. 3.6** EDX of  $\text{AgI}_{0.94}\text{Cl}_{0.06}$  for the image shown in Fig. 3.4 (b) in a specified spot appearing as clusters

### 3.5 DIFFERENTIAL SCANNING CALORIMETRIC (DSC) MEASUREMENTS

To understand the thermal characteristics of the  $\text{AgI}_{1-x}\text{Cl}_x$ , DSC studies were carried out. The plots obtained from DSC measurements carried out on  $\text{AgI}_{1-x}\text{Cl}_x$  ( $x=0$  to  $0.1$ ) are shown in Fig. 3.7 to 3.11. The plot of AgI shows onset of  $\beta$  to  $\alpha$  phase transition temperature around 420 K. Further, increasing the concentration of  $\text{Cl}^-$  in AgI shows a melt-type transition. The phase transition temperature was found to reduce from  $\sim 420$  K in AgI to  $\sim 404$  K in  $\text{AgI}_{0.975}\text{Cl}_{0.025}$ . Also, for composition above  $x \geq 0.05$ , the onset of  $\beta$  to  $\alpha$  phase transition temperature was also found to be around 404 K. All the compositions above  $x \geq 0.05$  in  $\text{AgI}_{1-x}\text{Cl}_x$  were found to have nearly the same onset temperature for phase transition. The incorporation of  $\text{Cl}^-$  into the  $\beta$ -AgI structure will cause defects in the hexagonal crystal lattice. The defects in such crystals can be incorporated as long as the crystal structure can withstand the distortions. Beyond the critical defect concentration [10], the lattice will no longer withstand the distortion and will change to the disordered or high temperature phase ( $\alpha$ -phase). Also, as the crystal structures of AgI and AgCl are different below the  $\beta$  to  $\alpha$  phase transition temperature, this could lead to the enhancement of Frenkel defects in the crystal [3]. This shows that above  $x \geq 0.05$ , the crystal structure of AgI could not accommodate AgCl. It was also observed that there were two different slopes in the  $\beta$  to  $\alpha$  transition region. This could be due to the difference in the lattice structure as the structure of AgCl is cubic and that of AgI is hexagonal before the phase transition. This is clearly resolved when the concentration of AgCl is less in AgI. But for  $\text{AgI}_{0.9}\text{Cl}_{0.1}$ , in Fig. 3.11, the difference in slope for the phase transition is not seen, which shows that the concentration of AgCl is sufficiently larger so that the heat required for the crystal structure transformation becomes unresolved compared to the phase transition. The above interpretation can be correlated to the phase diagram shown in Fig. 3.12. For the transition around 419 K, corresponding to the phase change from  $\beta/\gamma$ -phase to  $\alpha$ -phase, the slope is negative in the phase diagram as seen in Fig. 3.12. Therefore, the temperature for phase transition for the compositions of  $\text{AgI}_{1-x}\text{Cl}_x$  in the range  $0 \leq x \leq 0.1$ , decreases with addition of  $\text{Cl}^-$  in AgI.

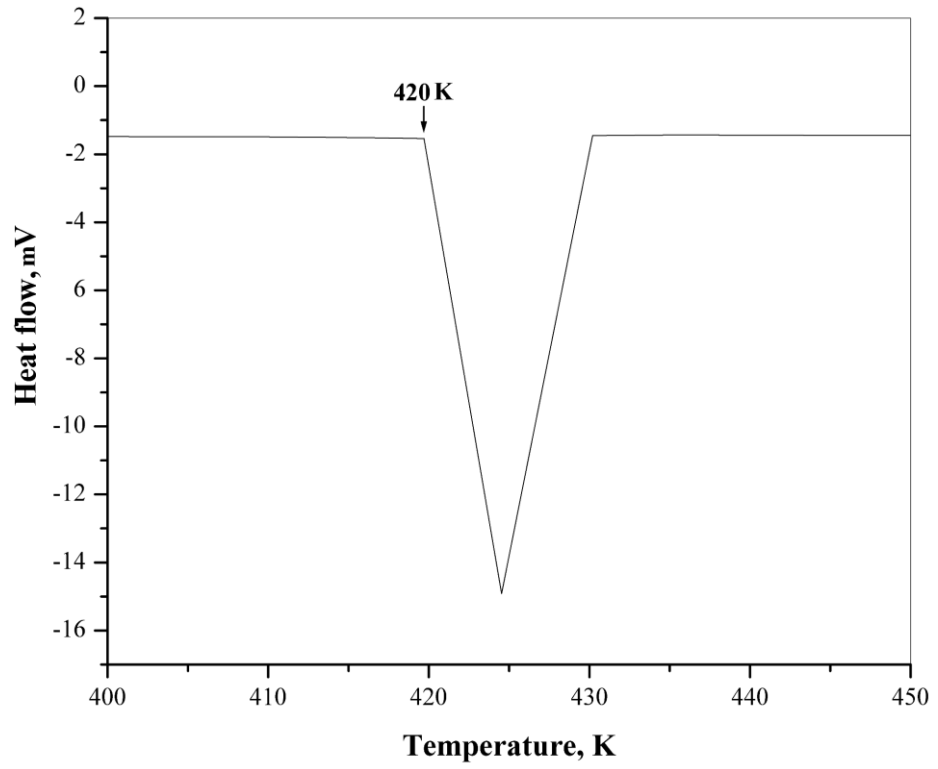


Fig. 3.7 DSC pattern of AgI

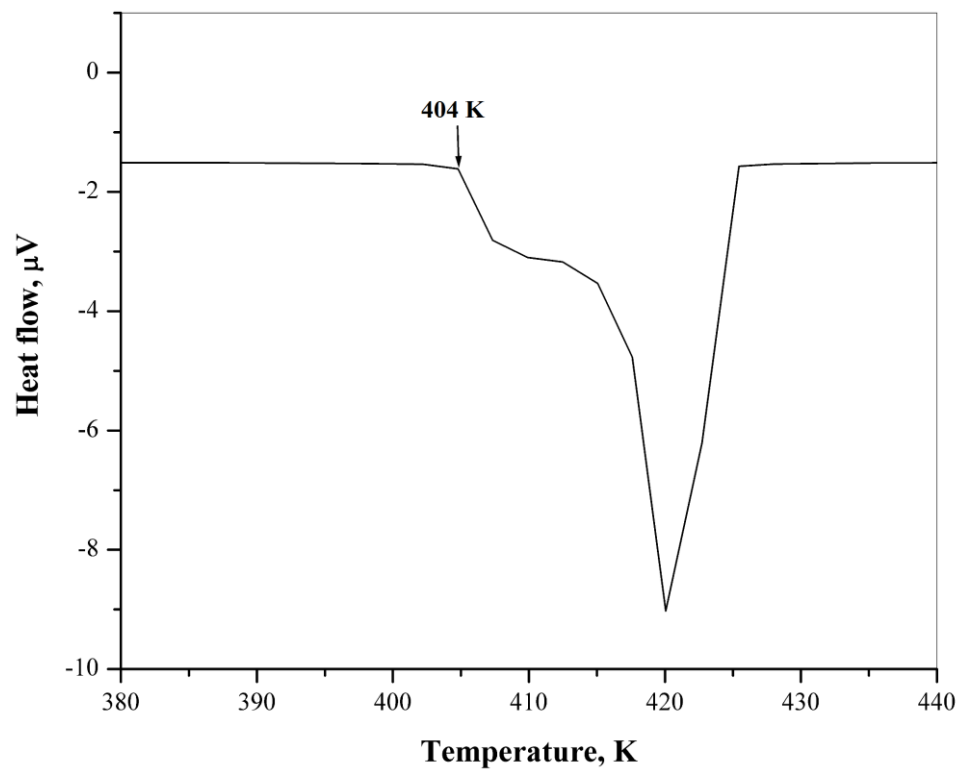


Fig. 3.8 DSC pattern of AgI<sub>0.975</sub>Cl<sub>0.025</sub>

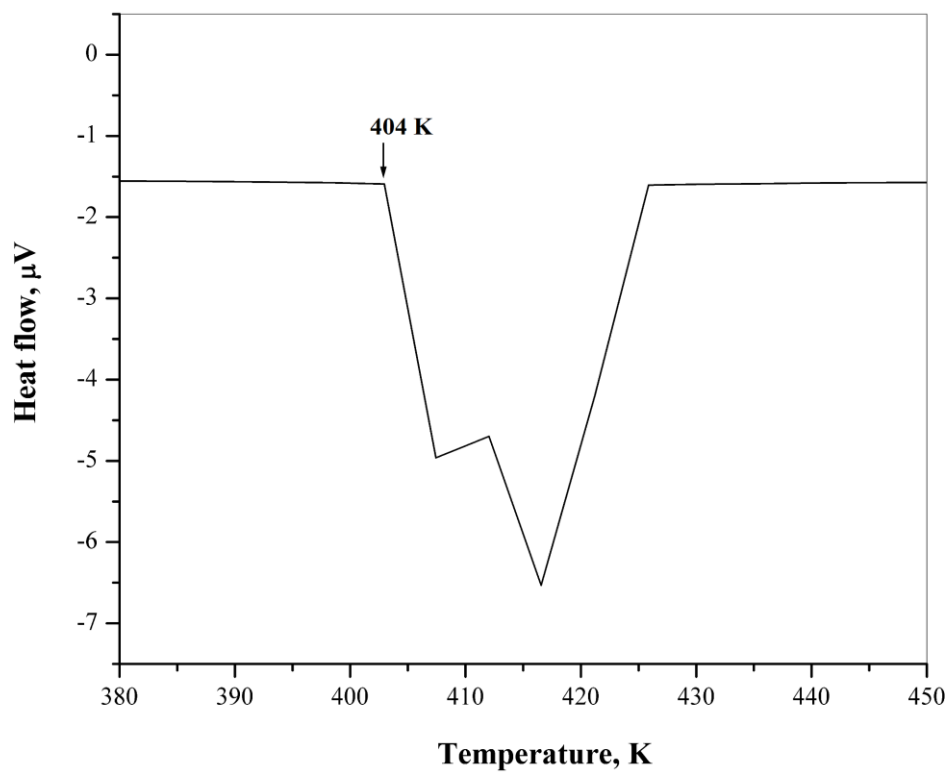


Fig. 3.9 DSC pattern of  $\text{AgI}_{0.95}\text{Cl}_{0.05}$

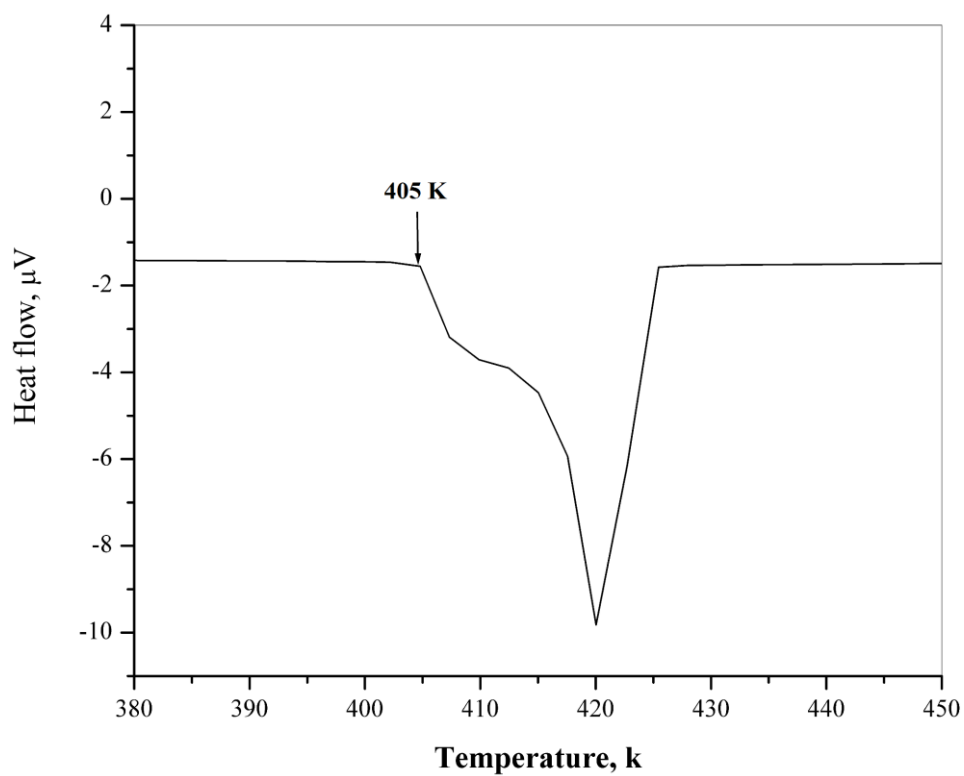


Fig. 3.10 DSC pattern of  $\text{AgI}_{0.94}\text{Cl}_{0.06}$

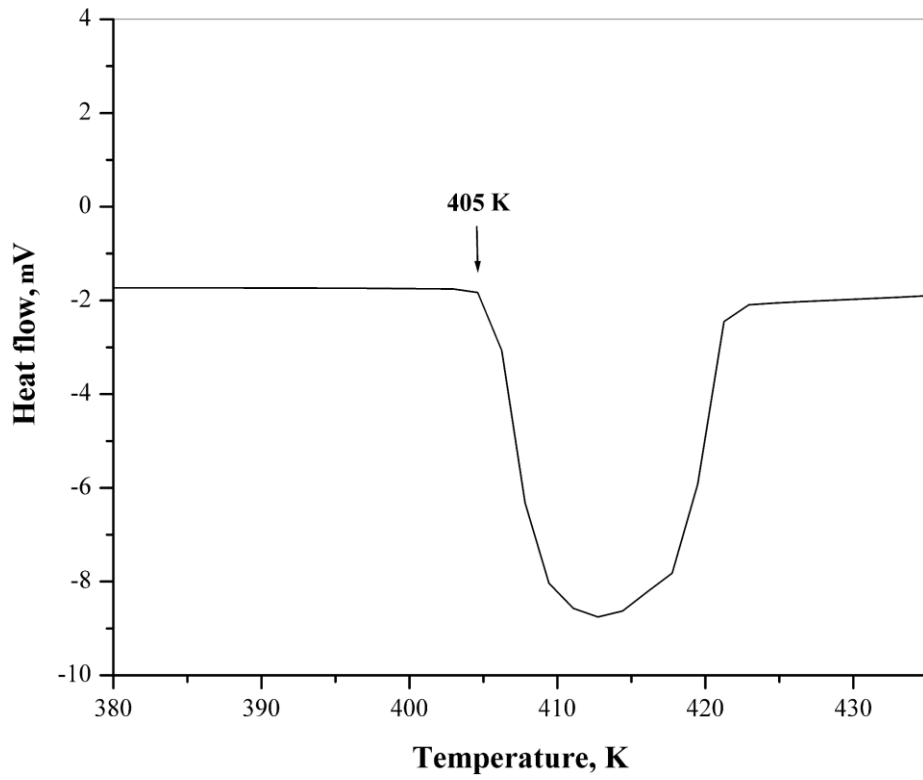


Fig. 3.11 DSC pattern of  $\text{AgI}_{0.9}\text{Cl}_{0.1}$

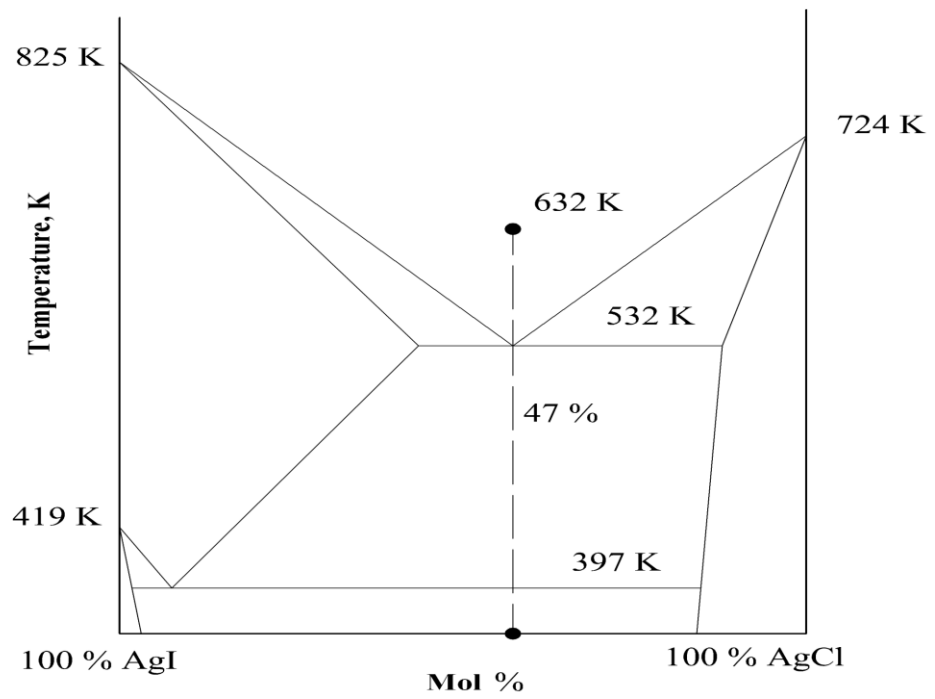


Fig. 3.12 Phase diagram of AgI-AgCl composition with temperature [4]

The plot of onset of  $\beta$  to  $\alpha$  transition temperature with respect to the concentration of  $\text{Cl}^-$  in  $\text{AgI}_{1-x}\text{Cl}_x$  is shown in Fig. 3.13. The gradation in the onset phase transition temperature is reflected with increase in the concentration of  $\text{AgCl}$  in  $\text{AgI}$ . Beyond the solubility limit, the DSC results show no change in the  $\beta$  to  $\alpha$  transition temperature, which again confirm the solubility of  $\text{AgCl}$  in  $\text{AgI}$  to be around 5 mol%.

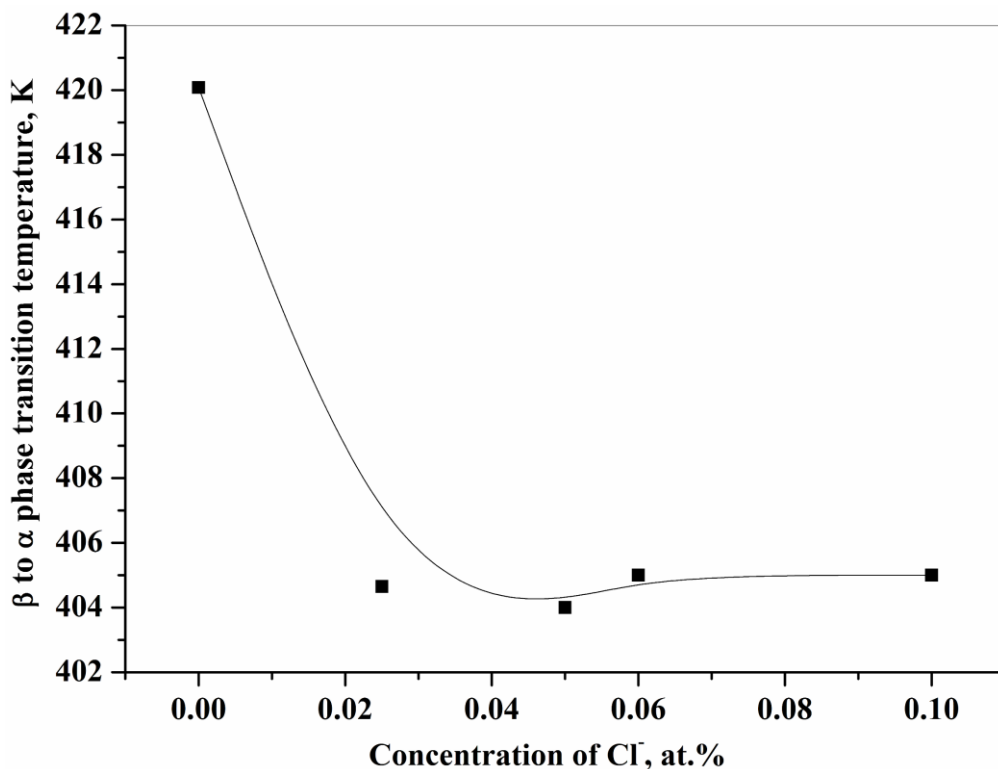


Fig. 3.13 Plot of  $\beta$ - $\text{AgI}$  to  $\alpha$ - $\text{AgI}$  phase transition temperature vs concentration of  $\text{Cl}^-$  in  $\text{AgI}$  from DSC measurements

### 3.6 SOLUBILITY LIMIT ESTIMATION USING AAS AND XPS TECHNIQUES

#### 3.6.1 Solubility studies using Atomic Absorption Spectrometer (AAS)

The solubility of  $\text{AgI}$  in ammonia solution is dependent on the pH of the solution and hence, an optimum pH should be used to study the dissolution of  $\text{AgCl}$  added  $\text{AgI}$  in ammonia. For the same reason, different concentration of ammonia (26.76 M, 17.84 M, 5.32 M and 2.67 M) were used to optimise the solubility of  $\text{AgI}$ . The estimated  $\text{Ag}^+$  ion concentration for  $\text{AgI}$  towards different concentrations of ammonia is shown in Table 3.4.

The ammonia concentration for dissolving AgCl was optimised as 17.84 M for analysis. Even though variation with different concentration of ammonia was little, a better consistency was observed when the concentration of ammonia was around 17.84 M which was taken as the optimised concentration for dissolution of AgCl.

**Table 3.4 Concentration of Ag<sup>+</sup> ions in AgI using AAS**

| Sl.No: | Concentration of ammonia (M) | Ag <sup>+</sup> concentration (µg/ml) |
|--------|------------------------------|---------------------------------------|
| 1.     | 26.76                        | 4.0                                   |
| 2.     | 17.84                        | 4.8                                   |
| 3.     | 5.32                         | 4.2                                   |
| 4.     | 2.67                         | 4.6                                   |

The results of the Ag<sup>+</sup> estimation on the samples of AgI<sub>0.975</sub>Cl<sub>0.025</sub> are shown in Table 3.5. From the table, as-prepared samples contain the maximum insoluble AgCl, which is 56.56 % of the theoretically calculated Ag<sup>+</sup> ion concentration as AgCl in AgI<sub>0.975</sub>Cl<sub>0.025</sub>. Hence, 43.4 % of AgCl has dissolved in AgI even before heating the sample.

**Table 3.5 Concentration of Ag<sup>+</sup> ions leached from the AgI<sub>1-x</sub>Cl<sub>x</sub> matrix**

| Sl. No. | Sample composition                       | Sample condition | Concentration of Ag <sup>+</sup> as AgCl in AgI <sub>1-x</sub> Cl <sub>x</sub> solid (theoretical) (mmol) | Concentration of Ag <sup>+</sup> (mmol) |
|---------|--|------------------|---|---|
| 1.      | AgI <sub>0.975</sub> Cl <sub>0.025</sub> | as-prepared      | 0.23  | 0.13                                    |
| 2.      | AgI <sub>0.975</sub> Cl <sub>0.025</sub> | heated           | 0.23  | 0.02                                    |
| 3.      | AgI <sub>0.95</sub> Cl <sub>0.05</sub>   | as-prepared      | 0.46  | 0.27                                    |
| 4.      | AgI <sub>0.95</sub> Cl <sub>0.05</sub>   | heated           | 0.46  | 0.11                                    |

This shows that after heating the sample AgI<sub>0.975</sub>Cl<sub>0.025</sub>, 91 % of the Ag<sup>+</sup> ions with respect to the theoretical value of AgI<sub>0.975</sub>Cl<sub>0.025</sub> have dissolved into AgI matrix. This shows the formation of the solid solution is envisaged for composition < 5 mol % of AgCl in AgI.

An error of ( $\pm$ )10 % is observed in this analysis. Around 41.3 % of the  $\text{Ag}^+$  ion has dissolved in the AgI matrix for the composition  $\text{AgI}_{0.95}\text{Cl}_{0.05}$ . This is in correlation with the as-prepared  $\text{AgI}_{0.975}\text{Cl}_{0.025}$  sample. Similarly, after heating,  $\text{AgI}_{0.95}\text{Cl}_{0.05}$ , 76.08 % of the theoretical value has dissolved in AgI matrix. From XRD results, the solubility limit of AgCl in AgI was  $x \geq 0.05$  in  $\text{AgI}_{1-x}\text{Cl}_x$ . Thus, the excess 14.92 % leaching into ammonia solution from  $\text{AgI}_{0.95}\text{Cl}_{0.05}$  when compared to  $\text{AgI}_{0.975}\text{Cl}_{0.025}$ , could be due to the insoluble AgCl in the heated samples.

### 3.6.2 Elucidation of AgCl solubility in AgI by using X-ray photoelectron spectroscopy

As the concentration of chlorine in  $\text{AgI}_{0.975}\text{Cl}_{0.025}$  was below the detection limit of the instrument, the effect of the addition of  $\text{Cl}^-$  in Ag 3d and I 3d patterns were unseen for as-prepared samples and heated samples. Therefore, only the XPS patterns of  $\text{AgI}_{0.95}\text{Cl}_{0.05}$  are discussed. From the Cl 2p patterns observed in Fig. 3.14, the major peak of  $\text{Cl}^-$  corresponds to the one which has formed the solid solution with AgI at 198.8 and

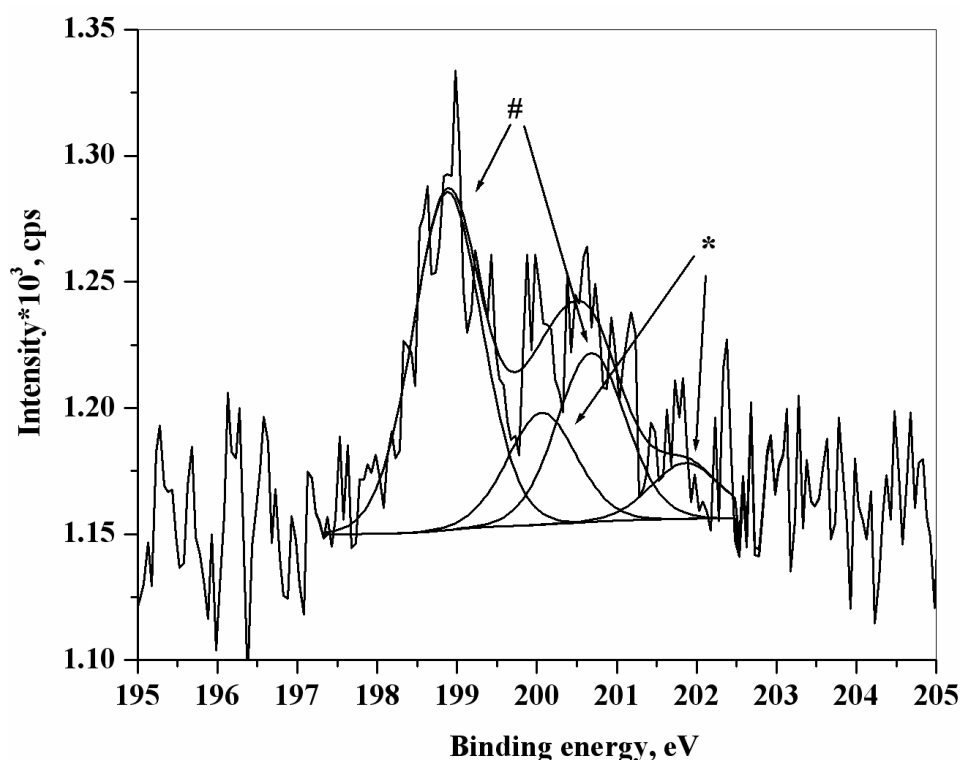
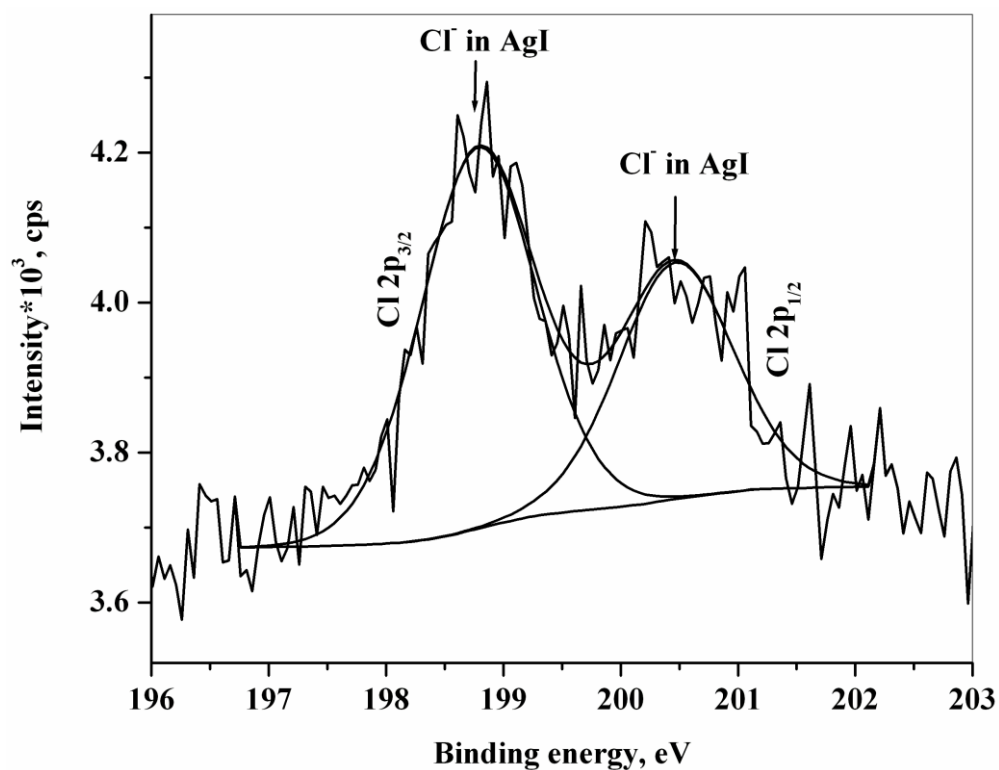


Fig. 3.14 XPS patterns of Cl 2p of  $\text{AgI}_{0.95}\text{Cl}_{0.05}$  as-prepared sample. # represent the insoluble AgCl and \* represents  $\text{Cl}^-$  in AgI



**Fig. 3.15 XPS patterns of Cl 2p of  $\text{AgI}_{0.95}\text{Cl}_{0.05}$  sample after heating at 473 K and washing with ammonia**

200.6 eV. It is also observed that the as-prepared samples have additional peaks at 200.0 and 201.8 eV, which corresponds to the  $\text{Cl}^-$  adjacent to  $\text{Ag}^+$  and this could be due to the presence of AgCl in the sample as an insoluble entity. All the curve fitted peaks have a FWHM of  $\sim 1$  eV. In Fig. 3.15, for heated  $\text{AgI}_{0.95}\text{Cl}_{0.05}$ , the peaks at 198.8 eV and 200.6 eV correspond to the  $2p_{3/2}$  and  $2p_{1/2}$  of  $\text{Cl}^-$  in the vicinity of  $\text{Ag}^+$  as a solid solution [11].

Ag 3d and I 3d patterns of  $\text{AgI}_{0.95}\text{Cl}_{0.05}$  are shown in Fig. 3.16 and 3.17. For as-prepared  $\text{AgI}_{0.95}\text{Cl}_{0.05}$ , the binding energies of the major Ag 3d peak is around 369.4 eV for Ag  $3d_{5/2}$  which corresponds to the binding energy of Ag 3d in AgI [12]. With a difference of 6.0 eV from the  $3d_{5/2}$  peak, the Ag  $3d_{3/2}$  peak was observed at 375.4 eV as shown in Fig. 3.16 (a). For samples heated to 473 K, there were additional peaks at higher binding energies of 370.7 and 376.6 eV which is 1.2 eV far from the major Ag 3d (which arises from Ag 3d close to  $\Gamma$ ) {Fig. 3.16 (b)}. As reported in the literature,  $\text{Ag}^+$  close to  $\text{Cl}^-$  will have up to 2 eV more binding energies than  $\text{Ag}^+$  close to  $\Gamma$  [13]. Similarly, the I 3d

pattern observed for  $\text{AgI}_{0.95}\text{Cl}_{0.05}$  also shows the major peaks of I  $3d_{5/2}$  and I  $3d_{3/2}$  at 620.5 and 631.9 eV {Fig. 3.17 (a)}. The change in the chemical environment due to the presence of  $\text{Cl}^-$  is seen in two new peaks at 618.1 and 630.0 eV which are  $\sim 1.7$  eV away from the major peaks of I $^-$  corresponding to I  $3d_{5/2}$  and I  $3d_{1/2}$  {Fig. 3.17 (b)}. It was inferred from AAS studies that the solubility limit for AgCl in AgI is  $x \leq 0.05$  in  $\text{AgI}_{1-x}\text{Cl}_x$ . Also, the formation of solid solution even in the as-prepared samples from AAS studies proves that around 41 % of AgCl dissolves in AgI. XPS corroborates the results of AAS, as the Cl 2p peak of  $\text{AgI}_{0.95}\text{Cl}_{0.05}$  shows more intense insoluble AgCl peak which is distinct from the Cl 2p corresponding to the soluble  $\text{Cl}^-$  in AgI (Fig. 3.15). The insoluble  $\text{Cl}^-$  peaks are removed after washing with ammonia (Fig. 3.15). Similar observations were seen in the results pertaining to the  $\text{Ag}^+$  ion concentration obtained from AAS results. Therefore, the result from both AAS and XPS concludes the formation of the solid solution even for the as-prepared sample and also on the solubility of AgCl in AgI. The summary of binding energies of the XPS analysis is presented in Table 3.6

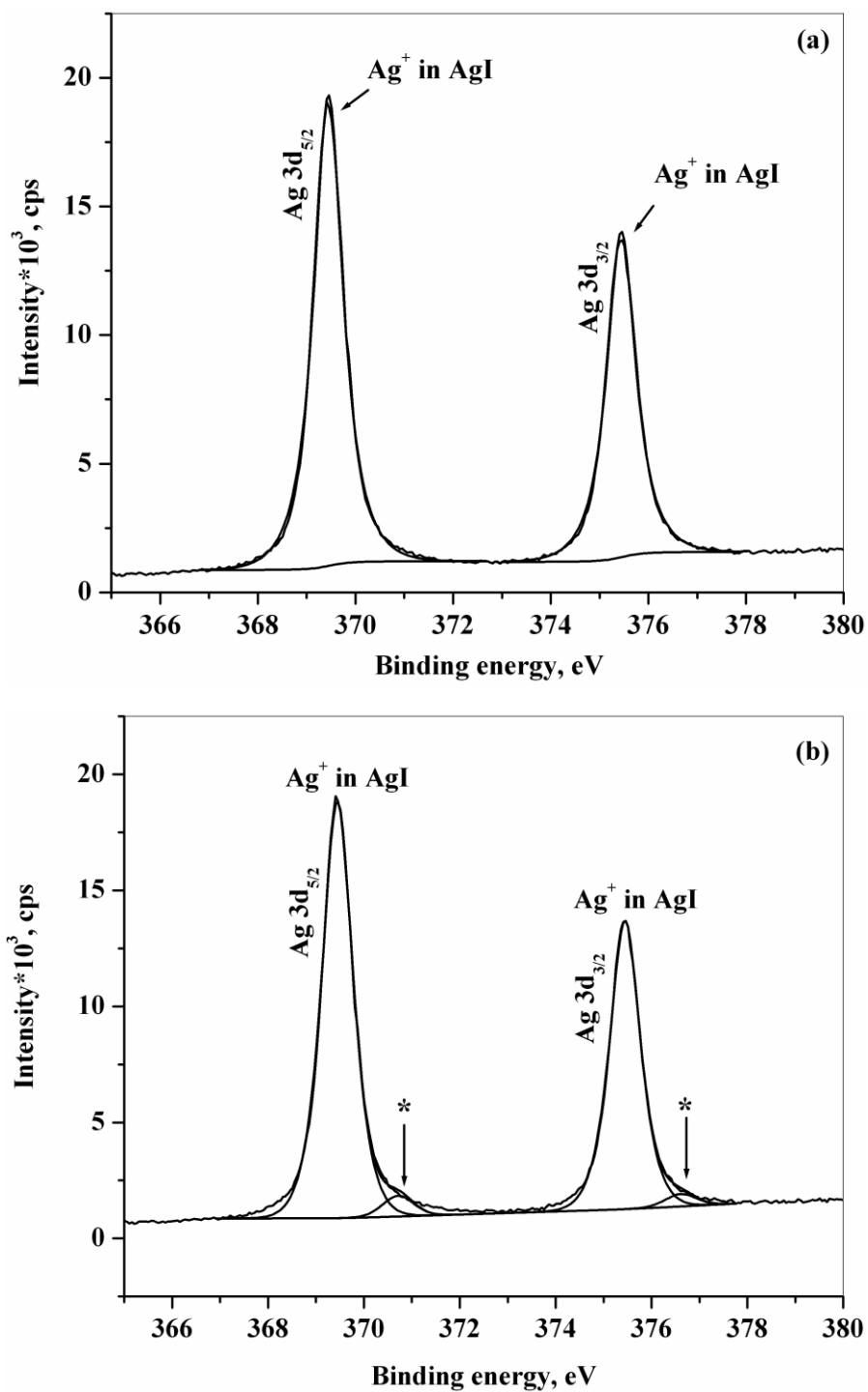
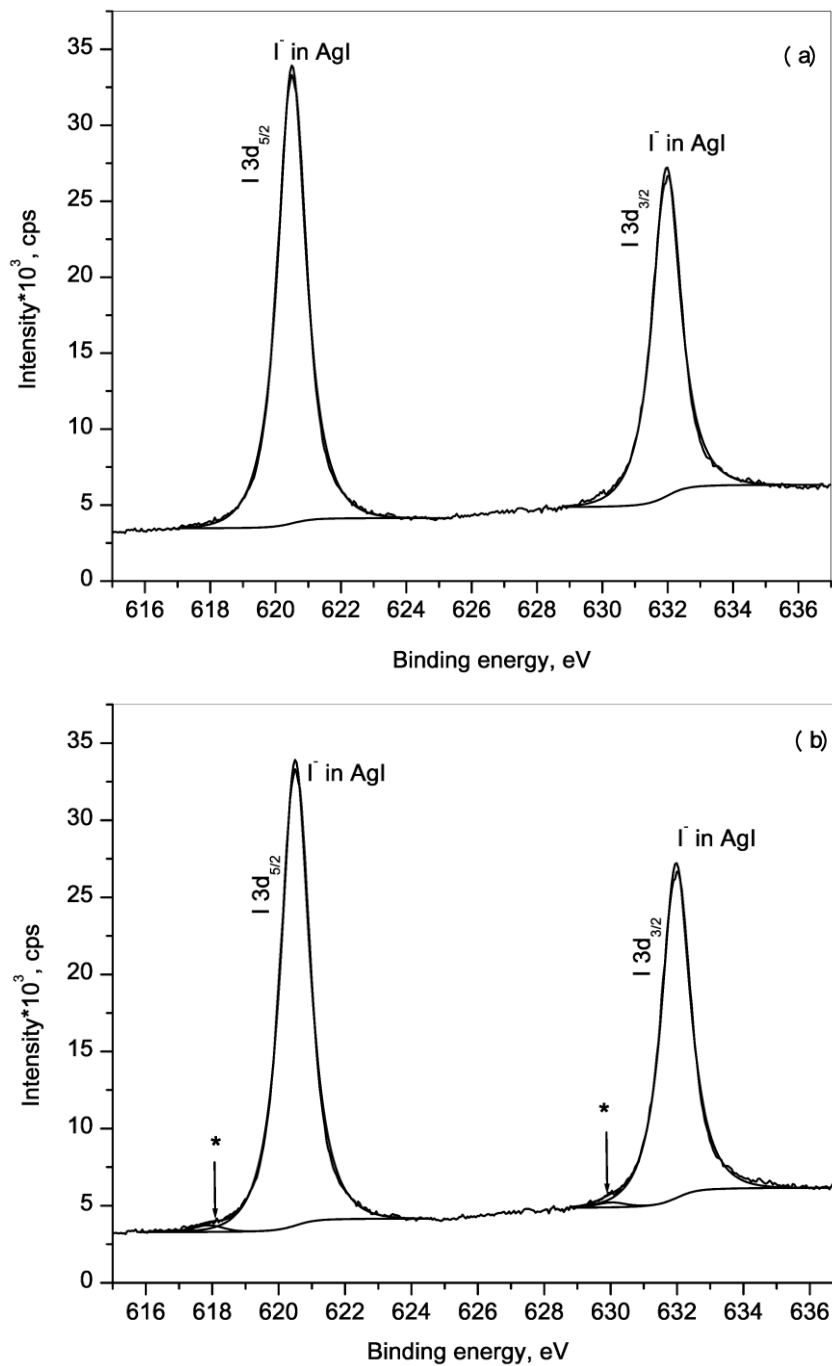


Fig. 3.16 XPS patterns of Ag 3d of  $\text{AgI}_{0.95}\text{Cl}_{0.05}$  ammonia washed (a) as-prepared sample and (b) heated to 473 K. \* represents the change in the chemical environment due to the substitution of  $\text{Cl}^-$  ion



**Fig. 3.17** XPS patterns of I 3d of  $\text{AgI}_{0.95}\text{Cl}_{0.05}$  ammonia washed (a) as-prepared sample and (b) heated to 473 K. \* represents the change in the chemical environment due to the substitution of  $\text{Cl}^-$  ion

Table 3.6 Summary of binding energies of Cl 2p, I 3d and Ag 3d

| Element          | Cl 2p             |                   |                   |                   | Ag 3d             |                   |                   |                   | I 3d              |                   |                   |                   |
|------------------|-------------------|-------------------|-------------------|-------------------|-------------------|-------------------|-------------------|-------------------|-------------------|-------------------|-------------------|-------------------|
| Sample           | as-prepared       |                   | heated            |                   | as-prepared       |                   | heated            |                   | as-prepared       |                   | heated            |                   |
| Orbital          | 2p <sub>3/2</sub> | 2p <sub>1/2</sub> | 2p <sub>3/2</sub> | 2p <sub>1/2</sub> | 3d <sub>5/2</sub> | 3d <sub>3/2</sub> |
| Major peaks      | 198.8             | 200.6             | 198.8             | 200.4             | 369.4             | 375.4             | 369.4             | 375.4             | 620.5             | 631.9             | 620.5             | 631.9             |
| Additional peaks | 200.0             | 201.8             | -                 |                   | -                 |                   | 370.7             | 376.6             | -                 |                   | 618.1             | 630.0             |

### 3.7 STUDIES RELATED TO IONIC CONDUCTION AND BULK ELECTRICAL CONDUCTIVITY

#### 3.7.1 Transport number measurement studies

Generally, high ionic conduction is a prerequisite for solid electrolytes that are employed in potentiometric sensors. Thus, it is essential to quantify the percentage of ionic transference in such materials. The ionic transference numbers were measured for  $\text{AgI}_{1-x}\text{Cl}_x$  using a perturbation potential of 0.5 V. Initially, at time  $t=0$ , the current measured after the application of a DC potential of 0.5 V is due to both ionic and electronic conduction. In  $\text{AgI}_{1-x}\text{Cl}_x$  compounds, the ionic conduction is due to the  $\text{Ag}^+$  ions. After a fixed duration of time, the ionic movement ceases. Once the ionic movement ceases after around 7 min of application of the potential, electronic movement will give rise to the current. Typical plots of current vs. time are given in Fig. 3.18 (a) and (b). The inset shows the enlarged version of the decrease of initial current with time. The figure shows the typical behavior of a solid electrolyte under the application of a DC potential. Initial current, mainly the sum of ionic and electronic is very high. Eventually the current falls to constant value, where only electronic current persists. The rates of decrease in the current with time are  $\sim 1.19 \times 10^{-4} \text{ A}\cdot\text{s}^{-1}$  and  $2.07 \times 10^{-4} \text{ A}\cdot\text{s}^{-1}$  for AgI at 298 and 423 K respectively when the region corresponding to ionic movement is fitted to a linear plot. This result again correlates to the increased ionic transport number due to the phase

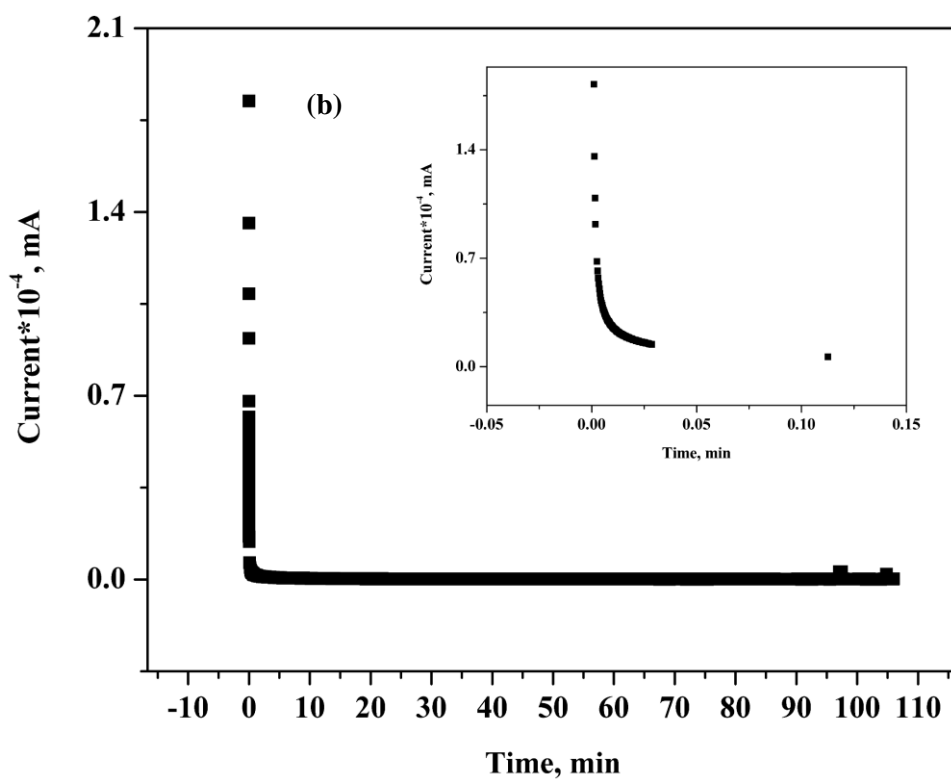
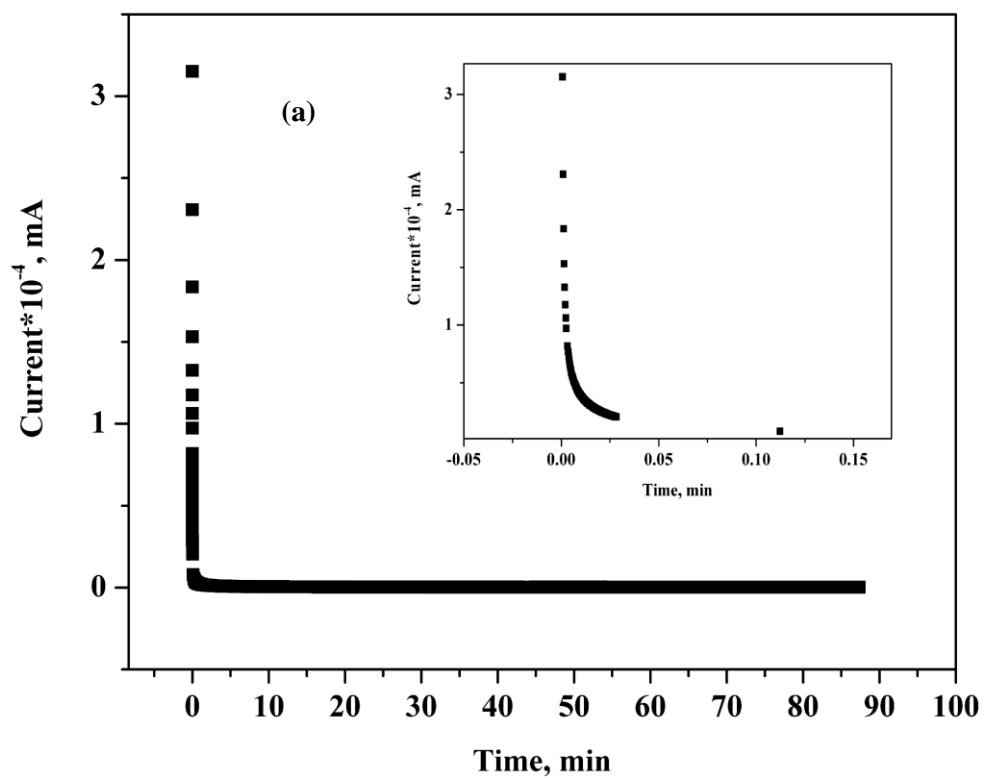


Fig. 3.18 Typical plot of current vs. time for AgI at (a) 298 and (b) 423 K with a DC potential of 0.5 V. The inset shows the enlarged plot of the initial current.

transition of AgI into highly conducting  $\alpha$ -phase. The measured ionic transference number for  $\text{AgI}_{1-x}\text{Cl}_x$  is given in Table 3.7.

**Table 3.7 Measured ionic transference number in percentage for  $\text{AgI}_{1-x}\text{Cl}_x$  at different temperatures**

| Sample                                | Transference number<br>% |       |       |       |
|---------------------------------------|--------------------------|-------|-------|-------|
|                                       | 298 K                    | 373 K | 423 K | 473 K |
| AgI                                   | 99.32                    | 99.89 | 99.89 | 99.88 |
| $\text{AgI}_{0.975}\text{Cl}_{0.025}$ | 99.25                    | 99.89 | 99.89 | 99.89 |
| $\text{AgI}_{0.95}\text{Cl}_{0.05}$   | 99.36                    | 99.81 | 99.82 | 99.82 |
| $\text{AgI}_{0.9}\text{Cl}_{0.1}$     | 99.20                    | 99.72 | 99.79 | 99.86 |

The ionic transference was calculated using the equation:

$$t_{\text{ion}} = \frac{i_{\text{initial}} - i_{\text{final}}}{i_{\text{initial}}} \quad (3.18)$$

where  $t_{\text{ion}}$  is the ionic transference number,  $i_{\text{initial}}$  is the initial current which was calculated by fitting a line to the first five experimentally observed values and taking the y-intercept as the  $i_{\text{initial}}$ . In the above equation,  $i_{\text{final}}$  is the final current obtained by taking the average values of current in the constant current region once the ionic migration ceases.

At room temperature,  $\beta$ -phase is poorly conducting compared to  $\alpha$ -phase which is formed after  $\sim 423$  K. Thus, the transference number before the transition temperature was lower compared to that in the highly conducting  $\alpha$ -phase. Also, after the solubility limit of  $\text{AgI}_{0.95}\text{Cl}_{0.05}$ , the  $t_{\text{ion}}$  was found to reduce probably due to the precipitation of AgCl in the matrix.

Transport measurements carried out on compositions of  $\text{AgI}_{1-x}\text{Cl}_x$  ( $x=0-0.06$ ) show transference number for ionic conduction from 99.2% to 99.89 % from room temperature to 473 K. At room temperature, the  $\beta$ -AgI phase is the major contribution for the ionic transference number. As the temperature increases and reaches the  $\beta$ -AgI to  $\alpha$ -AgI transition, the ionic transference number increases to 99.8 %. For other compositions of  $\text{AgI}_{1-x}\text{Cl}_x$  ( $x=0.025-0.06$ ) similar trend in the transference number was observed. This

shows that the number of ionic charges available for conduction paths does not change much with the incorporation of AgCl in AgI above 423 K.

### **3.7.2 Electrical conductivity studies**

Electrical conductivity values of a solid electrolyte are essential for understanding the optimum temperature and compositions which has highest conductivity values. This in turn is useful in potentiometric sensing studies based on the solid electrolytes. The conductivity studies were carried out in the temperature range of 298 K to 523 K for the compositions of  $\text{AgI}_{1-x}\text{Cl}_x$  ( $x=0-0.06$ ). Typical Nyquist plots for AgI using a perturbation potential of 0.15 V at different temperatures are given in Fig. 3.19 (a-f).

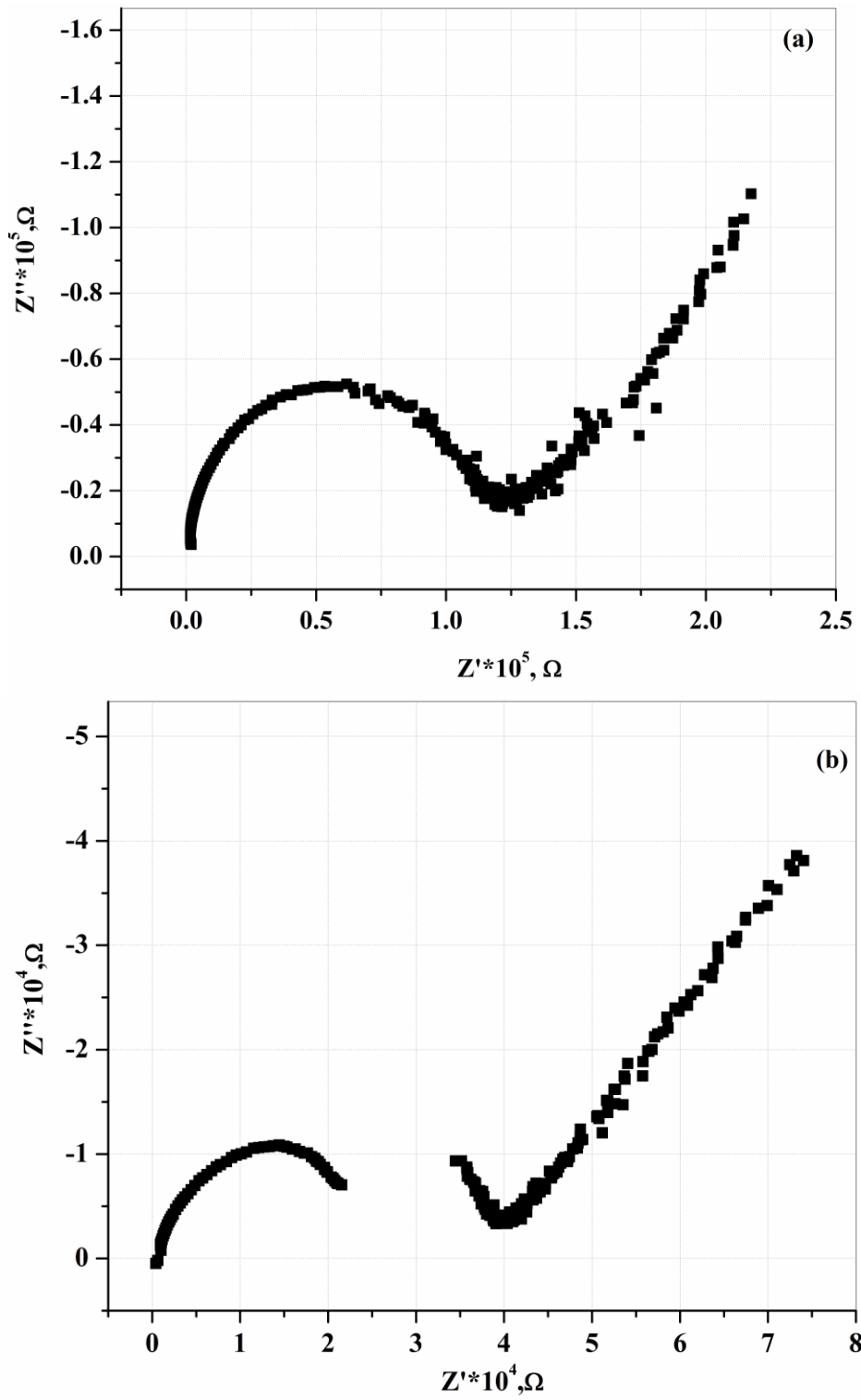


Fig. 3.19 Typical Nyquist plots for AgI at temperatures (a) 298 K and (b) 373 K

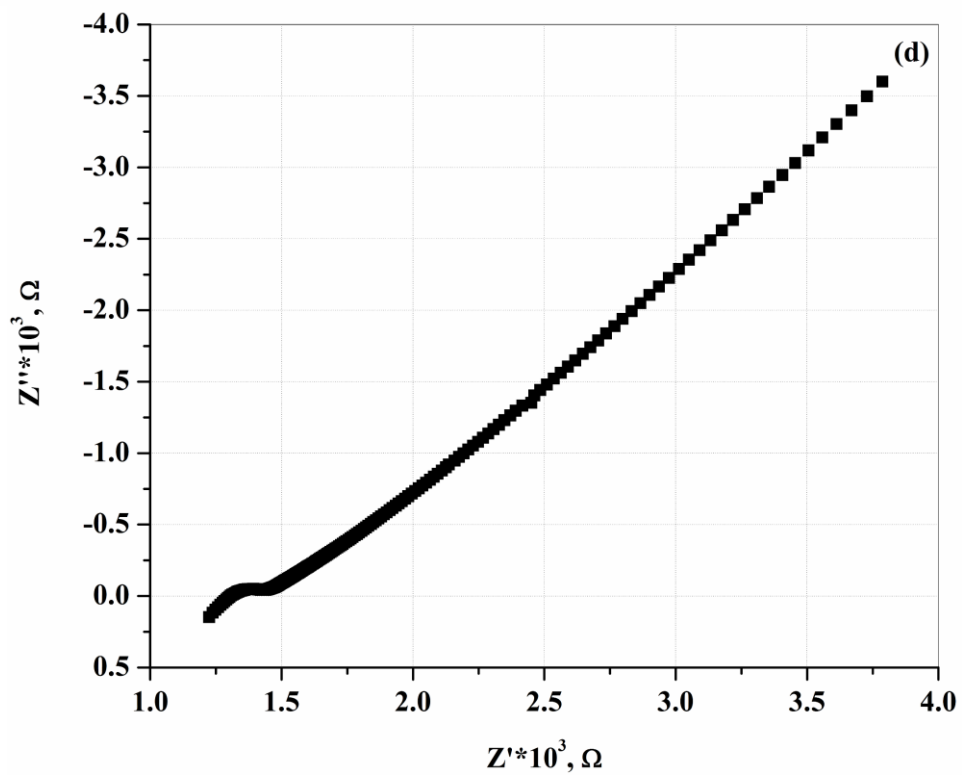
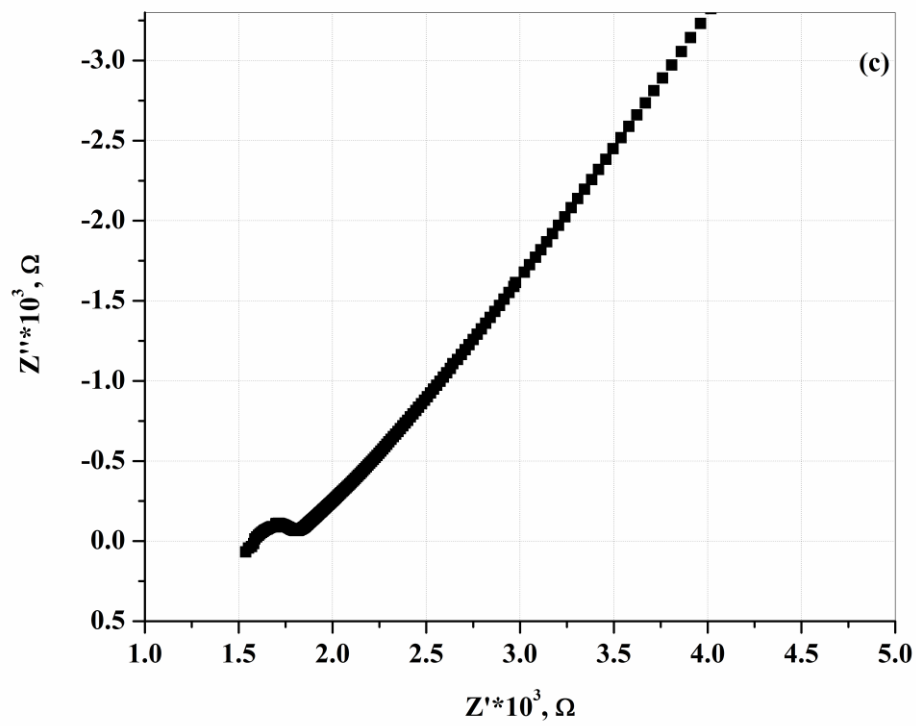


Fig. 3.19 Typical Nyquist plots for AgI at temperatures (c) 408 K and (d) 413 K

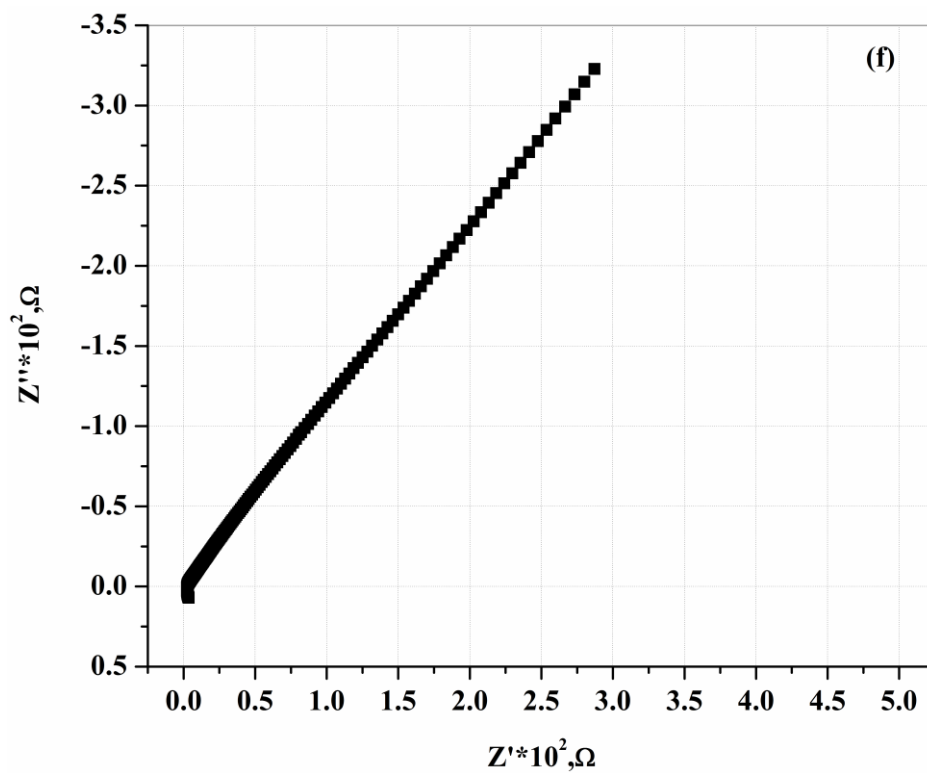
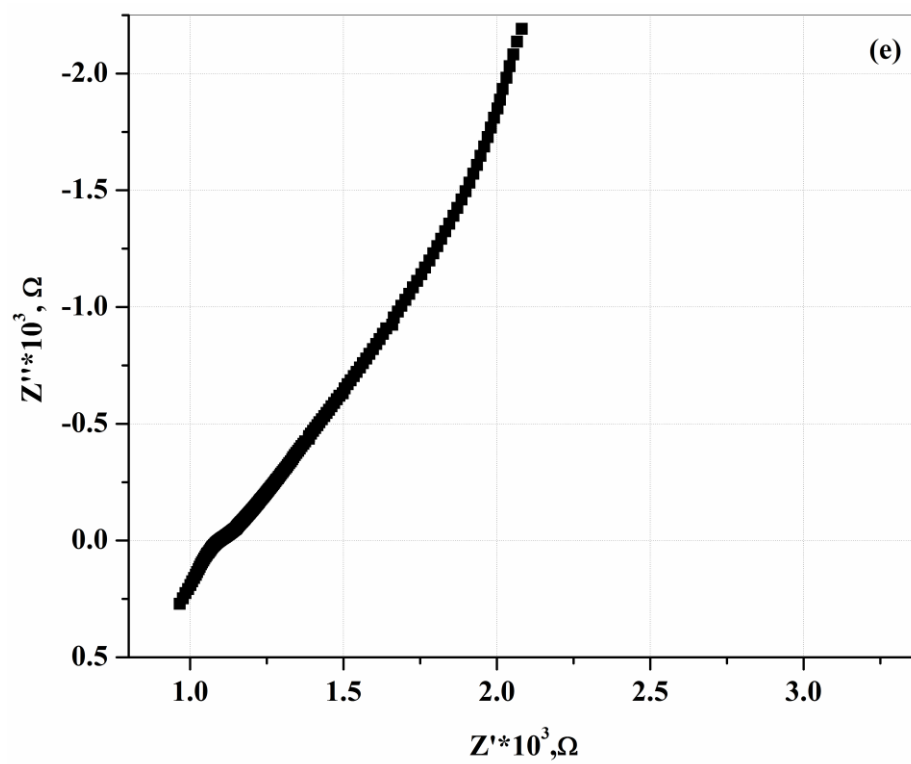
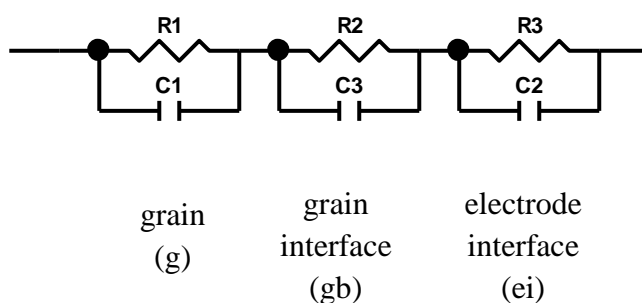


Fig. 3.19 Typical Nyquist plots for AgI at temperatures (e) 417 K and (f) 473 K

Resolving the bulk resistance of a material from the grain boundary resistance, demands for the use of appropriate equivalent circuits to fit the experimentally obtained Nyquist plot. Ceramic solid electrolyte based on YSZ was fitted in the admittance plane using circuit proposed by Bauerle (Bauerle equivalent circuit) [14]. The circuit was then routinely used to understand the bulk and grain boundary resistance and also the electrode interfaces. Typical Bauerle equivalent circuit is shown in Fig. 3.20



**Fig. 3.20 Bauerle equivalent circuit**

The circuit elements of grain (g), grain boundary (gb) and electrode interface (ei) are connected in series. Here R1, R2, R3 and C1, C3, C2 represents the resistance and capacitance of the grain, grain boundary and the electrode interfaces respectively.

Similarly, for the compositions of  $\text{AgI}_{1-x}\text{Cl}_x$ , the equivalent circuit used for resolving the bulk resistance is shown in the Fig. 3.21. In the figure the circuit “R1 and C1” represents the bulk (grain) of the material. The fitting was complete only with the usage of an inductor element (L1). As there is a possibility of inductance in the high frequency region from the electrode leads. But, the instrument was short periodically using the calibration standard. Also, the inductor characteristics were not observed at room temperature for all the compositions. Therefore, the only possibility could be due to the presence of an air gap between the electrode-electrolyte interfaces causing the Nyquist plot to be in the fourth quadrant at high frequency.

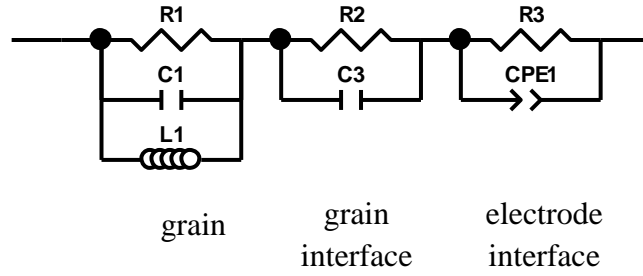


**Fig. 3.21** Equivalent circuit used for fitting  $\text{AgI}_{1-x}\text{Cl}_x$

Here  $R_1$ ,  $R_2$  and  $R_3$  represent the resistance of the grain (bulk), grain boundary and electrode interface.  $C_1$  and  $C_2$  represent the grain and the grain boundary capacitance.

The constant phase element  $\left(\frac{1}{(j*\omega)^n*Q_1}\right)$ , where  $j$  is the imaginary unit,  $\omega$  is the angular frequency and  $Q_1$  is a parameter to represent the CPE. When the exponent  $n$  is zero, the electrode interface behaves as a resistor, when  $n$  is one, the constant phase element behaves as a pure capacitor which in turn will treat the electrode interface as a parallel resistor and capacitor. A CPE (constant phase element) was used to fit the electrode-electrolyte interface with varying orders of  $n$  for  $\text{AgI}_{1-x}\text{Cl}_x$ .

The bulk resistance was calculated for  $\text{AgI}$  at different temperatures. The bulk conductivity was then calculated as explained in the experimental section using the formula given in equation (3.4).

$$R_1 = \rho \frac{l}{A} \quad (3.4)$$

where  $\rho$  is the resistivity,  $l$  is the thickness of the pellet used and  $A$  is the surface area of the pellet packed by the electrode and  $R_1$  is the bulk resistance. The plot of conductivity (calculated from the resistivity value) and the temperature known as the Arrhenius plot shows the transition of the phases from  $\beta$  to  $\alpha$  as a huge jump in the conductivity as  $\alpha$ -cubic phase is the highly conducting phase.

Conductivity studies on the compositions of  $\text{AgI}_{1-x}\text{Cl}_x$  ( $x= 0-0.06$ ) show typical behavior of  $\text{AgI}$  conductor with a sudden jump of conductivity during  $\beta$ - $\text{AgI}$  to  $\alpha$ - $\text{AgI}$  transition

temperature around 423 K. Fig. 3.22 shows the Arrhenius plot obtained for the compositions of  $\text{AgI}_{1-x}\text{Cl}_x$  ( $x = 0, 0.025, 0.05$  and  $0.06$ ). Below  $\sim 423$  K, the  $\beta$ -phase shows an increase in the conductivity with temperature due to Frenkel defects arising because of difference in the crystal structure of AgCl and AgI. The transition ( $\beta$  to  $\alpha$ ) temperature of AgI decreases with increase in  $\text{Cl}^-$  concentration in AgI. The deduced transition temperature for  $\text{AgI}_{1-x}\text{Cl}_x$  ( $x=0-0.06$ ) is given in Table 3.8. The introduction of the new phase of AgCl above the composition of  $x \geq 0.05$  in  $\text{AgI}_{1-x}\text{Cl}_x$ , as discussed in XRD, leads to decrease in the number of  $\text{Ag}^+$  ions paths for effective conduction. Thus, the conductivity decreases due to the precipitation of AgCl as a separate phase, beyond the solubility limit. After  $\alpha$  phase formation, the conductivity values for all the compositions of  $\text{AgI}_{1-x}\text{Cl}_x$  were found to be the same, irrespective of the concentration of AgCl present within the solubility limit.

The  $\beta$  to  $\alpha$  transition temperature from DSC measurements carried on the composition  $\text{AgI}_{1-x}\text{Cl}_x$  ( $x=0-0.1$ ) show the same trend in

phase transition temperatures obtained from conductivity measurements. Thus, it confirms the solubility limit of AgCl in AgI is less than 5 mol%. The transport measurements also correlates the results from electrical conductivity measurements at 423 K where  $\alpha$ -AgI phase for all the compositions studied were found to have nearly the same conductivity values.

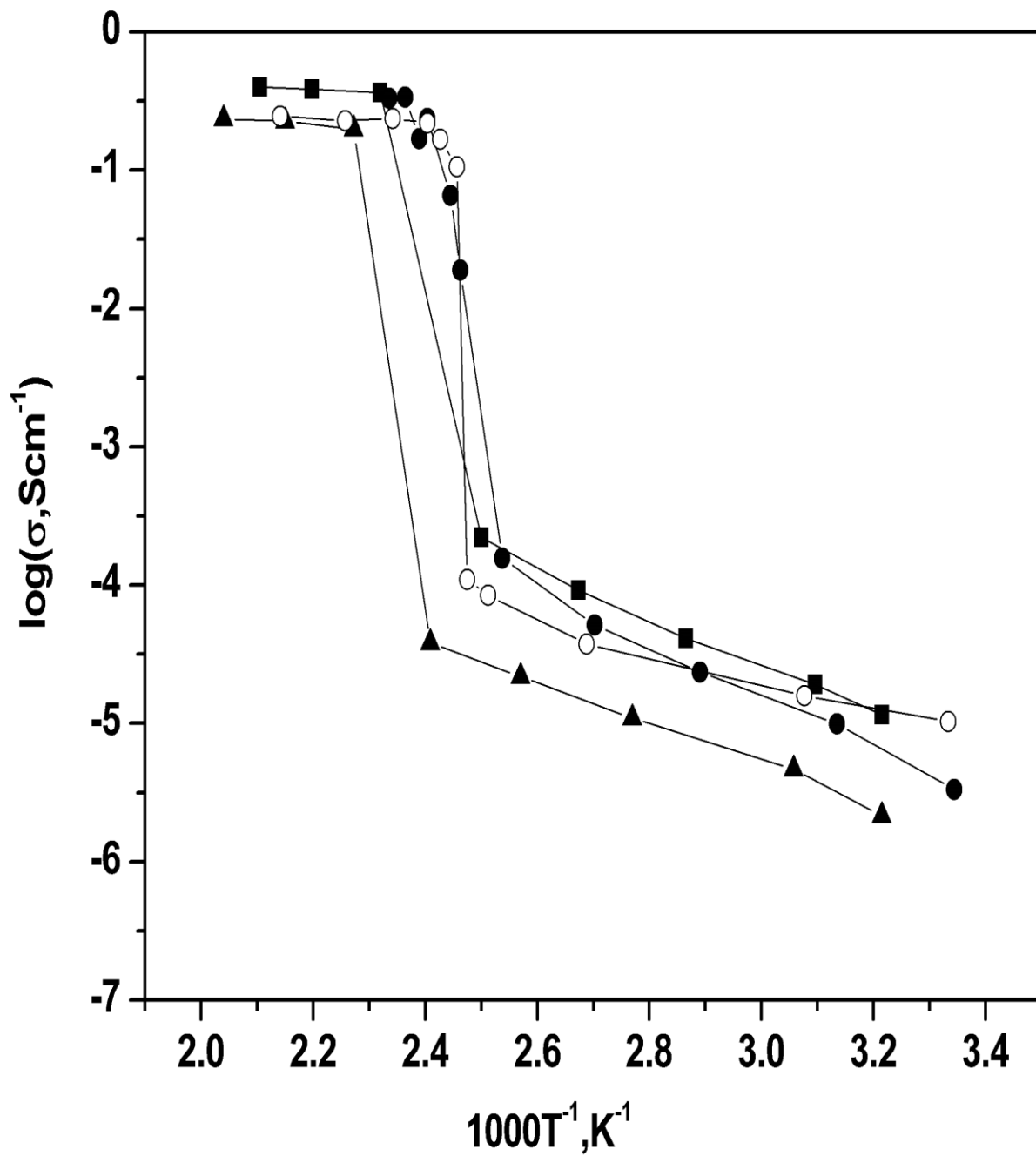


Fig. 3.22 Arrhenius plots of  $\text{AgI}_{1-x}\text{Cl}_x$  with  $x$  as ( $\blacktriangle$ ) 0, ( $\bullet$ ) 0.025, ( $\blacksquare$ ) 0.05 and ( $\circ$ ) 0.06

**Table 3.8  $\beta$ -AgI to  $\alpha$ -AgI phase transition temperature for  $\text{AgI}_{1-x}\text{Cl}_x$  ( $x = 0-0.06$ ) from conductivity measurements**

| $\text{AgI}_{1-x}\text{Cl}_x$<br>x is | $\beta$ to $\alpha$ phase transition<br>temperature, K |
|---------------------------------------|--|
| 0                                     | 416  |
| 0.025                                 | 394  |
| 0.05                                  | 398  |
| 0.06                                  | 404  |

### 3.8 CONCLUSION

The characterisation of  $\text{AgI}_{1-x}\text{Cl}_x$  ( $x=0-0.25$ ) synthesized by co-precipitation method using various facilities like XRD, SEM, DSC, electrical conductivity, ionic transference number measurement, XPS and AAS are dealt in this chapter. The onset temperature for  $\beta$  to  $\alpha$  phase transition in AgI with the addition of AgCl measured using DSC and bulk electrical conductivity studies shows decrease in the onset temperature pertaining to  $\beta$  to  $\alpha$  transition in AgI. The investigations were further supported by the study of the morphology using SEM and percentage ionic character using ionic transport measurements. The solubility limit of AgCl in AgI studies using AAS and XPS facilities confirms the preferential leaching of the precipitated AgCl in  $\text{AgI}_{1-x}\text{Cl}_x$  composition beyond its solubility limit. The chemical environment change occurring to Ag and I ions in  $\text{AgI}_{1-x}\text{Cl}_x$  from XPS studies confirms the precipitation of AgCl. All these characterisation studies revealed that the solubility limit of AgCl is <5 mol % in AgI. These characterisation studies were important in predicting the usefulness of appropriate composition to be employed in sensing studies and related mechanism to be discussed in subsequent chapters.

### 3.9 REFERENCES

1. Powder diffraction file, 2015, Alphabetic indexes inorganic phases, The International Centre for Diffraction Data
2. R. Makiura, T. Yonemura, T. Yamada, M. Yamauchi, R. Ikeda, H. Kitagawa, K. Kato and M. Takata, 2009, Size controlled stabilization of the superionic phase to room temperature in polymer coated AgI nanoparticles, *Nature Materials*, 8, 476-480
3. S. Ihara, Y. Warita and K. Suzuki, 1984, Ionic conductivity in  $\text{AgI}_{1-x}\text{Cl}_x$ , *Physica Status Solidi A*, 86, 729-734
4. J. Sloan, A.I. Kirkland, J.L. Hutchinson and M.L.H. Green, 2002, Integral atomic layer architectures of 1D crystals inserted into single walled carbon nanotubes, *Royal Society of Chemistry, Chemical Communications*, 0, 1319-1332
5. B.D. Cullity, 1956, *Elements of X-ray diffraction*, Addison Wesley Publishing Company, Inc., 509 pp
6. S. Geller, 1977, *Solid electrolytes*, Springer Verlag Berlin Heidelberg, New York, 220pp
7. Z. Ullah, S. Atiq and S. Naseem, 2013, Indexing the diffraction pattern and investigating the crystal structure of Pb-doped strontium ferrites, *Journal of Scientific Research*, 5 (2), 235-244
8. R.D. Shannon, 1976, Revised effective ionic radii and systematic studies of interatomic distances in halides and chalcogenides, *Acta Crystallographica, Section A*, A32, 751-767
9. R.M. Barrer, 1941, *Diffusion in and through solids*, The MacMillan Company, New York, 460 pp
10. K. Shahi, W. Weppner and A. Rabenau, 1986, Defects and first order phase transition in AgI, *Physica Status Solidi A*, 93, 171-176

11. V.K. Kaushik, 1991, XPS core level spectra and Auger parameters for some silver compounds, *Journal of Electron Spectroscopy Related Phenomena*, 56, 273-277
12. J.F. Moulder, W.F. Stickle, P.E. Sobol, K.D. Bomben and J. Chastain, 1991, *Handbook of X-ray photoelectron spectroscopy*, Physical Electronics Inc., 255 pp
13. NIST database for XPS, 2012 Measurement Services Division, Material Measurement Laboratory, Updated on Sept. 15, [Accessed on 25<sup>th</sup> April 2017]
14. E. Barsoukov and J.R. Macdonald, 2005, *Impedance spectroscopy: theory, experiment and application*, John Wiley and Sons, New Jersey, 595 pp

## CHAPTER 4

### HALOGEN SENSING CHARACTERISTICS OF $\text{AgI}_{1-x}\text{Cl}_x$ ( $x=0-0.05$ )

#### 4.1 INTRODUCTION

Potentiometric sensors offer several advantages over other modes of sensing like conductometric, optical, etc. These sensors are highly selective and the sensing using such type of sensors is independent of the geometry of the cell [1]. The need for the halogen sensors has already been emphasised in the introduction chapter. This chapter elaborates the principle and the sensing characteristics of  $\text{AgI}_{1-x}\text{Cl}_x$  ( $x=0$  to  $0.05$ ) towards iodine and chlorine in trace levels.

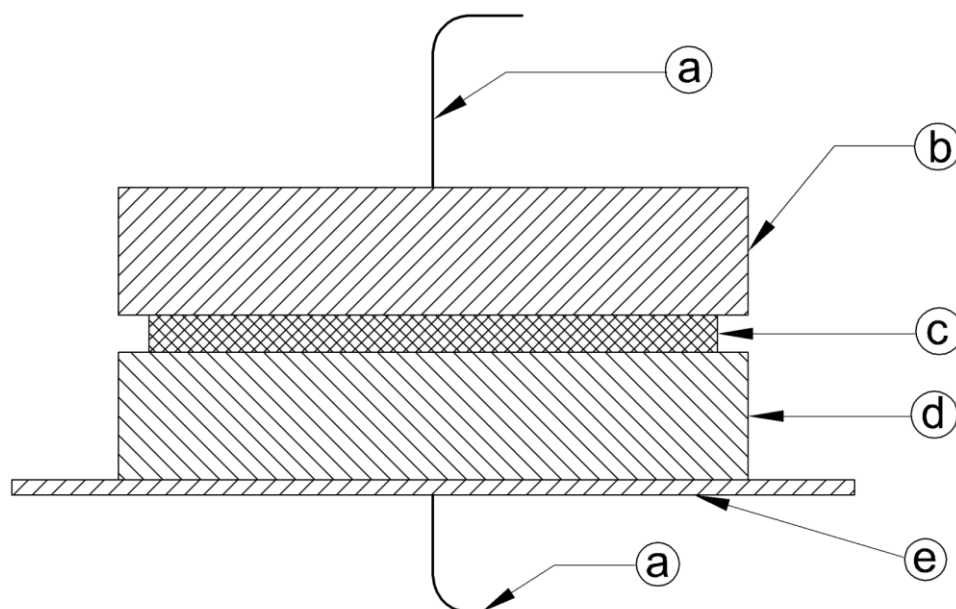
#### 4.2 EXPERIMENTAL

As discussed in the experimental section, sensor studies using iodine and chlorine were done in two different modes: iodine sensing was carried out in a dynamic mode where argon was used for introducing iodine into the glass chamber. A graduated syringe was used, in the case of chlorine, for admitting the gas into the reaction chamber. For halogen sensing studies, the sensing configuration was housed in a 1 L glass chamber. Theoretical calculations of emf were carried out from the basic thermodynamic functions of AgI at 428 K.

#### 4.3 PRINCIPLE OF HALOGEN SENSING BY $\text{AgI}_{1-x}\text{Cl}_x$

A sketch of the potentiometric cell employed for sensing is given in Fig. 4.1. The mobile species involved in the compositions of  $\text{AgI}_{1-x}\text{Cl}_x$  is mainly  $\text{Ag}^+$  ions. For the potentiometric cell,  $\text{Ag}|\text{AgI}_{1-x}\text{Cl}_x|\text{Pt}, \text{X}_2$ , where  $\text{X}_2=\text{I}_2/\text{Cl}_2$  involving the respective compositions will have an overall cell reaction as:





Cell configuration:  $\text{Ag}|\text{AgI}_{1-x}\text{Cl}_x|\text{Pt}$

- |                       |   |
|-----------------------|---|
| (a) Platinum leads    | (d) Solid electrolyte: $\text{AgI}_{1-x}\text{Cl}_x$ pellet |
| (b) Silver pellet     | (e) Working electrode (Pt)                                  |
| (c) Silver thick film |   |

**Fig. 4.1 Sketch of the electrochemical cell used for sensing halogen**

The reference electrode for potentiometric cell was metallic silver and therefore, activity of the Ag in the reference side will be unity, as silver metal is in the standard state. The redox reaction occurring at the electrode under equilibrium condition is given as:



Nernst equation for this cell is as given in equation (4.3) where E is the emf of the cell, R is the universal gas constant, T is the absolute temperature; n is the number of electrons transferred in the overall reaction, F is the Faraday constant and  $a_{\text{Ag}}$  is the activity of silver in the working electrode.

$$E = \frac{RT}{nF} \ln \left( \frac{1}{a_{\text{Ag}}} \right) \quad (4.3)$$

Based on the above equation, activity of silver ( $a_{\text{Ag}}$ ) is reduced at the working electrode side in the presence of iodine vapour. Therefore, the emf of the potentiometric cell

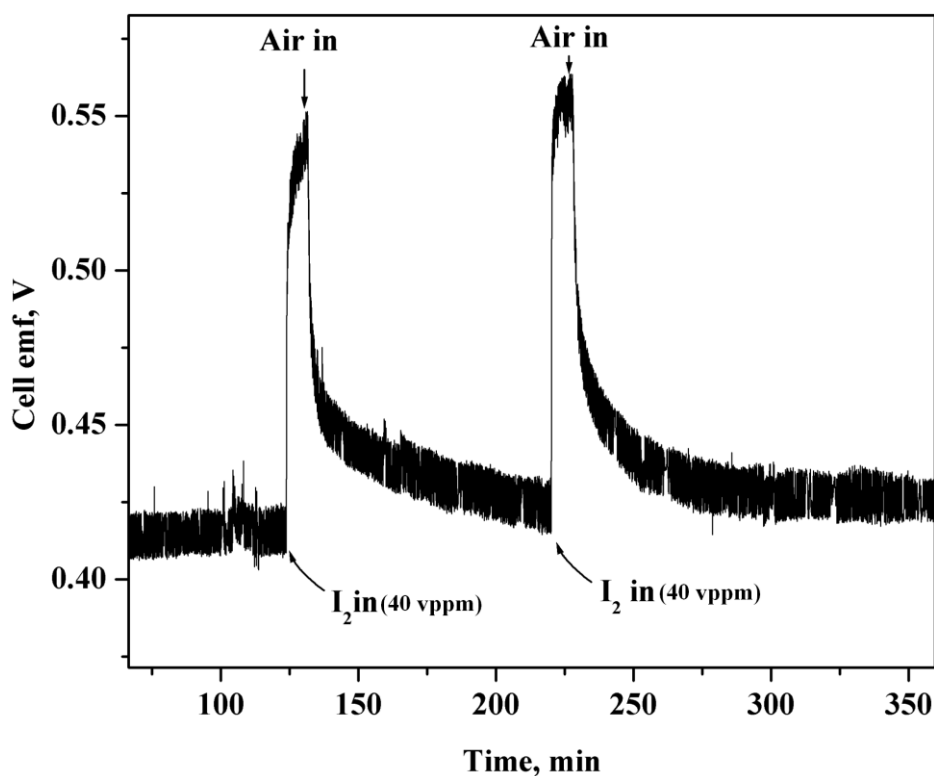


Fig. 4.2 Transient response of AgI and ~40 vppm of iodine gas at 428 K

increases. The typical transient obtained on exposure to iodine by AgI is shown in Fig. 4.2. The sensor retraced to its baseline when the cell was purged with argon. Purging of the chamber causes desorption of the gases adsorbed inside the electrochemical cell surface and also from the entire chamber.

#### 4.3.1 Theoretical emf calculation

Consider the formation of AgI from its constituent elements in the standard state:



The standard Gibbs energy formation of AgI at 428 K is  $-67.442 \text{ kJ}\cdot\text{mol}^{-1}$  [2]. The standard emf corresponding to temperature 428 K can be calculated from the equation

$$\Delta G_{\text{AgI}}^{\circ} = -nFE^{\circ} \quad (4.5)$$

where  $\Delta G_{\text{AgI}}^{\circ}$  is the standard Gibbs energy formation of AgI,  $n$  is the number of electrons in the redox reaction,  $F$  is the Faraday's constant,  $E^{\circ}$  is the emf of the cell in the standard state. The standard emf ( $E^{\circ}$ ), with  $n=1$  is around 698.9 mV. Considering the activity of

AgI and Ag to be unity, the emf of the cell (E) and the concentration of iodine/chlorine are related by the equation (4.6).

$$E = E^{\circ} - \frac{RT}{2F} \ln a_{[I_2/Cl_2]} \quad (4.6)$$

where R is the universal gas constant, T is the absolute temperature,  $a_{[I_2/Cl_2]}$  represents the activity of iodine or chlorine. By varying the concentration of the halogens there will be a change in the emf (E) of the cell.

#### 4.4 IODINE SENSING CHARACTERISTICS

The iodine sensing characteristics of the three compositions AgI, AgI<sub>0.975</sub>Cl<sub>0.025</sub> and AgI<sub>0.95</sub>Cl<sub>0.05</sub> towards ~6-60 vppm of iodine at 428 K was carried out using argon carrier.

The flow rate was optimised as 10 mL/min and fluctuations observed during the flow of

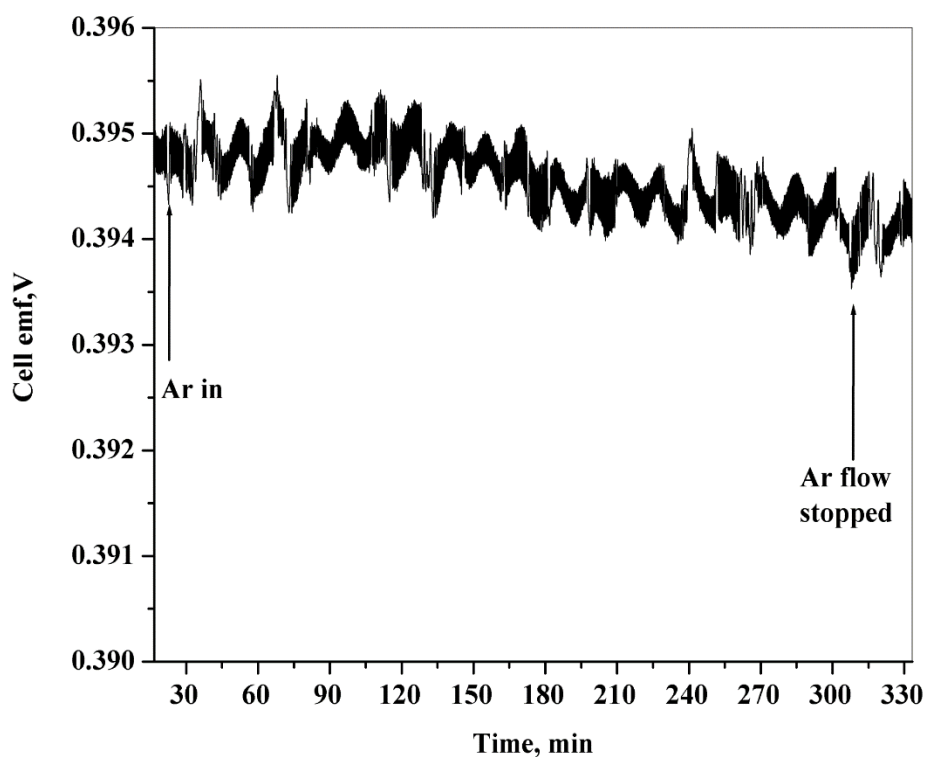


Fig. 4.3 Typical variation in the baseline of AgI based electrochemical cell during the passage of the argon carrier gas

Ar gas was around 1 mV change only. Fig. 4.3 represents the typical baseline recorded during the flow of Ar gas into the glass chamber containing the electrochemical cell.

Generally, the average time for response and 90 % retrace (to the baseline value) were around ~7 min and ~58 min for all the compositions investigated. This shows that the kinetics for the sensing and retrace are the same for all the compositions under study. For the same concentration of iodine vapour admitted, the response (change in the emf) towards the gas is in the order  $\text{AgI} < \text{AgI}_{0.975}\text{Cl}_{0.025} < \text{AgI}_{0.95}\text{Cl}_{0.05}$ . Similar trend was obtained for all the concentrations of iodine.

The typical transients obtained for AgI,  $\text{AgI}_{0.975}\text{Cl}_{0.025}$  and  $\text{AgI}_{0.95}\text{Cl}_{0.05}$  are shown in Fig. 4.4-4.6. The response of the transient was calculated by taking the difference in the emf of the cell after and before injecting the gas (equation (4.7)).

$$\text{Response} = V_{\text{gas}} - V_0 \quad (4.7)$$

where  $V_0$  is the emf in air and  $V_{\text{gas}}$  is the emf in the presence of the halogen.

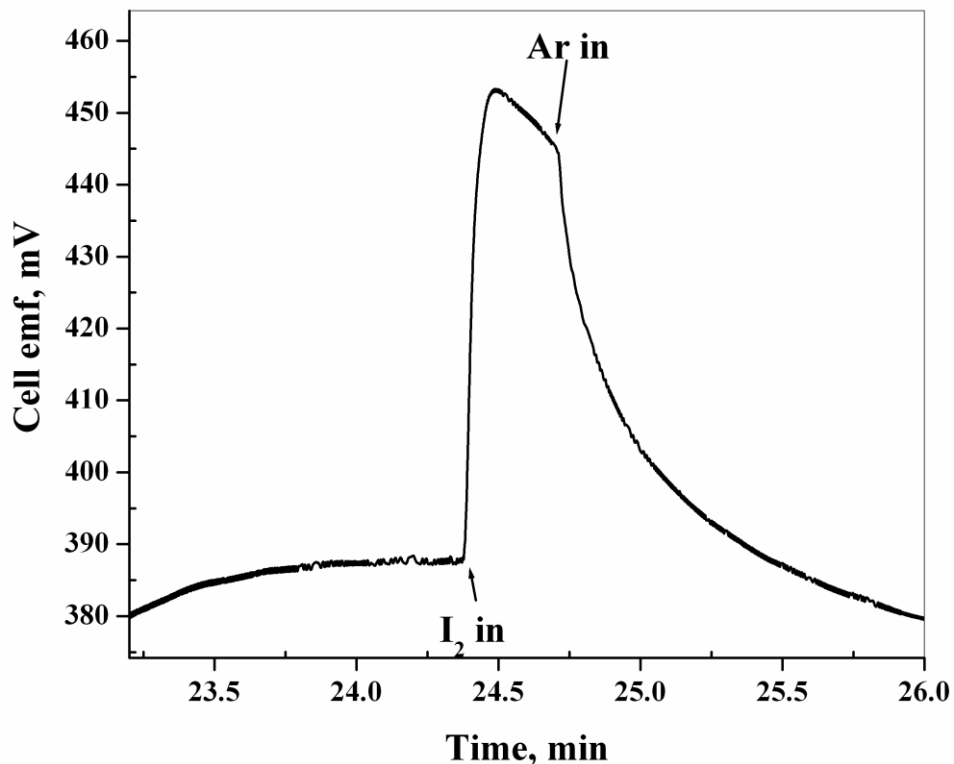


Fig. 4.4 Typical transient observed by AgI ~6 vppm of iodine at 428 K in argon

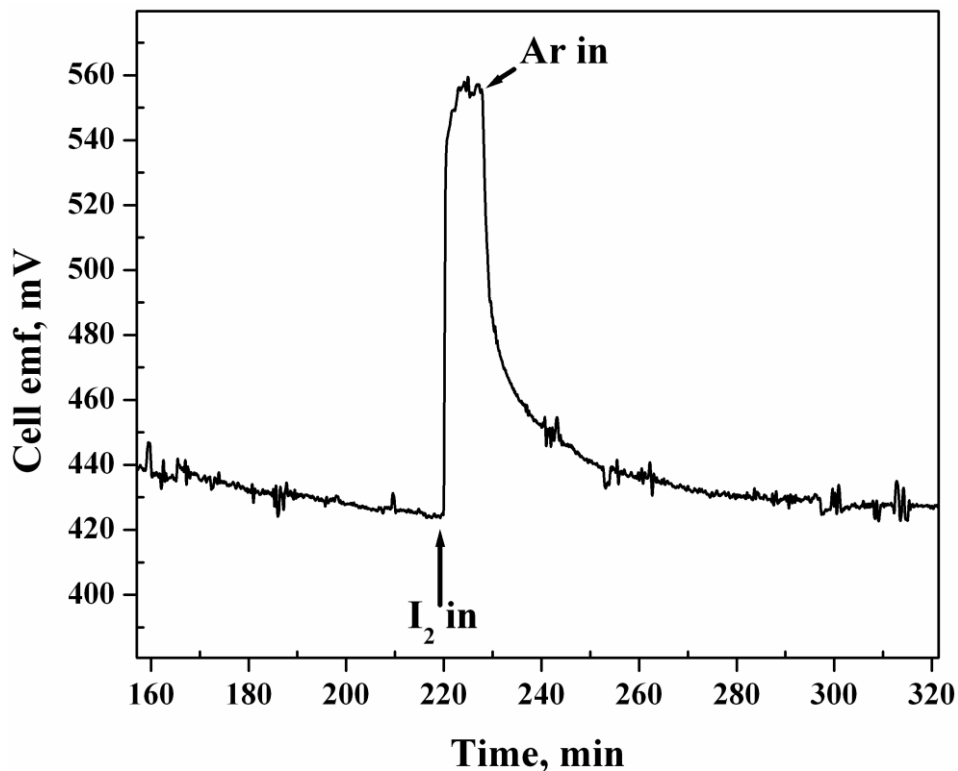


Fig. 4.5 Typical transient observed by  $\text{AgI}_{0.975}\text{Cl}_{0.025}$  ~6 vppm of iodine at 428 K in argon

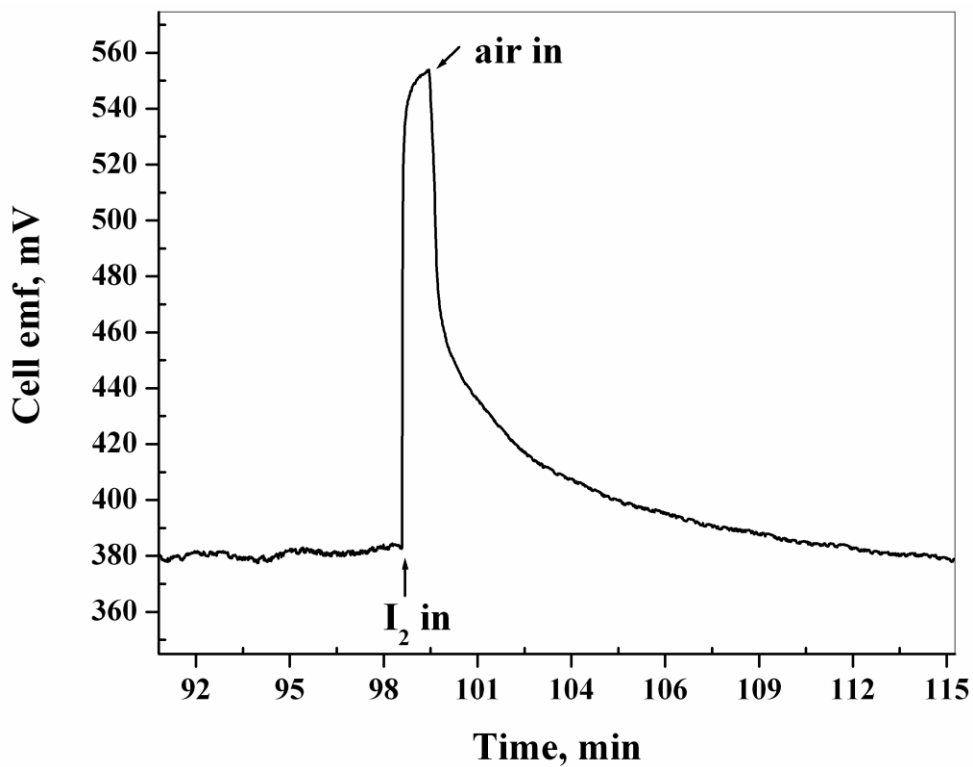


Fig. 4.6 Typical transient observed by  $\text{AgI}_{0.95}\text{Cl}_{0.05}$  towards ~6 vppm of iodine at 428 K in argon

The calibration plot for the concentration of ~6-60 vppm of iodine vapour on the compositions of AgI, AgI<sub>0.975</sub>Cl<sub>0.025</sub> and AgI<sub>0.95</sub>Cl<sub>0.05</sub> are shown in Fig. 4.7 (a-c). The value of the response of AgI towards the concentration of iodine was ~80-138 mV, whereas for AgI<sub>0.975</sub>Cl<sub>0.025</sub> and AgI<sub>0.95</sub>Cl<sub>0.05</sub> the response was in the range of ~90-140 mV and ~90-160 mV respectively. The values used in the calibration plot is the average response obtained for 7 to 9 individual experiments conducted for a given composition of AgI<sub>1-x</sub>Cl<sub>x</sub> towards a given concentration of iodine. The slopes for the three calibration plots of AgI<sub>1-x</sub>Cl<sub>x</sub> after the linear fit are shown in Table 4.1. However exact reasons for the response exhibited by AgI<sub>0.95</sub>Cl<sub>0.05</sub> over the other compositions are not known.

Study on the Cs doped AgI by Sola et al. [3] showed the usefulness of the compound to sense iodine from 385-5122 vppm at 373 K. On the other hand, the present studies using AgI<sub>1-x</sub>Cl<sub>x</sub> (x=0, 0.025 and 0.05) showed at least 80 mV change for ~6 vppm of iodine itself. The possibility of sensing low concentrations of iodine could be due to the temperature (428 K) of sensor studies. At this temperature, the kinetics of the sensing process is expected to be significantly higher than at 373 K [3].

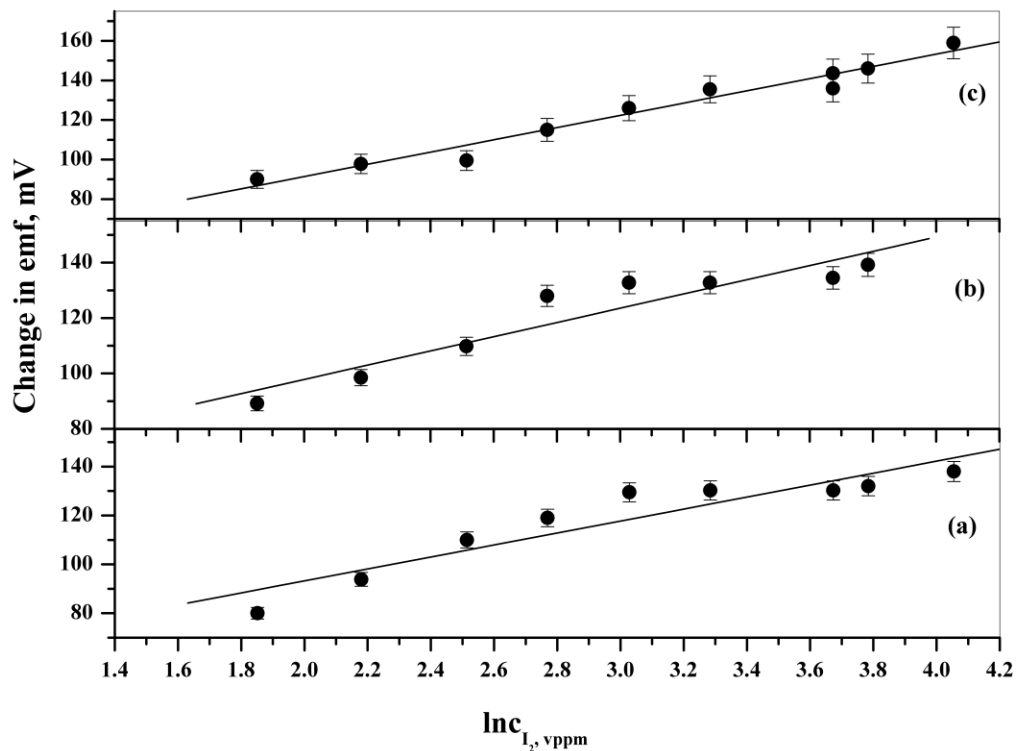


Fig. 4.7 Calibration plot of iodine sensing in the range of ~6-60 vppm for (a) AgI (b)  $\text{AgI}_{0.975}\text{Cl}_{0.025}$  and (c)  $\text{AgI}_{0.95}\text{Cl}_{0.05}$  in argon

Table 4.1 Fit parameters for the calibration plot for  $\text{AgI}_{1-x}\text{Cl}_x$  towards iodine sensing

| Composition                           | Fit parameters for the linear fit |       |
|---------------------------------------|-----------------------------------|-------|
|                                       | $y = A + Bx$                      |       |
|                                       | A, mV                             | B, mV |
| AgI                                   | 44.24                             | 35.49 |
| $\text{AgI}_{0.975}\text{Cl}_{0.025}$ | 46.44                             | 25.70 |
| $\text{AgI}_{0.95}\text{Cl}_{0.05}$   | 29.50                             | 30.94 |

Other compositions of  $\text{AgI}_{1-x}\text{Cl}_x$  ( $x > 0.05$ ) were also tested for iodine sensing in the same range of concentration of the iodine. The compositions of  $\text{AgI}_{1-x}\text{Cl}_x$  above  $x \geq 0.06$  were found to give low sensitivity towards iodine. As emphasised from the XRD and electrical conductivity studies in chapter 3, the limit of solubility of AgCl in AgI in the composition  $\text{AgI}_{1-x}\text{Cl}_x$  was  $x \leq 0.05$ . The reduction in the sensitivity above  $x > 0.05$  in  $\text{AgI}_{1-x}\text{Cl}_x$  could be due to the precipitation of the AgCl phase. It was also proved in the ionic transference

number measurements that the transference number for ions got reduced with the increase in the  $\text{Cl}^-$  concentration above the solubility limit of  $\text{AgI}_{0.95}\text{Cl}_{0.05}$ . Thus, the ionic conduction got reduced due to the precipitation of the  $\text{AgCl}$  phase. The details of studies based on the solubility product and the ionic transference number measurement were discussed in detail in chapter 3.

#### 4.5 COMPARISON OF EXPERIMENTALLY OBSERVED VALUES TO THE THEORETICAL CALCULATED EMF

It was described in section 4.3.1 that the emf of the electrochemical cell  $\text{Ag}|\text{AgI}_{1-x}\text{Cl}_x|\text{Pt}$  increases with the increase in the concentration of iodine. The plots of theoretical emf to the experimentally observed values are plotted in Fig. 4.8. Fairly good agreement is observed between the experimental values and theoretical predictions.

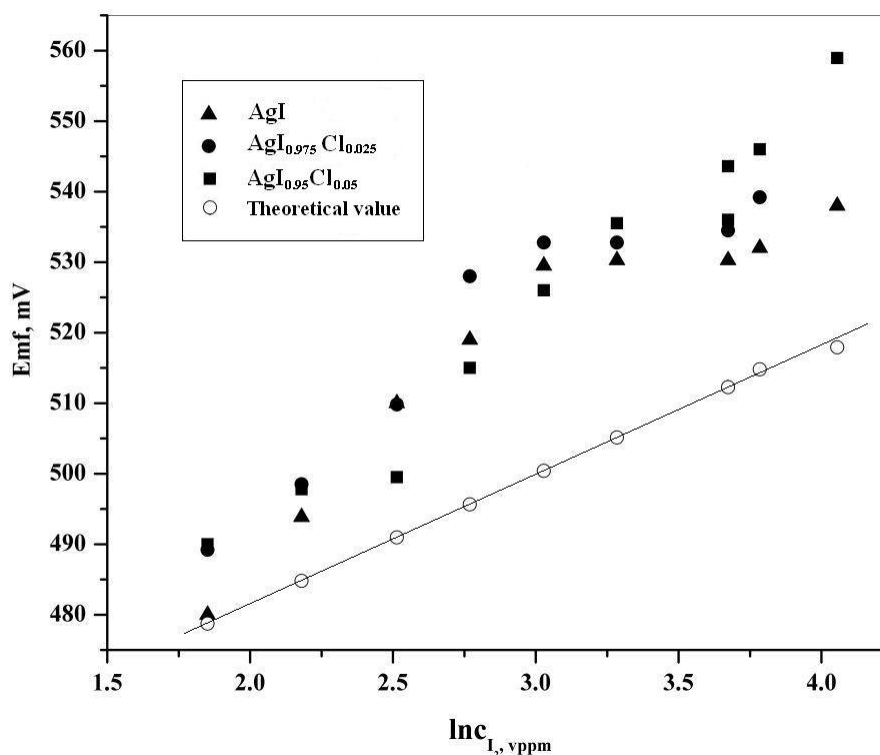


Fig. 4.8 Plot of experimental vs theoretical values of  $\text{AgI}_{1-x}\text{Cl}_x$  ( $x=0, 0.025$  and  $0.05$ ) equilibrated with  $\sim 6\text{-}60$  vppm of iodine at 428 K in argon

#### 4.6 CHLORINE SENSING CHARACTERISTICS

Chlorine sensing investigations were carried out on three compositions of AgI,  $\text{AgI}_{0.975}\text{Cl}_{0.025}$  and  $\text{AgI}_{0.95}\text{Cl}_{0.05}$  in the range of 20-100 vppb of the gas.  $\text{AgI}_{0.975}\text{Cl}_{0.025}$  and  $\text{AgI}_{0.95}\text{Cl}_{0.05}$  were found to give good response to trace levels (vppb) of chlorine gas. It was found that the AgI pellet did not retrace back after the injection of chlorine gas. This could be due to the formation of AgCl at the electrolyte|working-electrode interface due to the reaction of AgI with  $\text{Cl}_2$ . This stable layer can mask the activity of Ag on the working electrode side slowing down the normal retrace of the potentiometric cell. A methodology for elucidating such trace levels of gas adsorption is presented in chapter 5. Typical transients observed for  $\text{AgI}_{0.975}\text{Cl}_{0.025}$  are shown in Fig. 4.9 (a) and 4.9 (b) and that observed for  $\text{AgI}_{0.95}\text{Cl}_{0.05}$  are shown in Fig. 4.10 (a) and 4.10 (b) respectively. The average response time was around 7 min for both the compositions of  $\text{AgI}_{1-x}\text{Cl}_x$  ( $x=0.025$  and  $0.05$ ). The average 90 % retrace times for the compositions were around 12 min.

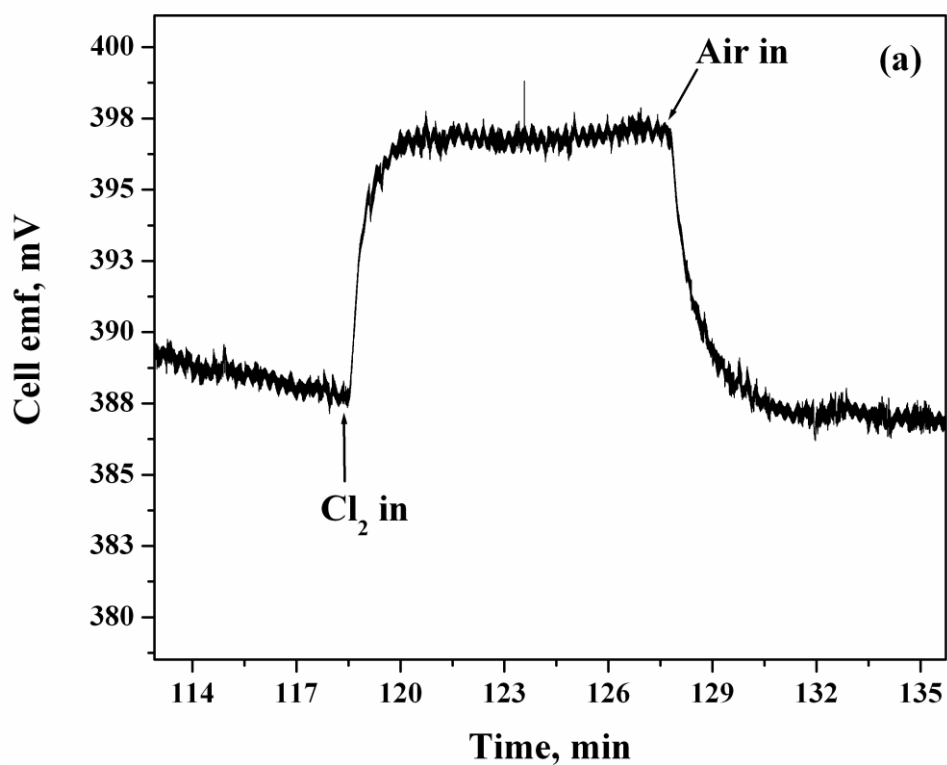


Fig. 4.9 (a) Typical transients observed for  $\text{AgI}_{0.975}\text{Cl}_{0.025}$  towards 20 vppb  $\text{Cl}_2$  in air

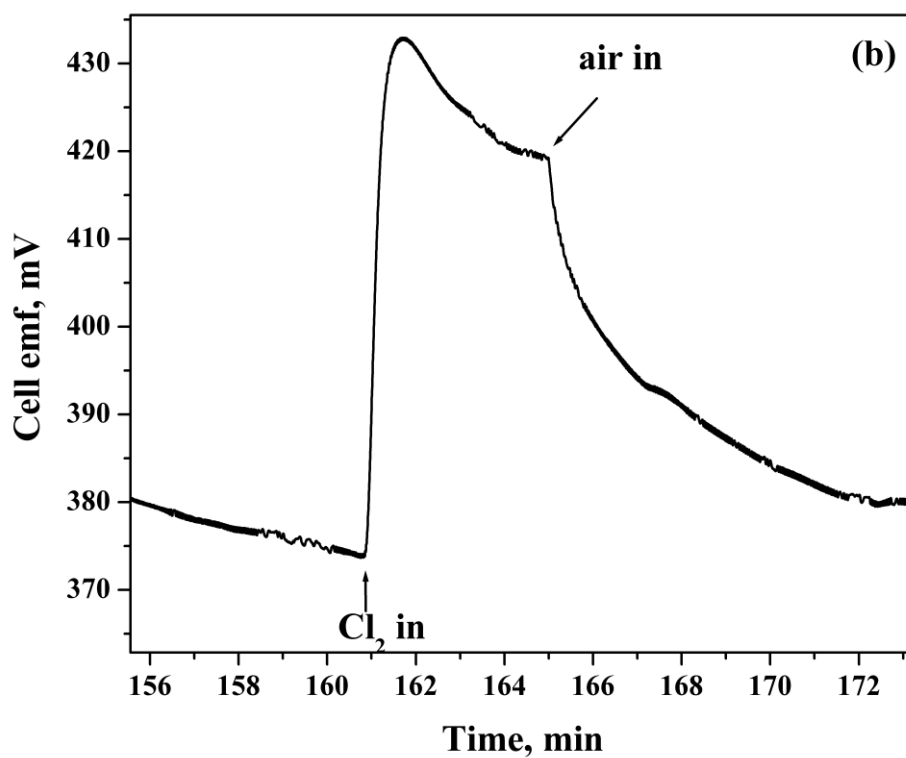


Fig. 4.9 (b) Typical transients observed for  $\text{AgI}_{0.975}\text{Cl}_{0.025}$  towards 100 vppb  $\text{Cl}_2$  in air

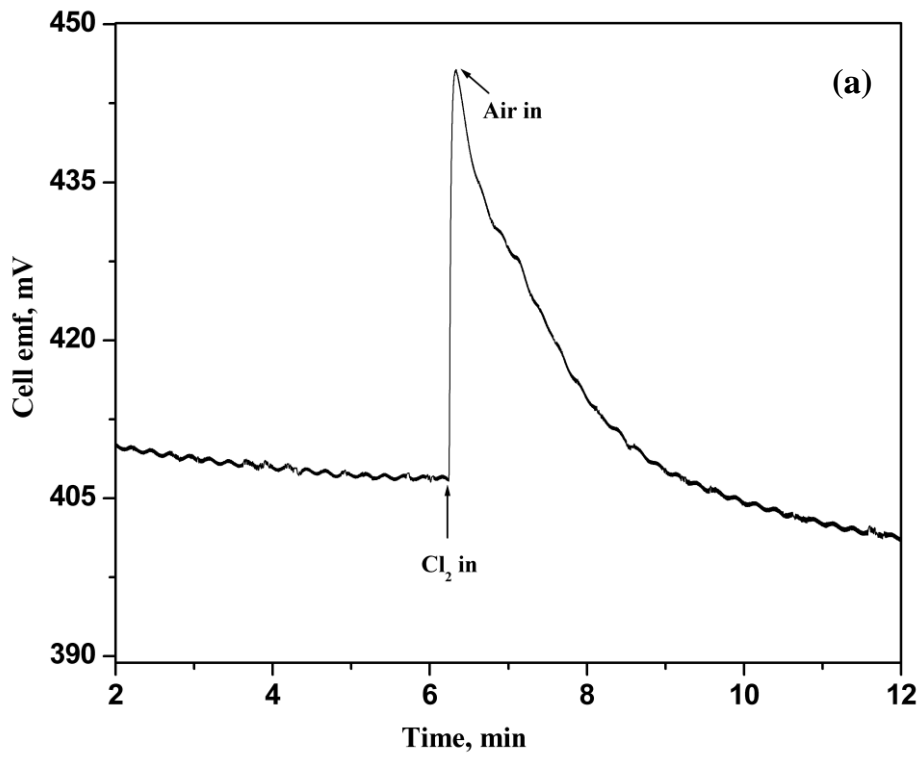


Fig. 4.10 (a) Typical transient exhibited by  $\text{AgI}_{0.95}\text{Cl}_{0.05}$  towards 20 vppb  $\text{Cl}_2$  gas in air

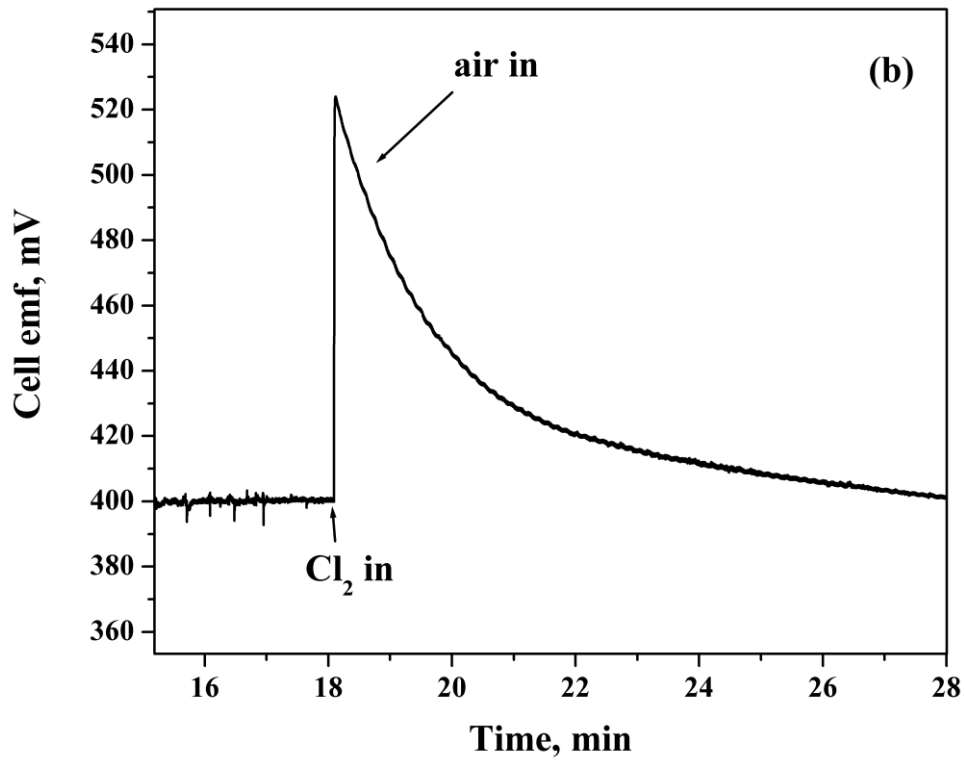


Fig. 4.10 (b) Typical transient exhibited by  $\text{AgI}_{0.95}\text{Cl}_{0.05}$  towards 100 vppb  $\text{Cl}_2$  in air

With respect to the retrace behaviour, the time required for removing the gas injected will be more compared to the response time, as the gas molecules would have stuck to the cooler regions of the glass chamber and requires more time for desorption. Also, iodine being a vapour will be condensing on the relatively cooler parts of the chamber making it still slower to desorb the vapours. Thus, it is observed that the average 90 % retrace times of  $\text{AgI}_{1-x}\text{Cl}_x$  towards iodine was more compared to that of chlorine.

Compositions above  $x > 0.05$  of  $\text{AgI}_{1-x}\text{Cl}_x$  system exhibited low sensitivity towards chlorine in the range of 20-100 vppb and hence were not considered for further sensor studies. This could be the same reason as explained in the iodine sensing characteristics exhibited by the same set of the compounds. The calibration plots of  $\text{AgI}_{0.975}\text{Cl}_{0.025}$  and  $\text{AgI}_{0.95}\text{Cl}_{0.05}$  are shown in Fig. 4.11.

From the slope of the calibration plot, the sensitivity for both the compositions were found to be the same whereas the response for the composition of  $\text{AgI}_{0.95}\text{Cl}_{0.05}$  was found to be higher than that of  $\text{AgI}_{0.975}\text{Cl}_{0.025}$ . The response of  $\text{AgI}_{0.975}\text{Cl}_{0.025}$  was in the range of 15-60 mV whereas the range for  $\text{AgI}_{0.95}\text{Cl}_{0.05}$  was around 30-120 mV. Table 4.2 gives the parameters used for fitting the calibration curve given in the Fig. 4.11.

The use of potentiometric sensors with auxiliary electrode, AgCl, was demonstrated in the literature of Hotzel and Weppner [4]. The cell,  $\text{Pt}|\text{Rb}_4\text{AgI}_5|\text{AgCl}$  used for sensing chlorine concentration from 102 vppm to percentage levels was demonstrated at 423 K. The unstable sensing characteristics shown by  $\text{Rb}_4\text{AgI}_5$  were reported to show a drift in the baseline of the sensor during sensing. It is to be noted that  $\text{AgI}_{1-x}\text{Cl}_x$  ( $x=0.025$  and  $0.05$ ) is capable of sensing down to 20 vppb of chlorine. Further, no drift in the baseline was observed over a period of several months.

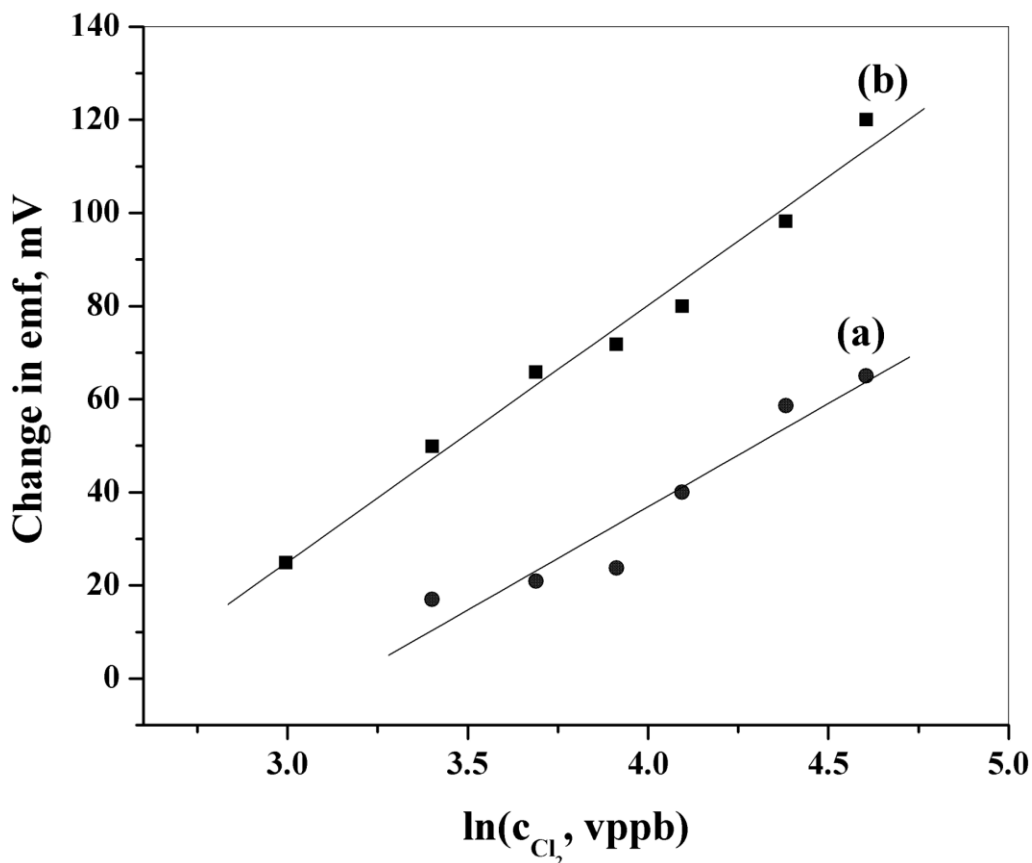


Fig 4.11 Calibration plots of (a)  $AgI_{0.975}Cl_{0.025}$  and (b)  $AgI_{0.95}Cl_{0.05}$  towards 20-100 vppb chlorine at 428 K in air

Table 4.2 Fit parameters for the calibration plot for  $AgI_{1-x}Cl_x$  towards chlorine sensing

| Composition             | Fit parameters for the linear fit |       |
|-------------------------|-----------------------------------|-------|
|                         | $y = A + Bx$                      |       |
|                         | A, mV                             | B, mV |
| $AgI_{0.975}Cl_{0.025}$ | -102.451                          | 45.91 |
| $AgI_{0.95}Cl_{0.05}$   | -140.468                          | 44.34 |

## 4.7 CONCLUSION

Sensing characteristics of the composition  $AgI$ ,  $AgI_{0.975}Cl_{0.025}$  and  $AgI_{0.95}Cl_{0.05}$  show good response towards iodine. Of the three compositions,  $AgI$  show maximum sensitivity towards iodine in the range of ~6-60 vppm. Chlorine sensing studies carried out on  $AgI_{0.975}Cl_{0.025}$  and  $AgI_{0.95}Cl_{0.05}$  show better sensitivity for  $AgI_{0.95}Cl_{0.05}$  towards 20-100 vppb of  $Cl_2$ . The compositions with  $x \geq 0.06$  in  $AgI_{1-x}Cl_x$  was found to have lower sensitivities as the ionic conductivity and the transference number was found to reduce

with increase in  $\text{Cl}^-$  content above  $x > 0.05$ . Thus, it was possible to demonstrate the usefulness of  $\text{AgI}_{1-x}\text{Cl}_x$  compositions to sense gases down to  $\sim 6$  vppm of iodine and  $\sim 20$  vppb of chlorine. Further detailed investigations are needed to understand the enhanced sensitivities and responses exhibited by  $\text{AgI}_{0.95}\text{Cl}_{0.05}$  towards iodine and chlorine.

#### **4.8 REFERENCES**

1. W. Weppner, 1987, Solid-state electrochemical gas sensors, *Sensors and Actuators*, 12, 107-119
2. I. Barin, 1995, Thermochemical data of pure substances, 3<sup>rd</sup> ed., VCH, Weinheim, 1885 pp
3. M. E. Sola, H.G. Rotstein and J. C. Bazán, 2002, The  $\text{Ag(s)}/\text{AgI(s)}/\text{graphite}$  solid cell as iodine sensor: speed of response and use of Cs doped AgI as electrolyte, *Journal of Solid State Electrochemistry*, 6 (4), 279-283
4. G. Hotzel and W. Weppner, 1986, Application of fast ionic conductors, *Solid State Ionics*, 18 and 19, 1223-1227

*This page is intentionally left blank.*

## **CHAPTER 5**

### **METHODOLOGY FOR ELUCIDATING THE MECHANISM OF AgI SENSING TOWARDS CHLORINE**

#### **5.1 INTRODUCTION**

From the material point of view, AgI was found to sense only iodine whereas  $\text{AgI}_{1-x}\text{Cl}_x$  ( $x=0.025$  and  $0.05$ ) were found to sense both iodine and chlorine. Since low level of halogens were used for understanding the sensing characteristics, the adsorption of the chlorine gas on the AgI surface leading to the formation of the thermodynamically stable AgCl species was difficult to realise with the existing methodologies. A methodology to analyse such low-levels of adsorption of a compound on the working electrode surface was evolved using X-ray photoelectron and dielectric impedance spectroscopic techniques. This chapter deals with the salient results obtained from these measurements.

#### **5.2 EXPERIMENTAL**

Using the in-house fabricated three electrode system, the interface of the two electrolytes (AgI and  $\text{AgI}_{0.95}\text{Cl}_{0.05}$ ) was studied using dielectric impedance spectroscopy. XPS studies carried out on the surface gives information regarding the by-product formed which can be envisaged as a change in the chemical environment of the material.

#### **5.3 NON RETRACING BEHAVIOR OF AgI TOWARDS CHLORINE**

Fig. 5.1 shows the typical transient observed for AgI when 40 vppb of  $\text{Cl}_2$  was injected at 428 K. The response (change in emf) for the injection of 40 vppb chlorine was around 232 mV. The value of emf then pegged around 452 mV which was ~80 mV higher than the baseline emf of AgI at 428 K (~372 mV). Even after passing Ar for 50 min, the baseline emf was not attained. The non retracibility of AgI towards chlorine gas strikes a marked difference for the sensing characteristic of AgI, where the compound can only sense iodine but not chlorine.

The involvement of any reaction between Ag and Cl could be one reason for the non retracing behaviour of AgI. Investigation of the top layer of the pellet after the interaction and the study of the working electrode interface was the only way to understand the mechanism, as the content of Cl<sup>-</sup> was very low that it cannot be detected using any other technique. Thus, X-ray photoelectron spectroscopy and electrochemical impedance spectroscopy were used to explore the change in the chemical environment and to observe the changes in the electrolyte/working electrode interface.

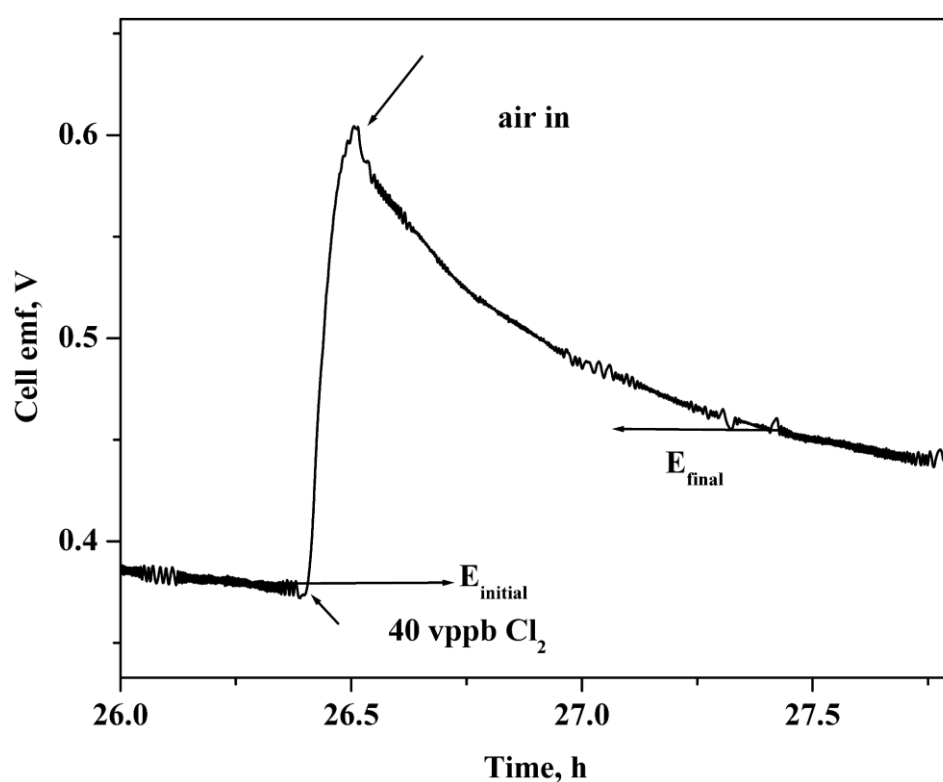


Fig. 5.1 Transient response for AgI towards 40 vppb Cl<sub>2</sub>

### 5.3.1 X-ray photoelectron spectroscopic studies

For XPS studies, the pellet was exposed to 500 vppb of chlorine at 428 K and then, the quenched pellet was analysed using the facility. XPS studies on AgI after exposure to chlorine (Fig. 5.2) shows Ag 3d main peak at 368.4 eV and 374.5 eV which corresponds to Ag 3d<sub>5/2</sub> and Ag 3d<sub>3/2</sub>. The small peak at 370.0 and 376.1 eV adjacent to the main peak

of Ag 3d at a higher binding energy difference of  $\sim 1.2$  eV corresponds to  $\text{Ag}^+$  surrounded by  $\text{Cl}^-$  ions. From the literature, AgI and  $\text{AgF}$  whose anions are having the highest electronegativity differences, the binding energy values of the bonded  $\text{Ag}^+$  ion was varying only  $\sim 1.6$  eV in magnitude [1]. Thus, the peak appearing at  $\sim 1.2$  eV difference from the main peak of Ag 3d corresponds to the formation of AgCl. AgCl, when formed can also affect the XPS pattern of  $\Gamma$  in the surrounding. As observed in Fig. 5.3 corresponding to I 3d pattern, a small peak with high binding energy of 621.2 eV at  $\sim 2.0$  eV difference from the major I  $3d_{5/2}$  peak, shows the presence of a highly electron withdrawing groups close to the  $\Gamma$  ion. The presence of  $\text{Cl}^-$  around iodine in ICl was reported to shift the binding energy of I 3d by  $\sim 2$  eV from I 3d binding energy in AgI [1]. ICl is having a boiling point of 370 K [2]. Thus, at the temperature of the study ICl is a gas, but, when the pellet is quenched to room temperature, ICl solidifies as 325 K is the melting point of ICl [2]. The formation of the AgCl could be envisaged in a cell formed at the interface of the working electrode and at the areas which are exposed to the gas (the sides of the pellet). The reaction for the formation of AgCl can be represented as:

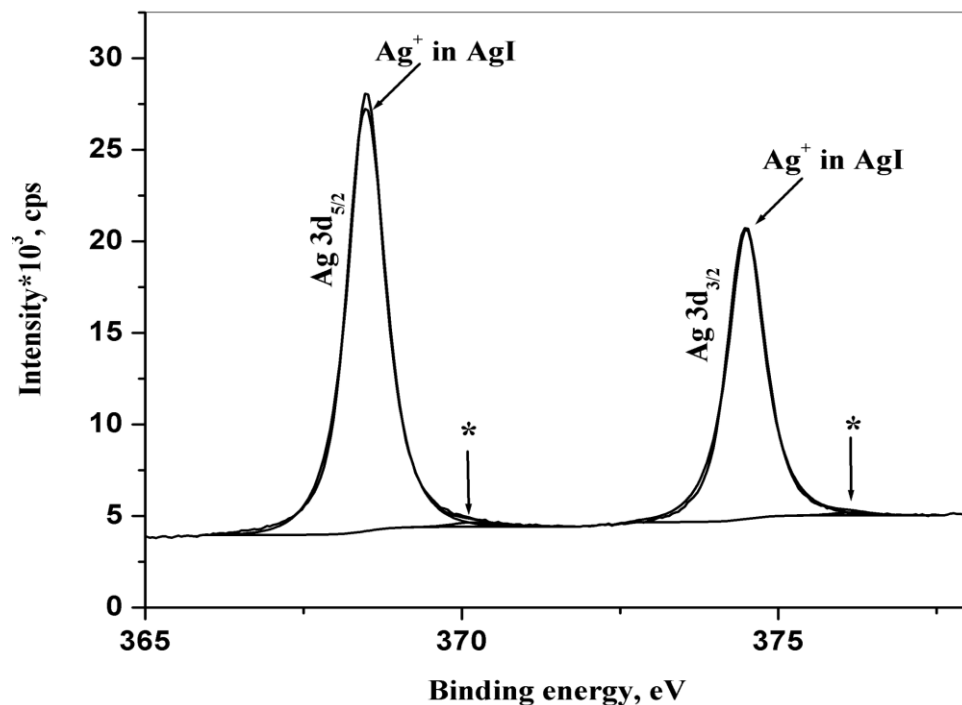


Fig. 5.2 XPS pattern of Ag 3d peak after exposure to 500 vppb of  $\text{Cl}_2$  gas at 428 K \*represents the formation of AgCl

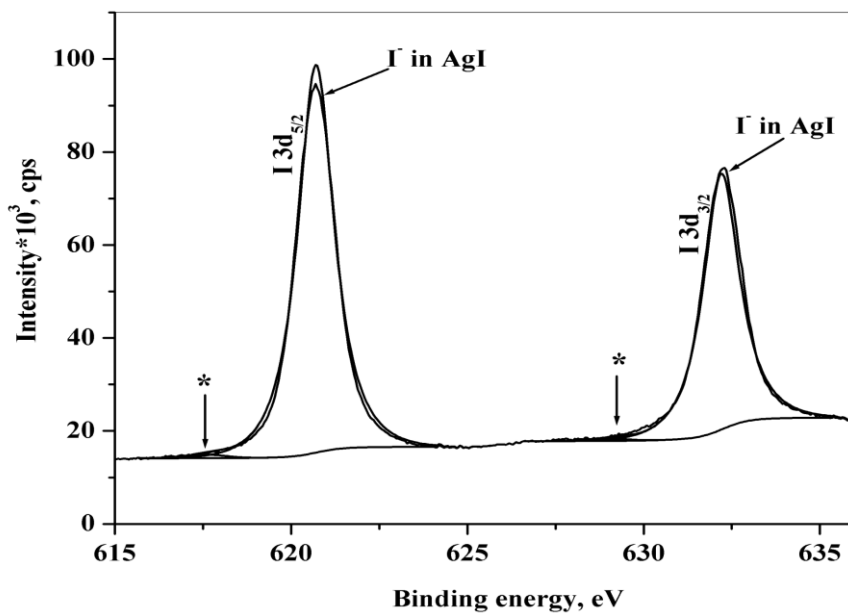
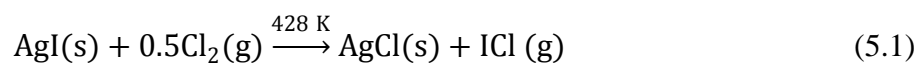
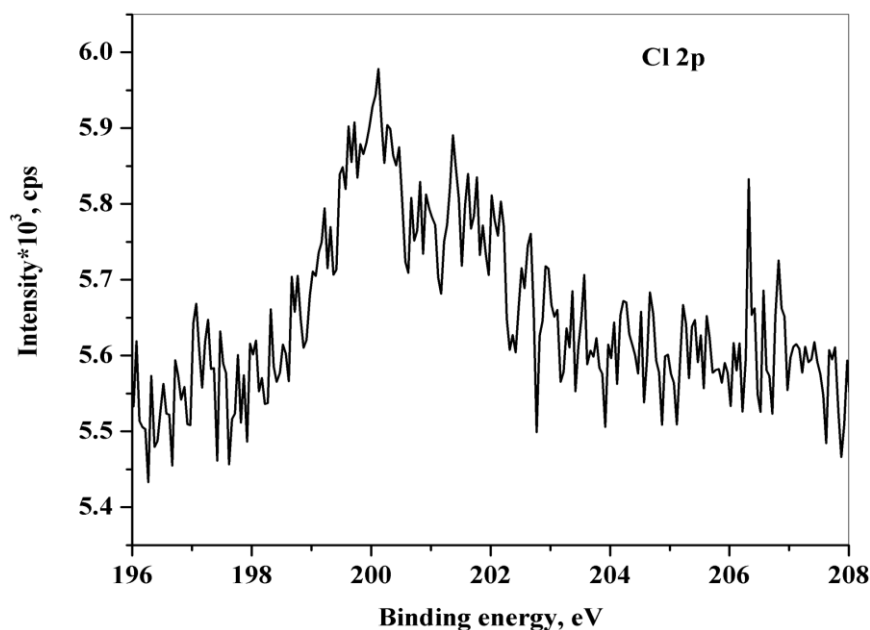


Fig. 5.3 XPS pattern of I 3d peak for AgI after exposure to 500 vppb of  $\text{Cl}_2$  gas at 428 K \* represents the formation of ICl



The AgCl formed stays as a solid layer on top of AgI, whereas ICl exists as a gas at these temperatures and is removed while flushing with air. The formation of AgCl by silver ion and ICl by iodide ion shifts the entire emf in favour of equilibrium towards AgCl, as



**Fig. 5.4 XPS pattern of Cl 2p peak in AgI after exposure to 500 vppb of Cl<sub>2</sub> gas at 428 K**

AgCl is thermodynamically more stable than AgI. The standard Gibbs energy of formation of AgI and AgCl at room temperature (298 K) is -66.19 kJ/ mol and -109.72 kJ/ mol respectively [3]. The chance of removal of AgCl becomes difficult, if it forms on the surface of AgI. This gives rise to a new emf on the surface due to the new equilibrium established. The emf of any cell can be calculated using the equation:

$$\Delta G = -nFE \quad (5.2)$$

The Gibbs energy for the formation of ICl is also negative at 428 K [4]. This also agrees with the transient obtained for AgI when injected with chlorine. The emf value increases after injection of chlorine even at ppb levels of concentration of gas as seen in Fig. 5.1. The range of energies from 196 eV to 208 eV in XPS corresponds to the Cl 2p region (Fig. 5.4). There is an increase in intensity of the Cl 2p region indicating the presence of chlorine on the topmost layer of AgI after exposure to chlorine gas.

### 5.3.2 Study on the working electrode interface of AgI using impedance spectroscopy

The characterisation of the working electrode interface can be carried out in one of the two ways:

- (a) On a symmetrical cell equipped with two nominally identical electrodes using a small ac signal at zero dc polarisation. In this case, the polarisation obtained can be divided into two, each obtained from two identical electrodes.
- (b) On a three-electrode cell with working, counter and reference electrode under potentiostatic/galvanostatic control. The measurement requires an electrochemical interface coupled with FRA.

Exchange current density generally depends on the concentration of the analyte, concentration of adsorbed species and temperature. The exchange current density in such cases is called apparent exchange current density. Only when the electrode surface area is having a significant role in the potentiometric cell, the term apparent and intrinsic (when the electrode surface area is different from the geometric area) exchange current densities are used. It is difficult to resolve the electrode interface in a two electrode configuration, where the working electrode gets polarised due to the adsorption of a new layer formed as the current flows through the adsorbed layer at the working electrode.

The measurements using three-electrode configuration carried out on AgI in air and in the presence of chlorine and iodine have given supporting information for the XPS carried out on AgI. The plots of impedance obtained at 428 K with an applied perturbation potential of 150 mV is given in Fig. 5.5-5.7. It is observed that for AgI, the values of charge transfer resistance are closer for unexposed and iodine exposed pellet whereas, the interfacial capacitance at higher frequencies (double layer capacitance) increase shows the adsorption of an intermediate [5]. The surface area of the working and counter electrode pasted over AgI pellet was  $\sim 0.5024 \text{ cm}^2$ .

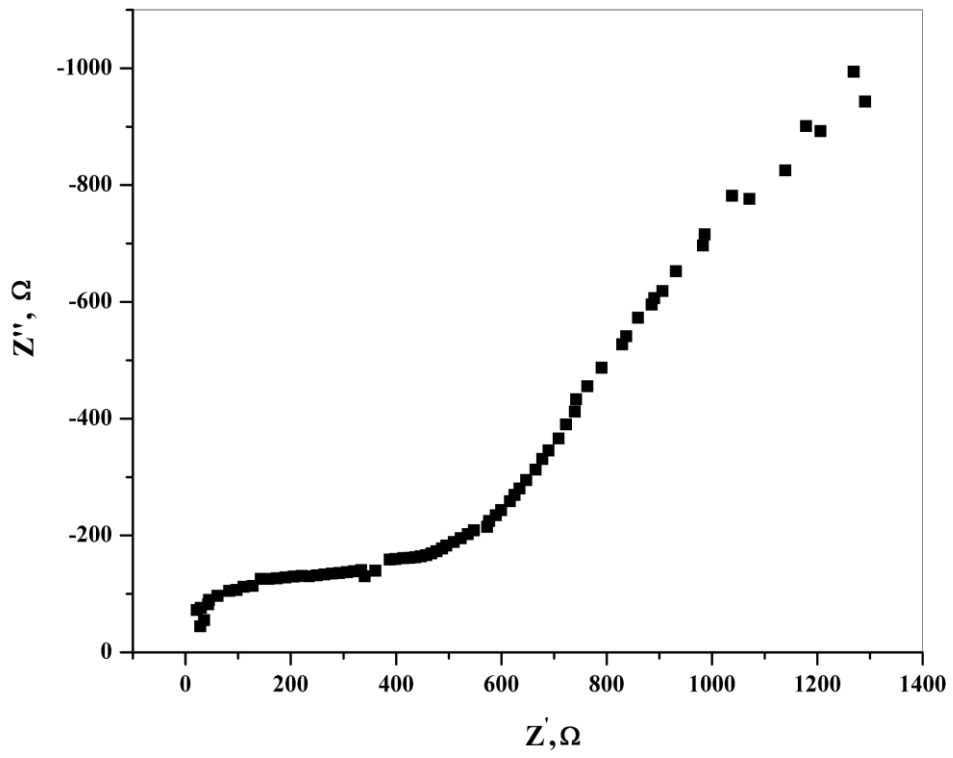


**Fig. 5.5 Nyquist plot of AgI at 428 K in air**

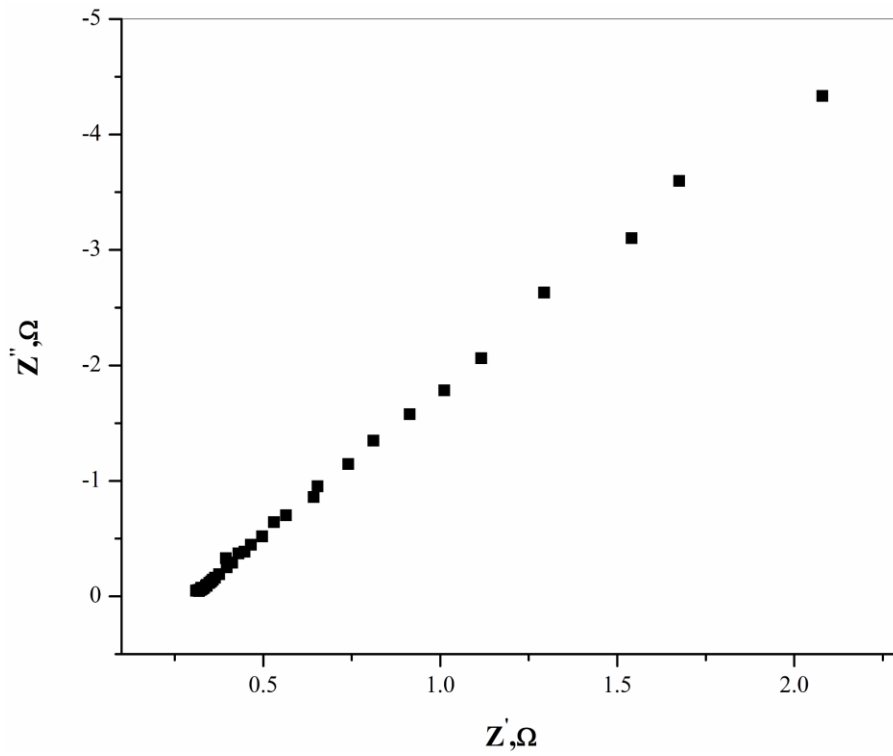


**Fig. 5.6 Nyquist plot of AgI exposed to iodine at 428 K in air**

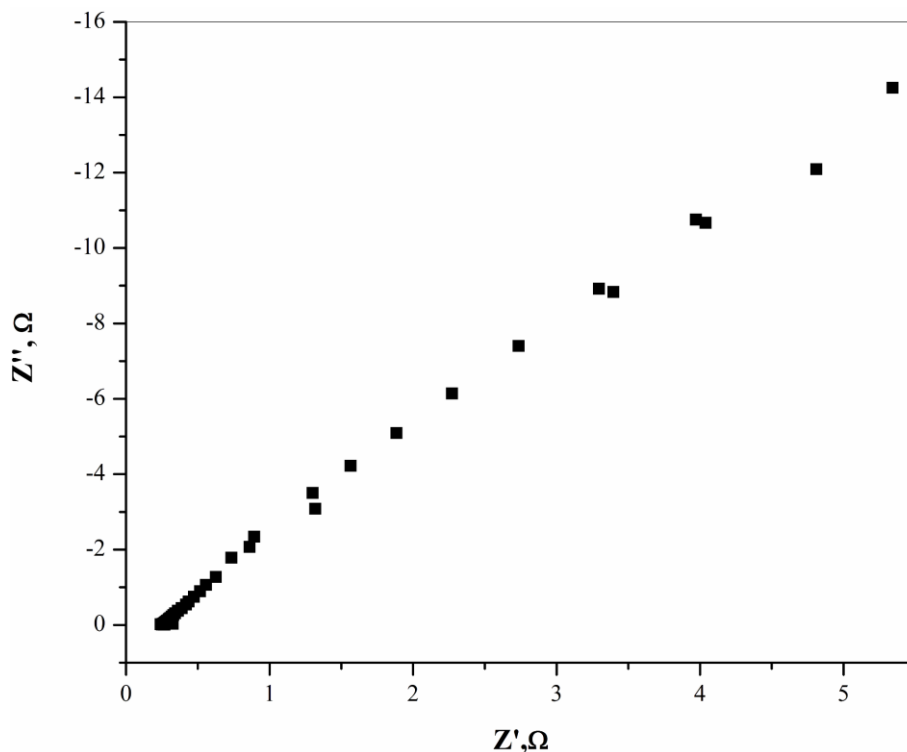


**Fig. 5.7 Nyquist plot of AgI after exposure to chlorine at 428 K in air**

The equivalent circuit for the above three Nyquist plots were derived from various approximations [6]. To manifest the diffusion of  $\text{Ag}^+$  and  $\text{Cl}^-$  at the electrode-electrolyte interface to react with the analyte gas, the preferred equivalent circuit treatment can be done based on the Erschler-Randles impedance [6, 7] for a two electrode configuration. The equivalent circuit for the cell is given in Fig. 5.8 below:

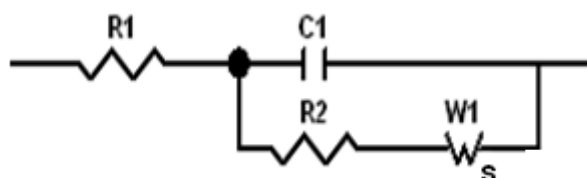


**Fig. 5.8 Equivalent circuit based on Erschler-Randles impedance [5]**

where  $R_1$  is the cell resistance,  $C_1$  is the double layer resistance,  $R_2$  is the charge transfer resistance and  $W_1$  is the Warburg diffusion due to the diffusing ions. As explained in chapter 2, assuming low overpotential, from equivalent circuit fitting of the curves, the

exchange current densities with respect to charge transfer resistance can be calculated using equation (5.3) [8].

$$i_0 = \frac{RT}{nFR_2} \quad (5.3)$$

where  $i_0$  is the exchange current density,  $R$  is the universal gas constant,  $n$  is the number of electrons involved in the charge transfer,  $F$  is the Faraday constant and  $R_2$  is the charge transfer resistance. The equivalent circuit used for the fitting of the three curves is given in Fig. 5.9.

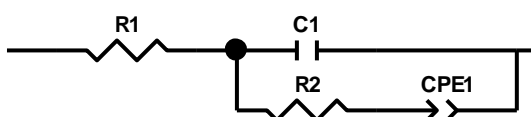


**Fig. 5.9 Equivalent circuit used for fitting AgI three electrode system at 428 K**

In Fig. 5.9,  $R_1$  is the cell resistance,  $R_2$  represents the charge transfer resistance and  $C_1$  is the double layer capacitance. From the value of  $R_2$ , which represents the charge transfer resistance, the exchange current densities for three conditions mentioned above were calculated using the above equation.  $CPE_1$  represents a constant phase element. As explained in the experimental section (chapter 2), the constant phase element represents the deviation from the ideal capacitance behaviour. The calculated exchange current densities are given in Table 5.1. The experiments were repeated three times to obtain concordant values. The values obtained from each set of experiment were averaged for calculating the exchange current density. The error in the estimation is in the range of  $(\pm)10\%$ . The components used in the equivalent circuit fitting gave the following values for the respective components:

**Table 5.1 Values of the circuit components used for equivalent circuit fitting**

| Sl.No: | Components                | Unexposed AgI         | AgI exposed to iodine  | AgI exposed to chlorine |
|--------|---------------------------|-----------------------|------------------------|-------------------------|
| 1.     | R1, ohm                   | 24.51                 | 31.84                  | 0.2785                  |
| 2.     | C1, F                     | $2.89 \times 10^{-7}$ | $8.909 \times 10^{-4}$ | $1.935 \times 10^{-3}$  |
| 3.     | R2, ohm                   | 380                   | 0.01                   | 20.07                   |
| 4.     | Q1, CPE                   | $2.4 \times 10^{-7}$  | $2.592 \times 10^{-5}$ | $2.222 \times 10^{-3}$  |
| 5.     | $n_w$ , order             | 0.551                 | 0.3915                 | 1                       |
| 6.     | $I_o$ , $\text{Acm}^{-2}$ | $1.93 \times 10^{-4}$ | 0.136                  | $1.83 \times 10^{-3}$   |

CPE: Constant Phase Element

From the above table, it is seen that the exchange current densities calculated for AgI in air behaves as a normal Warburg element with  $n_w \sim 0.5$ . The exchange current density was found to increase as the AgI is exposed to iodine. An increase in the exchange current density by an order of three proves that AgI facilitates iodine sensing. Thus, the kinetics of diffusion in the presence of iodine is faster than the equilibrium attained by AgI in air with the respective electrode. In the case of AgI exposed to chlorine, the current densities are lower than that for iodine exposure. This shows that the reaction at the interface is impeded. The value of order of the CPE ( $n_w$ ) is one in the case of chlorine exposed AgI. As the order is one which represents a pure capacitor a highly insulating material is formed at the interface. AgCl is an insulating material with a direct band gap of 5.6 eV [9]. Even though AgCl is an ionic conductor [10], the formation of this layer at the interface of the electrolyte-electrode, will slow down the redox reaction at the working electrode side. This in turn will result in the slow retrace behaviour of the potentiometric cell.

## 5.4 CONCLUSION

A methodology was evolved to understand the trace level of gas adsorption on the surface of AgI upon exposure of chlorine using XPS and EIS techniques. The significance of the diffusion control during the presence of the analyte gases were understood from the Nyquist plots obtained from impedance measurements. The presence of AgCl after the exposure of chlorine gas was confirmed by the behaviour of the layer formed on AgI, eventually increasing the capacitance of the working electrode-electrolyte interface. The presence of an additional peak in Ag 3d and I 3d XPS pattern confirms the presence of Cl<sup>-</sup> in the vicinity of Ag<sup>+</sup> and I<sup>-</sup> ion bringing a change in the chemical environment of both the ions. Thus, the chemical reaction due to the formation of AgCl on the surface of AgI is the main reason for the non-retracing characteristics of AgI as an electrolyte in chlorine sensing.

## 5.5 REFERENCES

1. J.F. Moulder, W.F. Stickle, P.E. Sobol, K.D. Bomben and J. Chastain, 1991, Handbook of X-ray photo-electron spectroscopy, Physical Electronics Inc., 255pp
2. R.G. Brisbois, R.A. Wanke, K.A. Stabbs, R.V. Stick, 2004, Encyclopaedia of reagents for organic synthesis, John Wiley and Sons
3. N.N. Greenwood, and A. Earnshaw, (1997), Chemistry of elements (2<sup>nd</sup> ed.), Oxford: Butterworth Heinemann, 1600 pp
4. K.K. Kelly, 1960, Contributors to data on theoretical metallurgy, US Department of Interior, 231 pp
5. N.G. Bukun and A.E. Ukshe, 2009, Impedance of solid electrolyte system, Russian Journal of Electrochemistry, 45, No.1, 11-24
6. J.E.B. Randles, 1947, Kinetics of rapid electrode reactions, Discussions of the Faraday Society, 1, 11-19

7. J. Corish and P.W.M Jacobs, 1972, Ionic conductivity of silver chloride single crystals, *Journal of Physics and Chemistry of Solids*, 33, 1799-1818
8. B.V. Ershler, 1947, Investigation of electrode reactions by the method of charging curves and with the aid of alternating currents, *Discussions of the Faraday Society*, 1, 269-277
9. E. Barsoukov (ed.) and J.R. Macdonald (ed.), 2005, *Impedance spectroscopy: theory, experiment, and applications*, 2<sup>nd</sup> ed., John Wiley & Sons, New York, 616 pp
10. J. Tejada, N.J. Shevchik, W. Braun, A. Goldmann and M. Cardona, 1975, Valence bands of AgCl and AgBr: UV photoemission and theory, *Physical Review B*, 12, 1557-1566

## **CHAPTER 6**

### **FABRICATION AND TESTING OF MINIATURISED CHLORINE SENSOR**

#### **6.1 INTRODUCTION**

Sensors or devices, in the end, must be small and handy. Therefore, the miniaturisation of the sensor is an important task for delivering, better devices which serves the required application. As mentioned in the introduction chapter, in the section related to pyroprocessing facility it was mentioned that large amount of chlorine is used for drying the chloride electrolyte melt used for the process. This chapter explains the fabrication of the miniaturised sensor for chlorine and its testing. Performance evaluation of the sensor towards trace levels of chlorine is described in the chapter.

#### **6.2 EXPERIMENTAL**

The pellet of  $\text{AgI}_{0.95}\text{Cl}_{0.05}$  was packed to alumina substrate using silver paste (reference electrode). A platinum mesh pressed from the opposite side was acting as the porous working electrode. A screen printed platinum heater serves as a source of heat to maintain the sensor material at 428 K. As described in the experimental section, chlorine was injected using a gas-tight syringe. After attaining the equilibrium, dry air was passed to bring the emf of the electrochemical cell back to the normal baseline. The sensor assembly and chamber was made with glass which are inert to chlorine.

#### **6.3 PRINCIPLE OF OPERATION**

The cell works on the principle of potentiometric sensor, which is explained in chapter 3. There will be a change in the emf of the cell in the presence of chlorine gas due to the decrease in the activity of the Ag at the working electrode. The equation, which governs the behaviour of the cell, is the Nernst equation at 428 K is given as:

$$E = 0.0368 * \ln\left(\frac{1}{a_{Ag}}\right) \quad (6.1)$$

where E is the emf of the cell in V,  $a_{Ag}$  is the activity of Ag which gives rise to emf. A decrease in the activity is envisaged during the presence of chlorine gas. This leads to the increase in the emf as seen as the sensor signal. Once the equilibrium has reached, the chlorine in the chamber is removed by passing dry air into the chamber.

## **6.4 FABRICATION AND ASSEMBLY OF SENSOR**

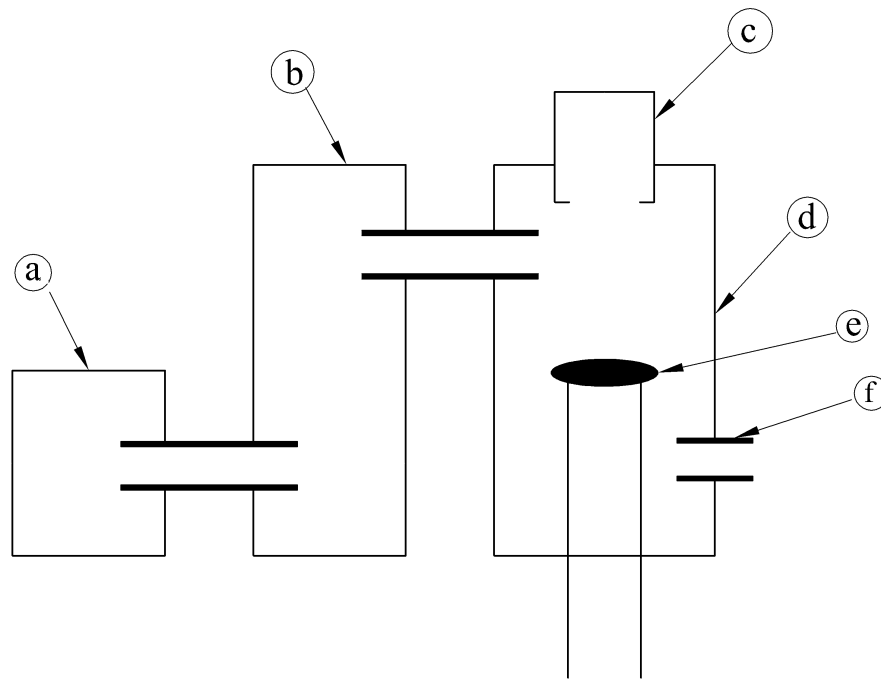
### **6.4.1 Materials for making of sensor**

The sensor parts were made by the following materials:

1. Electrolyte:  $AgI_{0.95}Cl_{0.05}$
2. Leads for connection: gold pads and gold wires, platinum foil and silver connectors
3. Heater material: platinum
4. Housing of sensor : glass
5. Sensor and heater leads: Teflon coated copper wire
6. Gas injection port: Teflon vecco with a silicone septum
7. Gas purifying unit: air passed through silica crystals, which acts as desiccant

### **6.4.2 Sketch of the sensor**

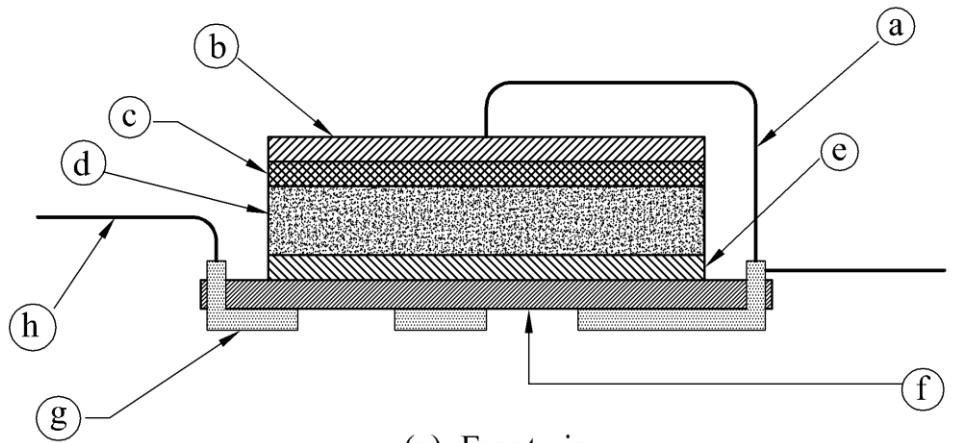
A schematic of the sensor housing and the purifier system is shown in Fig. 6.1. Once the sensor was exposed to chlorine gas of required concentration, after reaching the equilibrium, the purification system admits dry air into the chamber to remove the chlorine gas inside the glass chamber.



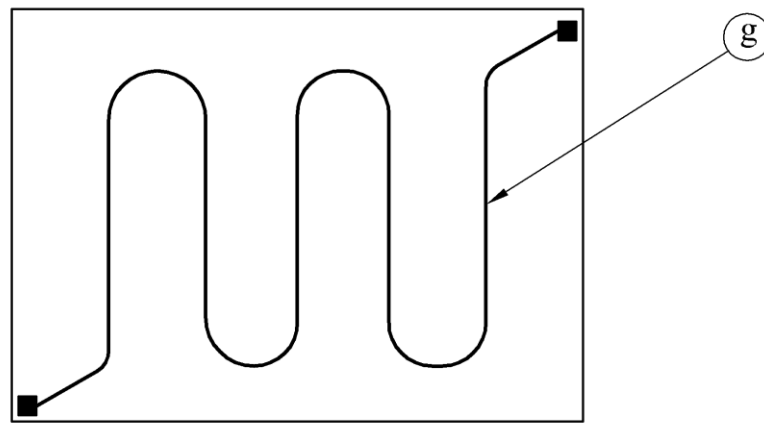
- |   |                          |
|---|--------------------------|
| (a) Air pump                            | (d) Sensor housing       |
| (b) Desiccant                           | (e) Electrochemical cell |
| (c) Veeco arrangement for injecting gas | (f) Port for gas outflow |

**Fig. 6.1 Layout of the sensor testing assembly**

The sensor configuration is shown in Fig. 6.2 (a) and (b). Fig. 6.2 (a) shows the configuration of the front part of the sensor where the solid electrolyte  $\text{AgI}_{0.95}\text{Cl}_{0.05}$  is sealed on one side with silver paste (reference electrode) and on the other side by platinum mesh which acts as the working electrode. The leads from the joints of the electrodes were taken using gold wires. To maintain the desired temperature, platinum heater coated on the other side of the substrate was used (Fig. 6.2).



(a) Front view



(b) Bottom view

- |   |  |
|---|--|
| (a) gold lead for working electrode                 | (e) silver thick film                  |
| (b) platinum foil                                   | (f) alumina substrate                  |
| (c) platinum mesh                                   | (g) platinum heater                    |
| (d) $\text{AgI}_{1-x}\text{Cl}_x$ solid electrolyte | (h) gold leads for reference electrode |

**Fig. 6.2 Sketch of sensor configuration of (a) cross sectional view showing the electrolyte and (b) bottom view showing platinum heater**

The photograph of the sensor showing the sensor chamber and the electrochemical cell is shown in Fig. 6.3 and 6.4. The platinum heater is a pre-calibrated screen printed heater, whose temperature is fixed by adjusting the resistance value of the platinum heater by fixing the potential and the current across the two terminals of the printed metal. For the calibration, the heater is placed inside the constant temperature zone of a furnace.

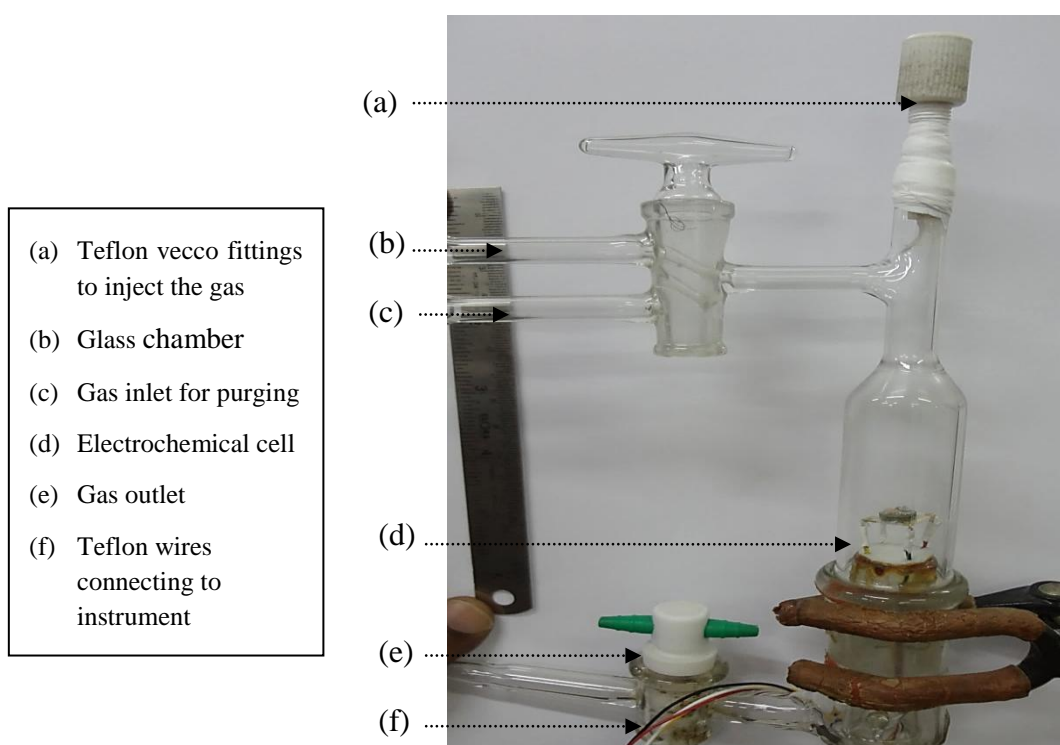
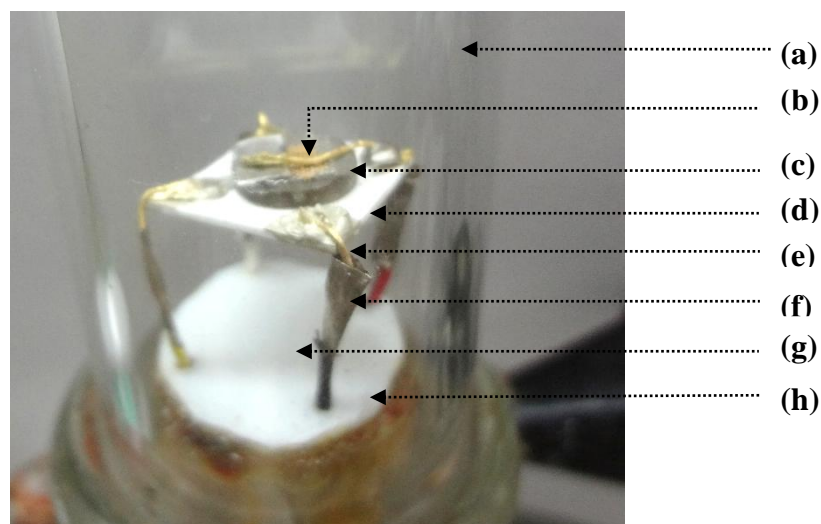


**Fig. 6.3** Photograph of the sensor assembly



- |                       |                                       |
|-----------------------|---------------------------------------|
| (a) Glass chamber     | (e) Gold leads                        |
| (b) Working electrode | (f) Silver tubes                      |
| (c) Solid electrolyte | (g) Leads for reference electrode     |
| (d) Alumina substrate | (h) Teflon based sealed with araldite |

**Fig. 6.4 Photograph of the electrochemical cell which was configured as sensor**

Once the thermal equilibrium is achieved, corresponding resistance of the platinum heater at the respective temperature of measurement with a heating rate of 5 K/ min is measured using Agilent data logger. After measuring the range of resistance in the temperatures of our interest, the calibration plot is made by plotting the resistance to the centreline temperature of the furnace. The calibrated plot of platinum heater is shown in Fig. 6.5. The intermediate resistance corresponding to temperature of measurement is calculated by fitting the calibration plot to a straight line. From the slope and the y-intercept of the straight line, the resistance for the given temperature of interest is calculated. For the plot given below, the fitting parameter is given as:

$$y = A + Bx \quad (6.2)$$

where  $A = 28.68 \pm 0.57$  and  $B = 0.06 \pm 0.01$

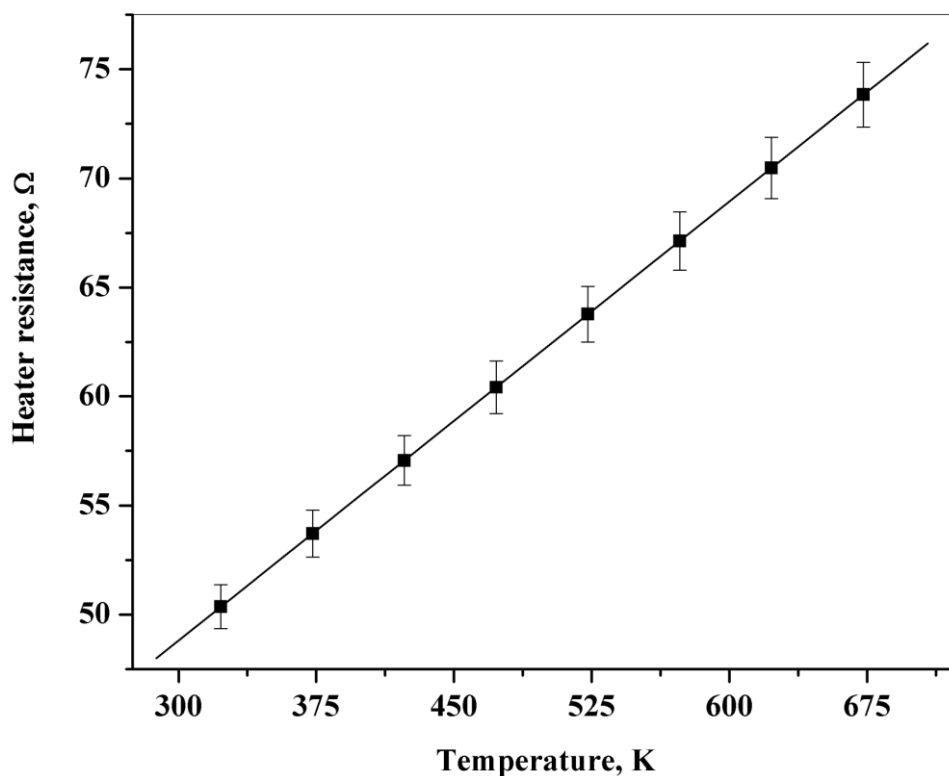


Fig. 6.5 Calibration plot for the screen printed platinum heater [1]

After the calibration, the respective temperature is fixed on the other side of the alumina substrate, by giving the necessary voltage and current for the desired temperature using a power supply module.

### 6.5 SENSING CHARACTERISTICS OF THE MINIATURISED SENSOR

The sensor was housed in a glass chamber and the temperature was maintained at 428 K across the pellet using the screen printed platinum heater and the baseline stability was logged for long hours with intermittent injection of chlorine gas to test its retrace. It was observed that the baseline was stable at ~200 mV. The measured emf was observed to reduce by half in the case of miniaturised sensor set up, where it was made sure that the electrodes were tightly packed. But, even then the theoretical value was not attained, the reasons for which are not clear.

Typical baseline of the sensor is shown in Fig. 6.6. Typical response of the sensor towards 17 vppb of chlorine gas is shown in Fig. 6.7. An injection of ~17 vppb of chlorine gas shows around 9 mV change in the emf of the cell. Typical response time for

the concentration was around 7 s and the 90 % baseline has retraced back in ~30 s. The repeatability for 17 vppb chlorine gas is shown in Fig. 6.8. It was found that the sensor exhibited consistently the similar response towards same concentration of the gas injected.

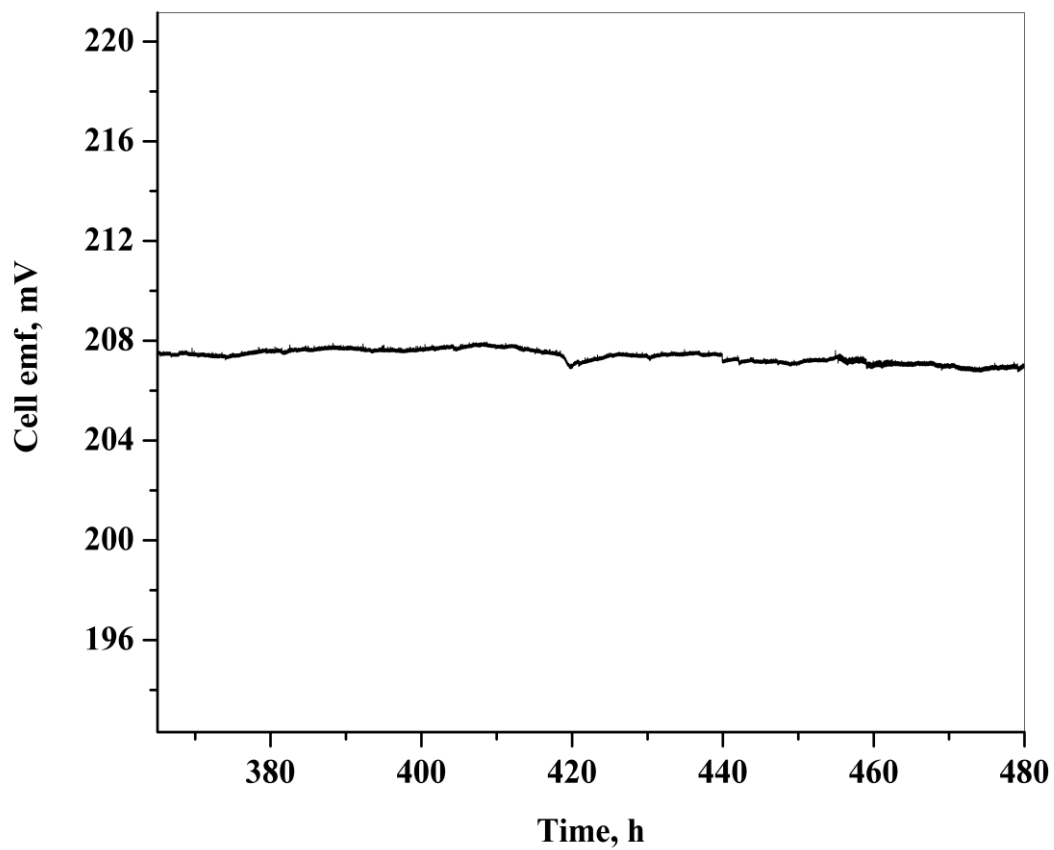


Fig. 6.6 Baseline of the electrochemical cell containing  $\text{AgI}_{0.95}\text{Cl}_{0.05}$  at 428 K

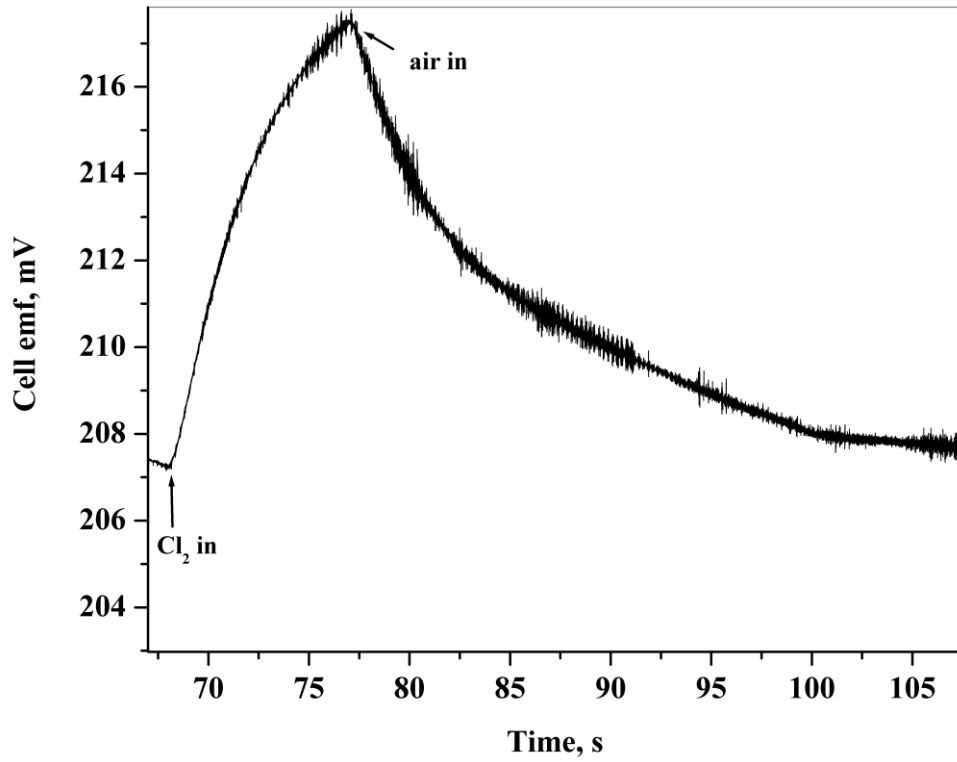


Fig. 6.7 Typical transient for 17 vppb of chlorine gas

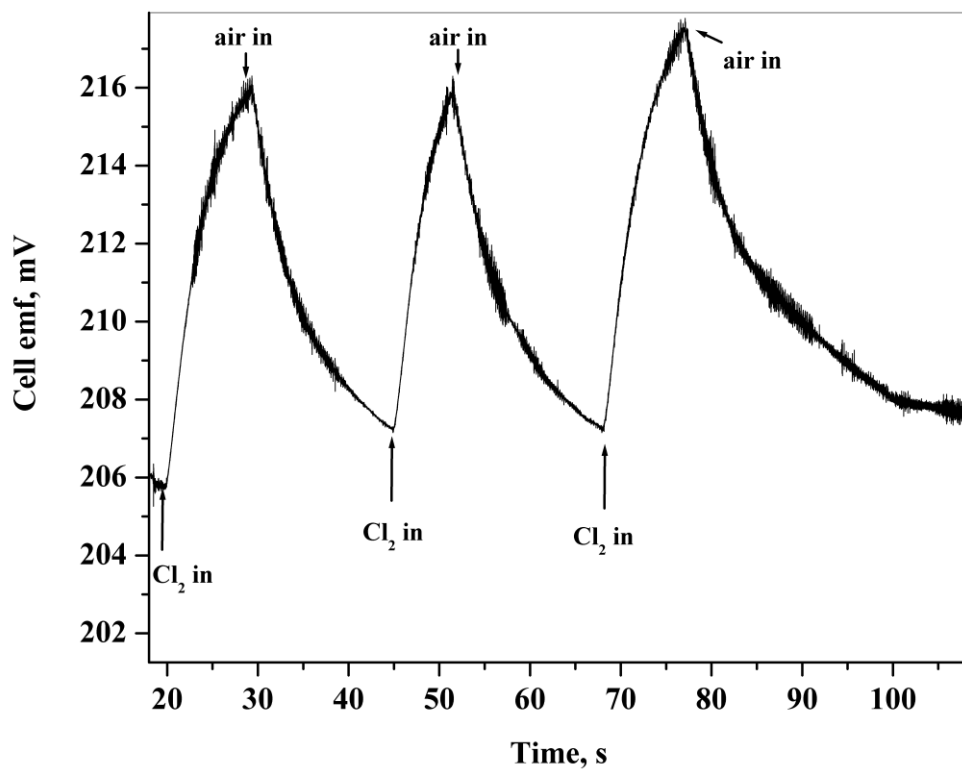


Fig. 6.8 Repeatability of sensor ( $\text{AgI}_{0.95}\text{Cl}_{0.05}$ ) towards 17 vppb of chlorine gas

The miniaturised glass chamber was around 60 ml only whereas in the bulk studies using 1 L sensor chamber was used. Therefore, the time for equilibration of the injected gas the electrode|electrolyte will be more in the case of chamber with larger dead volume. This will reflect in the response and the 90 % retrace time of the electrochemical cell. As the reduction in the dead volume is achieved in the miniaturised cell, reduction in the response and retrace time was observed. The chlorine gas injected was equilibrated in a small dead volume than in a larger one.

This configuration was tested for wide dynamic range sensing of chlorine from vppb to vppm levels of sensing. The calibration of  $\text{AgI}_{0.95}\text{Cl}_{0.05}$  is shown in Fig. 6.9. The values of the miniaturised sensor tested were around ~9 to 410 mV response towards ~17 to 15000 vppb of chlorine gas in static mode of injection. The response compared to the bulk in the range of 20-100 vppb of chlorine gas was similar. Advantage in miniaturising the sensor was found to be in the speed of sensing, as the response and the retrace times were found to reduce with decrease in the chamber volume.

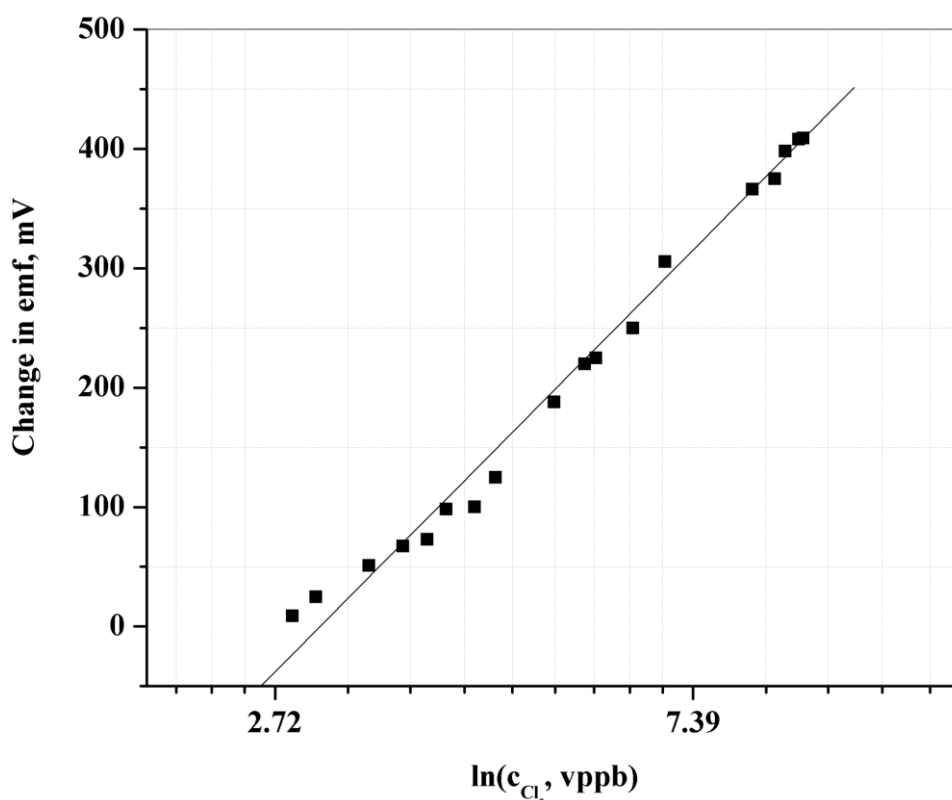


Fig. 6.9 Calibration plot of  $\text{AgI}_{0.95}\text{Cl}_{0.05}$  towards ~17 to 15000 vppb chlorine at 428 K in air

Typical response and 90 % retrace time were around 7 and 30s for all the concentrations of chlorine injected. In the concentration range a linear increase in emf output was observed as a function of chlorine ( $\ln c_{\text{Cl}_2}$ ) injected. Typically for 10 vppm, the change in emf output was ~398 mV and for 15 vppm the change was ~409 mV. As discussed in chapter 5.1, thermodynamically AgCl is more stable than AgI. Also, the phase diagram and physicochemical characterisation of AgCl and AgI discussed in chapter 3, was found to be around 0.05 mol%. The continuous reaction of chlorine with  $\text{AgI}_{1-x}\text{Cl}_x$  will lead to the formation of AgCl. Thus, theoretically the sample under study,  $\text{AgI}_{1-x}\text{Cl}_x$ , will eventually form AgCl reducing the speed of the redox reaction at the working electrode. But, it was observed that the cell was functioning in the span of few months even when repeated injections of trace levels of chlorine was made. This shows that even though the electrochemical cell is potentiometric type, the sensor behaviour is empirical towards chlorine sensing.

## 6.6 CONCLUSION

$\text{AgI}_{0.95}\text{Cl}_{0.05}$  composition was tested for the sensing properties in a miniaturised sensor assembly whose chamber volume was around 60 ml. The fabricated miniaturised sensor set-up was able to reduce the response and 90 % retrace times for sensing. The material was tested from ~17 to 15000 vppb of chlorine gas and was found to give nearly linear response until 15000 vppb of the gas. Thus,  $\text{AgI}_{0.95}\text{Cl}_{0.05}$  and the miniaturised cell configuration show promise to deploy them for field testing.

## 6.7 REFERENCES

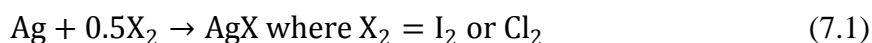
1. E. Prabhu, V. Jayaraman, K.I. Gnanasekar, T. Gnanasekaran and G. Periaswami, 2005, Pulsed laser deposition made thin film sensor for monitoring hydrogen in gas streams, Asian Journal of Physics, 14, No. 1&2, 33-40.

*This page is intentionally left blank.*

## CHAPTER 7

### SUMMARY AND CONCLUSIONS

Potentiometric sensors find important use in industry due to its wide dynamic range and high selectivity. Potentiometric sensors require materials with ions as predominant conducting species. AgI based materials have proved to exhibit good ionic conductivity for  $\text{Ag}^+$  ions above 420 K. Hence, materials with AgI as matrix are suitable to be used as solid electrolyte in potentiometric sensors. The compound formation equilibrium, viz. AgI and AgCl, in the presence of  $\text{I}_2$  and  $\text{Cl}_2$  respectively is represented by the equation:



The substitution of  $\text{Cl}^-$  was carried out to reduce the  $\beta$  to  $\alpha$  transition temperature of AgI, in order to bring down the temperature of the sensor by appropriately adding AgCl. Physicochemical characterisation using AAS and XPS established the solubility of AgCl in AgI to be  $< 5$  mol %. A methodology was evolved for analysing the precipitated AgCl in AgI beyond the solubility limit of AgCl in  $\text{AgI}_{1-x}\text{Cl}_x$ . Thus, from different physicochemical studies (XRD, AAS and XPS) the solubility limit of AgCl in AgI was established as  $< 5$  mol %. The onset of  $\beta$  to  $\alpha$  transition temperature and melting of AgI, measured using DSC facility, decreased with the addition of AgCl. All these basic studies have given significant support for corroborating the results from ionic transport measurements, which show the decrease in the ionic transference number beyond the solubility limit of AgCl in AgI. This in turn helped in finalising the sensor characterisation temperature and the composition suitable for testing. Results from bulk conductivity measurements were also in agreement with the thermal analysis wherein the  $\beta$  to  $\alpha$  transition temperature was found to first decrease and remains constant after the solubility limit of AgCl in AgI, in the conductivity measurement.

The sensing characteristics of  $\text{AgI}_{1-x}\text{Cl}_x$  ( $x = 0-0.05$ ) towards iodine and chlorine showed

a better performance of AgI towards iodine and  $\text{AgI}_{0.95}\text{Cl}_{0.05}$  towards chlorine in trace levels. Fairly good agreement between the experimental values and theoretical predicts was observed for  $\text{AgI}_{1-x}\text{Cl}_x$  ( $x=0, 0.025$  and  $0.05$ ) at 428 K in air towards 6-60 vppm of iodine.

The usefulness of the three electrode configuration for understanding the methodology for trace levels of adsorption of chlorine on AgI. The patterns from XPS proved to be a better support for confirming the results of impedance measurements. All the investigations on chlorine sensing mechanism of AgI using dielectric spectroscopy and XPS for the poor retrace behaviour confirms the formation of AgCl on the surface of AgI.

The testing of the miniaturised chlorine sensor fabricated in-house demonstrated the usefulness of  $\text{AgI}_{0.95}\text{Cl}_{0.05}$  to sense 17-15000 vppb of chlorine at 428 K. Advantage in miniaturisation of the sensor was in the response and retrace times, which were found to reduce with decrease in the volume of sensor housing.

## CHAPTER 8

### FUTURE PLAN

From the investigations carried out on  $\text{AgI}_{1-x}\text{Cl}_x$ , the following studies will be useful in widening the scope of understanding and investigating new materials and methodologies in the area of halogen sensing:

1. Understanding three electrode set-up for sensing application: Three electrode configuration was found to be useful in understanding the mechanism of sensing of AgI in the presence of chlorine gas. Extending the three electrode configuration to sensing studies for various gases to observe whether there is a change in the response of the sensor or improvement in the sensitivity based on the measurements can be made. Detailed investigations using the method to elucidate the reasons for the better response of  $\text{AgI}_{0.95}\text{Cl}_{0.05}$  towards iodine and chlorine.
2. Utilisation of the miniaturised set up: PVC industries use percentage levels of chlorine in their manufacturing processes. Materials doped with low chlorine content in AgI ( $\text{AgI}_{0.975}\text{Cl}_{0.025}$  and  $\text{AgI}_{0.95}\text{Cl}_{0.05}$ ) can be explored using the miniaturised set up to widen the dynamic range for chlorine sensing.
3. Unravelling new materials for halogen sensing: identification of alternate materials, which can be used at room temperature to sense iodine and chlorine, their characterisation and sensing studies.